

# VAN DER WAALS STACKING OF TWO-DIMENSIONAL MATERIALS

A Dissertation

Presented to the Faculty of the Graduate School

of Cornell University

in Partial Fulfillment of the Requirements for the Degree of

Doctor of Philosophy

by

Lujie Huang

December 2017

© 2017 Lujie Huang  
ALL RIGHTS RESERVED

# VAN DER WAALS STACKING OF TWO-DIMENSIONAL MATERIALS

Lujie Huang, Ph.D.

Cornell University 2017

Two-dimensional (2D) materials, which show a wide range of electrical and optical properties, can serve as building blocks to form stacked 2D systems that are connected by interlayer van der Waals interactions. Any 2D materials can be stacked together, regardless of their crystal structures: this versatility offers an opportunity to realize “materials by design”, where, through stacking, film properties can be directly manipulated and film thicknesses can be precisely controlled. In this dissertation, we focus on studying the fabrication, characterization, and application of the stacked 2D systems on a technologically relevant large scale.

We first introduce the growth of wafer-scale homogeneous monolayer transition metal dichalcogenides (TMD) films using metal-organic chemical vapor deposition (MOCVD), a growth technique that enables the fine tuning of precursor kinetics by using gas-phase precursors. After introducing our work on 2D material growth, we switch to 2D stacking and talk about a model 2D stacking system — twisted bilayer graphene (tBLG), where twist angle ( $\theta$ ) serves as a key parameter for manipulating the physical properties. We first discuss the  $\theta$ -dependent properties in tBLG and introduce a vacuum-assisted direct stacking technique that is able to generate high-quality,  $\theta$ -controllable tBLG using CVD sample sources. We then focus on small- $\theta$  tBLG, where, after presenting a quantitative study of the  $\theta$  dependence in its Raman  $R'$  process, we introduce a  $\theta$  measurement method that is developed based on these quantitative results.

Finally, we utilize this angle detection method to study the  $\theta$ -dependent electrical properties in small- $\theta$  tBLG. After discussing the 2D stacking model system tBLG, we switch to stacked 2D systems where no apparent changes in properties are introduced by stacking. This kind of stacked system can also have wide applications due to the atomically precise thickness control and well-defined surfaces. As a demonstration, we introduce our preliminary research that builds functional dielectric films from stacked multilayer WS<sub>2</sub>.

## **BIOGRAPHICAL SKETCH**

Lujie Huang was born and raised in a small town in Hubei, China. In 2007, she entered Chemistry department of Tsinghua University as an undergraduate student. In 2011, she graduated from Tsinghua University and arrived in Ithaca, New York to pursue a Ph.D in Physical chemistry. She completed her Ph.D. research under the supervision of Prof. Jiwoong Park.

To my parents

## ACKNOWLEDGEMENTS

Looking back at my experience in graduate school, I feel incredibly lucky to have been accompanied by so many wonderful people. I would first like to thank my dissertation advisor, Jiwoong Park. Joining the Park group is one of the best decisions I have ever made. Jiwoong is a great mentor. He has encouraged me to learn many things, not only because my projects require them, but also because they are a part of the knowledge set that he hoped I would gain. Jiwoong is an incredibly brilliant scientist. It is truly engaging to discuss scientific topics with him. He is also an excellent team leader. He manages to build a supportive group atmosphere, from which I have benefited a lot. I have learned many things from Jiwoong: how to do research, communicate scientifically, and also how to be an effective leader. I thank Jiwoong for having me in his group, for educating me, and for being supportive throughout my Ph.D.

Next, I would like to thank my colleagues in the Park group. You guys are amazing coworkers, collaborators, and friends to me. Wei, thank you for training me to do device fabrication, showing me how research is done, and guiding me throughout my first research project. I am sincerely grateful for the time and effort you spent mentoring me. All of my seniors, Robin, Mark, Lola, Carlos, and LiHong, thank you for your help and your suggestions. You guys made me feel welcomed and supported in this group. Also, I would like to thank the amazing postdocs in the Park group, Cheol-Joo, Fai, Kibum, Marcos, Matt, Yui, Joonki, Chibeom, Long, Lei, and Yu. You guys were the encyclopedias to which I could turn. Joonki, especially, thank you for making my post-graduation transition so smooth. I would also like to thank Joel, Saien, Kanheng, Yimo, Hui, Preeti, Kim, Fauzia, and Josh for being amazing lab mates and friends. And of course, my brilliant collaborators, Wei, Lola, Cheol-Joo, Marcos, Kibum, Saien,

Hui and Kanheng, thank you for the amazing work. Park group, I have truly enjoyed your company.

In Cornell, I have met many amazing people. I have learned a lot from the courses taught by Prof. Greg Ezra, Prof. Roger Loring, Prof. Craig Fennie and all my other professors. My graduate school experience would not have been so pleasant without the help of Pat Hine, the CNF staff members, and the CCMR staff members. And of course, I thank my special committee: Greg Ezra and Dan Ralph, who were always there when I needed suggestions.

My final thanks go to my friends and family. To my mom and dad, thank you for raising me, for encouraging your little girl to go study abroad, for having faith in me, and for being supportive. I would never be able to accomplish this without you. My dearest friends, thank you for creating so many great memories with me in Maplewood, Westview, Hasbrouck, Baker, PSB, in the state parks, New York City, Orlando, and Chicago. You guys are the best. I am incredibly lucky to have met you all.

## TABLE OF CONTENTS

Biographical Sketch . . . . .	iii
Dedication . . . . .	iv
Acknowledgements . . . . .	v
Table of Contents . . . . .	vii
List of Figures . . . . .	ix
<b>1 Introduction</b>	<b>1</b>
1.1 Overview . . . . .	1
1.2 2D materials family . . . . .	3
1.3 2D materials exfoliation and synthesis . . . . .	7
1.3.1 Exfoliation . . . . .	7
1.3.2 Synthesis . . . . .	9
1.4 2D Van der Waals stacking . . . . .	11
1.4.1 General features . . . . .	11
1.4.2 History . . . . .	12
1.4.3 Stacking techniques . . . . .	13
1.5 Dissertation outline . . . . .	16
<b>2 MOCVD synthesis of TMD</b>	<b>18</b>
2.1 Introduction . . . . .	18
2.2 Growth method and optimization . . . . .	20
2.3 Optical and structural characterization of TMD . . . . .	25
2.4 Electrical characterization of TMD . . . . .	28
2.5 Summary . . . . .	32
<b>3 Model Stacking System: Twisted bilayer graphene</b>	<b>34</b>
3.1 Introduction . . . . .	34
3.2 Electronic band structure . . . . .	35
3.3 Angle-dependent properties of tBLG . . . . .	42
3.4 Assembly of tBLG by vacuum-assisted direct stacking . . . . .	48
3.4.1 Introduction . . . . .	48
3.4.2 Graphene CVD growth and transfer . . . . .	49
3.4.3 Vacuum-assisted direct stacking . . . . .	53
3.5 Summary . . . . .	55
<b>4 Small-<math>\theta</math> tBLG angle detection by Raman R' process</b>	<b>56</b>
4.1 Introduction . . . . .	56
4.2 $\theta$ dependence of Raman R' process . . . . .	58
4.3 R' process polarization property . . . . .	62
4.4 $\theta$ mapping through R' process . . . . .	66
4.5 $\theta$ -dependent electronic features in small- $\theta$ tBLG . . . . .	70
4.6 Other electronic features in small- $\theta$ tBLG . . . . .	72

4.7	Large- $\theta$ tBLG and Bernal BLG electronic features . . . . .	76
4.8	Summary . . . . .	77
<b>5</b>	<b>Stacked TMD as functional dielectric layer</b>	<b>79</b>
5.1	Introduction . . . . .	79
5.2	Stacking and device fabrication . . . . .	80
5.3	Dielectric properties of the stacked TMD film . . . . .	83
5.4	Summary . . . . .	86
<b>6</b>	<b>Future directions</b>	<b>87</b>
6.1	TMD growth on patterned substrate . . . . .	87
6.2	Explore angle generated features in small- $\theta$ tBLG . . . . .	89
6.3	Free-standing stacked 2D material circuitry . . . . .	90
	<b>Bibliography</b>	<b>92</b>

## LIST OF FIGURES

1.1	Graphene crystal and electronic structure . . . . .	3
1.2	hBN crystal and electronic structure . . . . .	4
1.3	MoS <sub>2</sub> crystal and electronic structure . . . . .	5
1.4	2D materials family . . . . .	6
1.5	Polymer-free assembly of layered materials . . . . .	14
2.1	MOCVD growth setup . . . . .	20
2.2	MOCVD layer-by-layer growth . . . . .	21
2.3	MoS <sub>2</sub> grain structure optimization . . . . .	23
2.4	Wafer-scale homogeneous monolayer TMD films . . . . .	26
2.5	Continuity of monolayer MoS <sub>2</sub> . . . . .	27
2.6	Electrical characterization of MoS <sub>2</sub> FETs . . . . .	29
2.7	MoS <sub>2</sub> wafer-scale FETs . . . . .	31
3.1	Crystal and electronic structures of SLG and Bernal BLG . . . . .	35
3.2	tBLG unit cell size vs. $\theta$ . . . . .	37
3.3	Crystal and electronic structure of tBLG . . . . .	39
3.4	ARPES data from tBLG . . . . .	40
3.5	tBLG Raman G peak angle dependence . . . . .	42
3.6	tBLG optical absorption angle dependence . . . . .	43
3.7	Quantitative analysis of tBLG $\theta$ dependence . . . . .	44
3.8	tBLG CD spectra $\theta$ dependence . . . . .	46
3.9	tBLG vHS direct mapping with STS . . . . .	47
3.10	Statistical analysis of twist angle distribution in BLG . . . . .	49
3.11	Schematics of vacuum-assisted direct stacking . . . . .	54
4.1	Schematics and representative spectrum of Raman R' process . . . . .	59
4.2	Quantitative study of the Raman spectroscopy of small- $\theta$ tBLG . . . . .	61
4.3	On resonance R' peak polarization dependence . . . . .	63
4.4	Off resonance R' peak polarization dependence . . . . .	64
4.5	Derivation of the polarization dependence . . . . .	65
4.6	Polarization correction of R' peak intensity . . . . .	67
4.7	Angle mapping with Raman R' peak . . . . .	68
4.8	Effects of heating on Raman G peak . . . . .	69
4.9	Electrical conductivity study of dual gate small- $\theta$ tBLG device . . . . .	71
4.10	Density of states of tBLG based on tight binding calculation . . . . .	72
4.11	Effects of doping and vertical field on small- $\theta$ tBLG . . . . .	74
4.12	Effects of doping and vertical electrical on large- $\theta$ tBLG and Bernal tBLG . . . . .	77
5.1	Graphene transistor with stacked WS <sub>2</sub> as dielectric layer . . . . .	83
5.2	Graphene transistor gate leakage . . . . .	84
5.3	Graphene transistor channel performance . . . . .	85

5.4	Extracting dielectric constant of stacked WS <sub>2</sub> . . . . .	86
6.1	Patterned MoS <sub>2</sub> growth . . . . .	88
6.2	Fabrication of free-standing stacked 2D material circuitry . . . .	90

# CHAPTER 1

## INTRODUCTION

### 1.1 Overview

Two-dimensional (2D) materials are a group of materials that are one to a few atoms thick. After almost two decades of intense study, a plethora of 2D materials are now available, which cover a wide range of electrical and optical properties [1]. These 2D material layers can serve as building blocks to form stacked 2D systems that are connected by van der Waals interlayer interactions. In stacked 2D systems, due to the unique nature of van der Waals forces, all kinds of 2D materials can be stacked together, regardless of their lattice constants. This versatility is quite appealing, since tremendous possibilities in stacked 2D systems are expected through the permutation and combination of the large collection of 2D building blocks, offering an opportunity to realize “materials by design” [2].

There are two main approaches to utilizing 2D stacking for various applications. First, we can use interlayer interactions to manipulate the properties of the building blocks in a stacked 2D system. Among the property-manipulation mechanisms, there are the formation of a static potential in the form of a moiré pattern, the formation of strain solitons by surface reconstruction, the charge transfer effect, and the proximity effect. Examples include the interlayer optical properties in twisted bilayer graphene (tBLG) [3–7], the band gap opening in a graphene/hexagonal boron nitride (hBN) stack [8], the valley hall boundary states formation in small angle tBLG [9–11], and the spin-orbit interaction enhancement in a graphene/transition metal dichalcogenide (TMD) stack [12, 13]. The reason for these changes in properties being so significant is that, unlike

bulk materials where the effects of the environment are screened by the surface, 2D material itself is the surface and can be strongly altered by the environment. Moreover, in stacked 2D systems, the environmental perturbation is also provided by 2D materials, which have well-defined surfaces that are free from dangling bonds. This ensures the property manipulation in stacked 2D systems to be highly controllable.

In the second approach, 2D stacking can be used to build thin films with precise thickness and well-defined surfaces. These thin films can be assembled with 2D materials or other materials to generate devices with better electronic/optoelectronic performance, novel heterostructure devices, and atomically thin circuitry. Examples are the demonstration of high mobility graphene transistors in graphene/hBN [14] and hBN/graphene/hBN stacks [15], as well as the building of tunneling devices in graphene/hBN/graphene stacks [16,17]. This approach takes advantage of the precise thicknesses as well as the chemically well-defined surfaces of 2D materials.

In this chapter, we will provide the background review for 2D stacking. First, we will introduce the stacking building blocks by listing the structures and properties of various 2D materials and discussing their exfoliation and synthesis. After that, we will talk about 2D stacking itself, reviewing the research status of 2D stacking and discussing the stacking techniques. At the end, we will provide an outline for the entire dissertation.

## 1.2 2D materials family

2D material is one layer out of layered material. It can be isolated because layered material has weaker bonding in the vertical direction. The concept “2D” comes from the crystal structure confinement. Within the 2D plane, atoms connect to each other through covalent bonds. At the edge of this 2D film, there are unsaturated bonding sites — the dangling bonds — from which crystal growth is allowed, while orthogonal to the plane, on the film surface, all of the bonding sites are saturated. The crystal therefore generally does not expand along the third dimension and is two-dimensionally confined.

In the 2D materials family, graphene, hBN, and molybdenum disulfide ( $\text{MoS}_2$ ) have been studied most extensively. In Figure 1.1, 1.2, and 1.3, the crystal and electronic structures of these materials are provided.

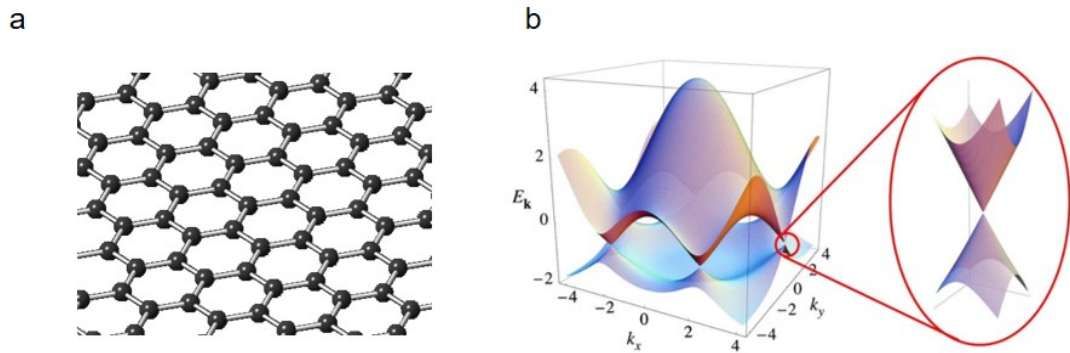


Figure 1.1: Graphene crystal and electronic structure  
(a) Graphene crystal structure. (b) Graphene band structure calculated from tight-binding model. Left: energy spectrum (in units of  $t$ ) for finite values of  $t$  and  $t'$ , with  $t = 2.7$  eV and  $t' = 0.2 t$ . Here  $t$  is the nearest-neighbor hopping energy and  $t'$  is the next nearest-neighbor hopping energy. Right: zoom-in of the energy bands close to one of the Dirac points. b is adapted from Reference [18].

Graphene is made up of one layer of carbon atoms in a honeycomb lattice. Near charge neutrality, the electronic band structure of graphene reveals a linear

dispersion, known as the Dirac cone. Graphene is the first reported 2D material [19]. It is semi-metallic and has incredibly high carrier mobility due to its unique band structure ( $10,000 \text{ cm}^2 \cdot \text{V}^{-1} \cdot \text{s}^{-1}$  in the initial report [19] and over 1 million  $\text{cm}^2 \cdot \text{V}^{-1} \cdot \text{s}^{-1}$  reported later in suspended devices [20,21] and hBN-stacked devices [14,15]). Since mobility is one of the most important properties of electronic materials, graphene inspired an outburst of research. Later, with the observation of properties such as the fractional quantum hall effect [22,23] and high mechanical strength [24], more attention was drawn to graphene, which then ignited the 2D material research field.

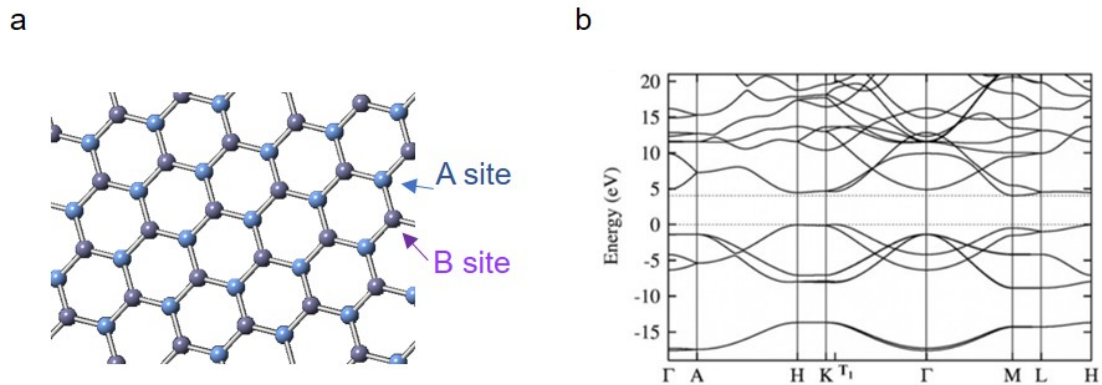


Figure 1.2: hBN crystal and electronic structure  
 (a) hBN crystal structure. (b) hBN band structure from DFT-LDA calculations. b is adapted from Reference [25].

hBN is an analogue to graphene. It is a one-atom-thick honeycomb lattice formed by alternating boron and nitrogen atoms. Because the A and B sites of the hBN lattice are occupied by different atoms, a bandgap is opened in hBN. The size of the hBN bandgap is around 6 eV [26], making hBN an insulator. As an insulating material with a surface free of dangling bonds, hBN can be an ideal dielectric layer for channel materials (such as graphene) that are sensitive to charged impurities and surface roughness.

MoS<sub>2</sub> is made up of one layer of molybdenum atoms sandwiched between

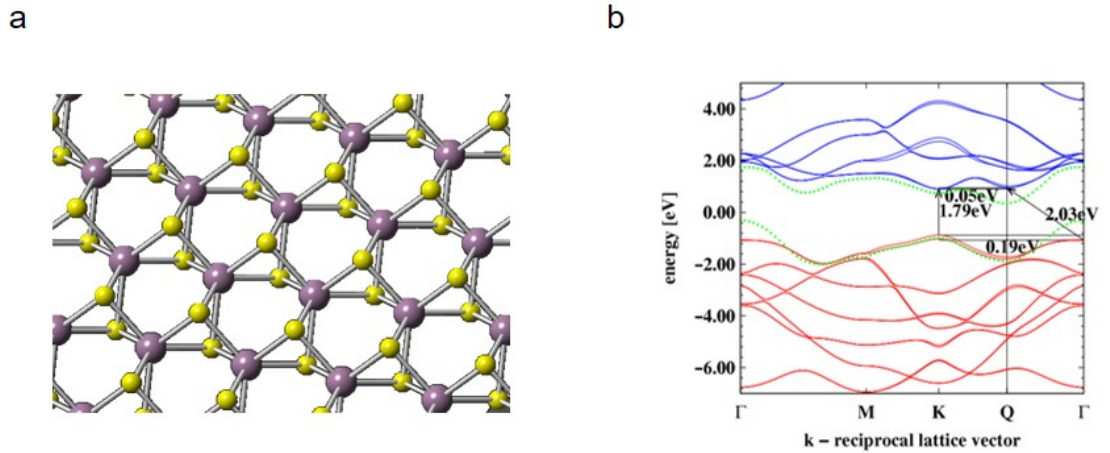


Figure 1.3: MoS<sub>2</sub> crystal and electronic structure  
 (a) MoS<sub>2</sub> crystal structure. (b) MoS<sub>2</sub> band structure. The green lines show the top (bottom) valence (conduction) bands in bulk MoS<sub>2</sub>. The blue and red lines are the conduction and valence bands of MoS<sub>2</sub>. b is adapted from Reference [27].

two layers of sulfur atoms. It is a semiconductor with a direct bandgap of 1.8 eV [28]. MoS<sub>2</sub> was reported to show a room temperature mobility of around 70 cm<sup>2</sup>·V<sup>-1</sup>·s<sup>-1</sup> and a high on-off ratio of 10<sup>8</sup> [29]. Although being much lower than graphene, this mobility is comparable to polycrystalline silicon (typically around 100 cm<sup>2</sup>·V<sup>-1</sup>·s<sup>-1</sup> [30]), and higher than other thin film semiconductors such as amorphous silicon (typically lower than 1 cm<sup>2</sup>·V<sup>-1</sup>·s<sup>-1</sup>) and organic semiconductors (typically lower than 1 cm<sup>2</sup>·V<sup>-1</sup>·s<sup>-1</sup> [31], and reaches 20 to 40 cm<sup>2</sup>·V<sup>-1</sup>·s<sup>-1</sup> in single crystalline organic semiconductors such as rubrene [32]), which has inspired interest for MoS<sub>2</sub> electronic applications. Moreover, the existence of a direct bandgap, as well as the valley polarization introduced by the broken inversion symmetry [33,34], make MoS<sub>2</sub> an interesting subject for optical and electro-optical studies.

In Figure 1.4, we provide a summary of the 2D materials family [1]. Among them, a big subgroup is TMD material. TMDs are three atoms thick and have the chemical composition MX<sub>2</sub> (M: transition metal, X: group 16 elements). MoS<sub>2</sub>

Graphene family	Graphene	hBN 'white graphene'	BCN	Fluorographene	Graphene oxide
2D chalcogenides	MoS <sub>2</sub> , WS <sub>2</sub> , MoSe <sub>2</sub> , WSe <sub>2</sub>		Semiconducting dichalcogenides: MoTe <sub>2</sub> , WTe <sub>2</sub> , ZrS <sub>2</sub> , ZrSe <sub>2</sub> and so on	Metallic dichalcogenides: NbSe <sub>2</sub> , NbS <sub>2</sub> , TaS <sub>2</sub> , TiS <sub>2</sub> , NiSe <sub>2</sub> and so on	
				Layered semiconductors: GaSe, GaTe, InSe, Bi <sub>2</sub> Se <sub>3</sub> and so on	
2D oxides	Micas, BSCCO	MoO <sub>3</sub> , WO <sub>3</sub>	Perovskite-type: LaNb <sub>2</sub> O <sub>7</sub> , (Ca,Sr) <sub>2</sub> Nb <sub>3</sub> O <sub>10</sub> , Bi <sub>4</sub> Ti <sub>3</sub> O <sub>12</sub> , Ca <sub>2</sub> Ta <sub>2</sub> TiO <sub>10</sub> and so on	Hydroxides: Ni(OH) <sub>2</sub> , Eu(OH) <sub>2</sub> and so on	
	Layered Cu oxides	TiO <sub>2</sub> , MnO <sub>2</sub> , V <sub>2</sub> O <sub>5</sub> , TaO <sub>3</sub> , RuO <sub>2</sub> and so on		Others	

Figure 1.4: 2D materials family

Blue: monolayers proved to be stable under ambient conditions. Green: likely stable under ambient conditions. Pink: unstable in air but may be stable in inert atmosphere. Grey: 3D compounds that have been successfully exfoliated down to monolayers, as is clear from atomic force microscopy, for example, but for which there is little further information. Adapted from Reference [1].

discussed in the above paragraph is a representative TMD material. Regarding TMDs, there are several aspects worth noting. First, for TMDs with different chemical compositions, the properties can vary dramatically. For example, most TMDs are semiconductors, while group 5 transition metal TMDs are metals. Second, since the three-atom-thick structure allows the crystal structures to be varied in certain ways with low energy costs (for example 1T and 2H phases), there exist semi-stable phases in some TMDs [35, 36]. Finally, we should note that not all TMDs are stable under ambient conditions, for example niobium diselenide (NbSe<sub>2</sub>). To study unstable TMDs, sandwiching them with stable 2D materials such as hBN is the mainstream approach [37].

Beside what has been introduced in detail, other examples of 2D materials include graphene oxide, black phosphorus, 2D oxides, etc. In this dissertation, we mainly work with graphene and TMDs. The reasons are: first, as discussed in this section, these materials have outstanding electrical and optical proper-

ties; second, as shall be discussed in the coming section, high-quality large-scale syntheses of graphene and TMDs are available.

### **1.3 2D materials exfoliation and synthesis**

When evaluating the techniques for generating 2D materials, there are three key aspects: the quality, the homogeneity, and the scale. Quality refers to the idealness of the 2D crystal, i.e. having a low level of property-affecting defects. Homogeneity refers to the layer thickness. Normally we require a homogeneous single layer throughout the entire sample. However, ideally, techniques that can generate homogenous films with any assigned number of layers are preferred, which is much harder to achieve. Scale is straightforward: it refers to the sample size. So long as quality and homogeneity can be preserved, the larger the better. Normally, when the sample size is on the order of inches (wafer size), it can be called large scale.

There are two approaches to generate 2D materials: exfoliation and synthesis.

#### **1.3.1 Exfoliation**

Exfoliation is a top-down approach: start with the bulk layered crystals and peel single layers off of them. The bulk crystals can come from either a natural source or a synthetic source. It is easier to gain access to natural source crystals. Synthetic source crystals, provided that the synthesis process is well-developed, can be of higher quality (such as the low defect level hBN crystal produced by

K. Watanabe and T. Taniguchi) and allow for the availability of crystals that are rare or absent in nature (such as WSe<sub>2</sub> and Nb doped MoS<sub>2</sub> [38]).

Starting with bulk crystals, 2D films can be exfoliated using mechanical exfoliation, i.e. the Scotch tape method. Applying this method, the bulk crystal is first thinned down using the Scotch tape; then 2D layers are peeled off from the bulk crystal and transferred to the target substrate through the Van der Waals interaction between the 2D layers and the substrate. The biggest advantage of mechanical exfoliation is high film quality. The generated 2D layers come in contact with very little contaminants during the process; thus, the amount of scattering sites on the 2D layer is constrained to a low level. Mechanical exfoliation is the method used in the initial work involving 2D materials [19], and is still one of the mainstream methods today, especially in occasions when low scattering density and high mobility are desired. When evaluating the quality of 2D samples, a common practice is to compare them to exfoliated samples. However, mechanical exfoliation has a major downside. It performs quite poorly with respect to homogeneity and scale: the layers produced by this method have random thickness and are normally on the order of micrometers.

Besides mechanical exfoliation, 2D materials can also be exfoliated from bulk crystals using the batch chemical/mechanical treatment [39–42]. The idea is to first weaken the layer-layer interaction and increase the layer-solution interaction by chemical reaction and/or adding surfactants, and then separate the layers using ultrasonic treatment. This method is compatible with batch processing and is of low cost, but the 2D materials produced using this method have high level of defects. 2D materials generated by this method are normally used in more application-oriented processes such as 2D material batteries.

### 1.3.2 Synthesis

2D materials synthesis is a bottom-up approach. It aims at directly producing single layer films through growth. To achieve this goal, the key is to suppress the formation of multilayers.

The mainstream technique for 2D synthesis is chemical vapor deposition (CVD). Different 2D materials have different chemical natures, and their CVD growth mechanisms can be quite different. Roughly, the growth mechanisms can be divided into two categories: growth that involves specific precursor-substrate chemistry and growth that does not involve specific precursor-substrate chemistry.

For CVD growth that involves specific precursor-substrate chemistry, the substrate acts as a catalyst for the growth. After the formation of a fully-covered first layer, further growth is suppressed, since the precursors are no longer able to contact the catalytic substrate. For this kind of growth, choosing a proper substrate is critical. For example, graphene CVD growth has been demonstrated on metallic substrates such as Pt [43], Ru [44], Ir [45], Ni [46, 47], and Cu [48]. Among them, Cu has high catalyst efficiency and low carbon solubility. With Cu as the growth substrate, a fully covered single layer is formed in a short time, after which multilayer growth is terminated. In comparison, with Ni as the substrate, multilayers are formed from carbon precipitation due to high carbon solubility. With Pt, Ru or Ir as the growth substrate, only small nonuniform multilayer graphene islands are formed, since these metals are not good catalysts for graphene formation.

For CVD growth that does not involve specific precursor-substrate chem-

istry, the role of the growth substrate is mainly to provide an interface where precursors or decomposed precursors can rest, move around, and finally meet each other to form the 2D films. The substrate does not have strong catalytic effects and does not need to be of a specific kind. Unavoidably, this growth mechanism does not favor the suppression of multilayer growth. However, single layer growth is still possible. Due to the absence of dangling bonds on the surfaces of 2D materials, the free energy of precursors on 2D materials is higher than on the growth substrates, which favors the growth of fully covered first layer before the starting of the multilayer growth. However, because the difference in free energy is small, to get the thermodynamically favored result, it is critical to control the kinetics of the process and stop the growth at precise time. The CVD growth of TMDs on silicon oxide ( $\text{SiO}_2$ ) is a representative example for 2D material CVD growth that does not involve specific precursor-substrate chemistry. As shall be introduced in chapter 2, their monolayer growth has been achieved.

Compared with exfoliation, the biggest advantage of synthesis is that it can be scaled up. For applications that go beyond proof-of-concept demonstrations, synthesis is a better approach. However, the quality of synthetic 2D materials is, in most cases, inferior to exfoliated ones, and the film homogeneity depends on precise growth control. The ideal 2D synthesis technique should generate high-quality, homogenous, and large-scale samples.

For graphene, there is another synthetic method: the high temperature thermal decomposition of silicon carbide. Graphene produced by this method is mostly used in scanning tunneling microscope (STM) [49] and angle-resolved photoemission spectroscopy (ARPES) studies [50,51], because the sample sur-

face is clean and sits on top of a flat and semi-conducting substrate. The downside of this method is that the graphene films are not homogeneous and are difficult to isolate from the substrate.

## 1.4 2D Van der Waals stacking

### 1.4.1 General features

To better understand the characteristics of 2D stacking, we can compare it with another layer-by-layer building technique, molecular beam epitaxy (MBE). When using MBE to grow 3D heterostructures, we can control the layer thickness down to the atomic scale. However, the adjacent layers are connected by covalent bonds and need to have matching crystal structures. This requirement strongly limits the variety of the layer composition. Compared with MBE, 2D stacking does not require lattice match, yet still yields a control over layer thickness with atomic precision. This versatility of composition comes from the fact that 2D stacked layers are brought together by interlayer van der Waals force instead of covalent bonds.

Besides composition versatility, the interlayer van der Waals interaction also adds a new degree of freedom — the interlayer rotation angle ( $\theta$ ). In certain stacked 2D materials systems,  $\theta$  can be a key parameter for determining physical properties. (This  $\theta$  dependency in stacked 2D materials is one of the main topics for this dissertation, which will be discussed in chapter 3 and 4 using the model system twisted bilayer graphene.)

For 2D stacking, we also need to note that the stacking-induced property change of the building blocks can be much weaker than in systems like 3D heterostructures grown by MBE. The reasons for this are the degree of property change is decided by the strength of the interaction, and the van der Waals force, though strong enough to hold the layers together, is much weaker than covalent bonds. In many cases, stacked 2D films behave just as independent 2D materials adding together. This is not necessarily a disadvantage. These kinds of 2D stacked films are direct analogies to the layered functional films in electronic and optoelectronic devices. They can therefore serve the same purposes while also having atomically precise thickness control, and well-defined dangling-bond-free interfaces.

### **1.4.2 History**

Not surprisingly, the early trials of 2D stacking were done with hBN. These pioneering works were motivated by the need for a better substrate than SiO<sub>2</sub> for graphene electronic devices. Back in 2008, through the demonstration of high-mobility transistors with suspended graphene [20, 21], it was confirmed that charge impurity sites in SiO<sub>2</sub> was causing substantial performance degradation in graphene. Because of this, researchers start to search for substrates that are free of surface charge impurities. In 2010, the Columbia group reported that hBN can serve as a high-quality substrate for graphene devices. [14] Following this work, encapsulation of graphene by hBN was demonstrated. In 2013, a stacking technique involving multiple pick-ups was developed and contamination-free hBN encapsulation of graphene was realized. [15] After that, this technique was proven to work on other 2D materials such as TMDs [52] as

well as 2D materials that are unstable under ambient conditions [37]. It became the mainstream stacking technique widely used in the 2D research field.

Along with the efforts to improve device performance by stacking, several other research directions were explored at the same time. One direction is to study effects introduced by the layer-layer interactions in stacked 2D films. A signature work in this direction is the observation of Hofstadter's butterfly [8, 53] in the moiré pattern created by graphene-hBN interaction. Another direction is to develop new kinds of electronic devices which are impossible to generate using traditional materials. The representative work is the building of field-effect tunneling transistors [16, 17]. Besides these two works, with 2D stacking, a strong Coulomb drag was observed between electrons from two parallel graphene layers separated by few layers of hBN [54].  $\theta$ -dependent optical properties [3–7], as well as  $\theta$ -dependent cross-layer electrical conductance [55], were also observed.

### 1.4.3 Stacking techniques

A good 2D-stacking technique needs to satisfy two requirements. First, the technique should ensure contamination-free interface. If contaminants exist between the layers, all important features of the 2D stacking (e.g. well-defined thickness, chemically well-defined interfaces, and well-controllable interlayer interactions) would be lost. To achieve such a goal, the key is to design a process which ensures that the film surface contacts nothing but the surfaces of other 2D materials or well-cleaned substrate surfaces during the stacking. Second, the stacking technique should have high yield. To ensure high yield, the

keys are to bring two target surfaces in good contact with one another, and to make sure the forces between the involved surfaces are well coordinated with the stacking steps.

The details of the stacking techniques must vary depending on the source of the 2D building blocks. For exfoliated 2D materials, the stacking process is well-developed. We now take the fabrication of graphene sandwiched between hBN films as an example to explain this process.

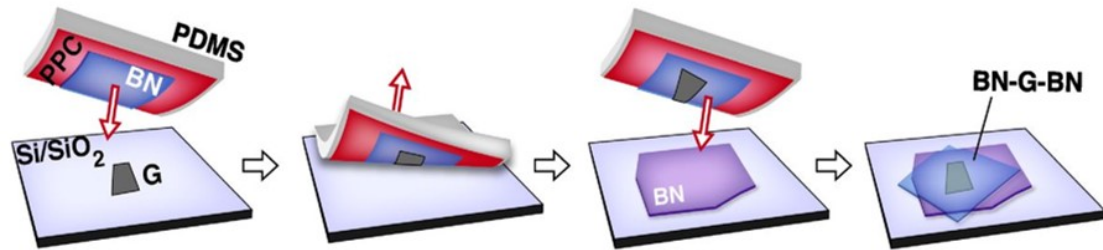


Figure 1.5: Polymer-free assembly of layered materials  
Schematic of the van der Waals technique for polymer-free assembly of layered materials. Adapted from Reference [15].

The steps for building graphene encapsulated by hBN are as illustrated in Figure 1.5. Two kinds of polymers, polydimethylsiloxane (PDMS) and polypropylene carbonate (PPC), are used. First, graphene and hBN are exfoliated onto a SiO<sub>2</sub>/Si substrate. Graphene and hBN pieces of desired thicknesses are manually selected using an optical microscope. Then, their surface cleanliness is confirmed by AFM measurements. The stacking goes as follows: at 40 °C, use the PPC on top of PDMS to pick up hBN, then graphene, followed by hBN, all from the SiO<sub>2</sub> substrate. Finally, at 90 °C, remove the PDMS from the stack. [15]

This process successfully generates high quality stacks for a few reasons. First, interlayer contamination is controlled at a very low level. The cleanliness

of the surfaces of the building blocks is confirmed by AFM. The interlayer is exposed to little polymer contaminants during stacking, and the amorphous carbon, which is unavoidable, is squeezed out and gathers in small puddles due to the van der Waals force. Second, good contact between layers during stacking is achieved. Since exfoliated samples are used, all the surfaces involved during stacking are flat. PDMS is elastic and can conform to the substrate. Additionally, the pieces being stacked are small in size. These three conditions make it easy to bring targeted surfaces together with good contact. Finally, the forces between surfaces are well coordinated with the stacking process. At 40 °C, the interaction strength follows this order: PDMS & PPC > PPC & hBN > 2D material & 2D material > 2D material & SiO<sub>2</sub>. At 90 °C, however, since the PPC is softened, the interaction between PPC and PDMS becomes the weakest and the stacked film can be put down to the final substrate.

The biggest advantage for exfoliated 2D material stacking is the high quality, but there are also downsides. First, since the exfoliated samples are of micrometer size, the stacking alignment would require micrometer precision, making the stacking rather time-consuming. Second, limited by the size of building blocks, the stacking of exfoliated 2D materials cannot be scaled up. We can avoid these two problems by using synthetic 2D materials as building blocks. However, new challenges arise with synthesis 2D building blocks. First, 2D synthesis films sit on top of growth substrates. The stacking process needs to ensure the removal of these substrates without degrading the 2D materials or leaving contaminants behind. Second, since not all growth substrates are flat and the samples are of large size, a special stacking process will be needed to bring the target surfaces in good contact. In this dissertation, one of our achievements is the development of a stacking technique for CVD graphene. Please refer to

chapter 3 for details.

## 1.5 Dissertation outline

As discussed in this chapter, the stacking of 2D materials is a powerful approach to manipulate the physical properties of 2D materials and to generate functional films. However, the realization of both of these features requires contamination-free stacked samples. To achieve this goal, both high-quality building blocks and well-engineered stacking techniques are essential. The stacking building blocks can be either exfoliated or synthetic 2D materials and the stacking techniques vary depending on the source of the building blocks. Currently, stacking is well-established for exfoliated 2D materials.

In this dissertation, we first focus on the building blocks. **Chapter 2** introduces the growth of wafer-scale homogeneous monolayer TMD films (mainly MoS<sub>2</sub>) using metal-organic chemical vapour deposition (MOCVD). The MOCVD method ensures precise control over precursor dynamics through the use of gas phase precursors. In this chapter, we provide details for growth optimization of MoS<sub>2</sub>; then, we list evidences to confirm the high quality and homogeneity of our films using various characterizations.

After introducing the growth work, we switch to 2D stacking. In chapter 3 and 4, we discuss a model stacking system — twisted bilayer graphene (tBLG), where film properties can be manipulated by stacking. In tBLG, twist angle ( $\theta$ ) serves as a key parameter for determining its physical properties. **In chapter 3**, a general discussion of tBLG is provided. We first talk about the electronic band structure and the  $\theta$ -dependent properties of tBLG; then introduce a vacuum-

assisted direct stacking technique that can generate high-quality  $\theta$ -controllable tBLG using CVD sample sources. **In chapter 4**, we focus on small- $\theta$  tBLG. After a discussion of the novel electrical properties of small- $\theta$  tBLG, we will introduce the mechanism of the Raman  $R'$  process in small- $\theta$  tBLG. Then, with a quantitative  $\theta$ -dependence study of the  $R'$  process, a  $\theta$  detection method is developed. Finally,  $\theta$ -dependent electronic features, a stacking-induced property change, will be discussed.

After the discussion of the property manipulation in the model system of tBLG, we will introduce our preliminary results on building functional films out of 2D material stacks. **In chapter 5**, we present our work which demonstrates a graphene field-effect transistor (FET) with stacked multilayer  $WS_2$  as the dielectric layer. Finally, **in chapter 6**, we will touch upon the future directions of 2D stacking.

## CHAPTER 2

### MOCVD SYNTHESIS OF TMD

#### 2.1 Introduction

TMDs can form stable three-atom-thick monolayers [1], of which the majority are semiconducting and the rest are metallic. Monolayer semiconducting TMDs provide ideal materials with high electrical carrier mobility [29,56–60] for atomically thin high-performance transistors and photodetectors. Monolayer metallic TMDs can serve as conducting wires and functional channels, such as superconducting channels [37] and spin injection sources [61], in atomically thin integrated circuitry. Additionally, both semiconducting and metallic TMDs can be building blocks for 2D stacking. By either serving in devices themselves or being building blocks in stacked 2D films, the unique electronic band structures and symmetry of TMDs can provide novel ways of enhancing the functionalities of such devices and stacked films, including the large excitonic effect [62], bandgap modulation [63], indirect-to-direct bandgap transition [28], piezoelectricity [64], and valleytronics [34].

Large-scale growth of TMDs on insulating substrates could, first, enable the batch fabrication of atomically thin high-performance devices; and second, enable large-scale 2D stacking. However, the large-scale growth of monolayer TMD films with spatial homogeneity and high electrical performance remains an unsolved challenge. Existing growth methods for large-scale monolayer TMDs have so far produced materials with limited spatial uniformity and electrical performance. For instance, the sulphurization of metal or metal compounds only provides control over the average layer number, producing spa-

tially inhomogeneous mixtures of monolayer, multi-layer and no-growth regions [65,66]. Although CVD based on solid-phase precursors (such as  $\text{MoO}_3$ ,  $\text{MoCl}_5$  or  $\text{WO}_3$ ) [67–72] has shown better thickness control on a large scale, the electrical performance of the resulting material, which is often reported from a small number of devices in selected areas, fails to show spatially uniform high carrier mobility.

In this chapter, we report a metal-organic chemical vapor deposition technique (MOCVD) for large-scale TMD synthesis. With this MOCVD technique, we demonstrate the synthesis of representative TMD materials, monolayers of  $\text{MoS}_2$  and  $\text{WS}_2$ , grown directly on insulating  $\text{SiO}_2$  substrates, with excellent spatial homogeneity and high mobility (an electron mobility of  $30 \text{ cm}^2 \cdot \text{V}^{-1} \cdot \text{s}^{-1}$  at room temperature and  $114 \text{ cm}^2 \cdot \text{V}^{-1} \cdot \text{s}^{-1}$  at 90 K for  $\text{MoS}_2$ ) over an entire 4-inch wafer. The versatility of this MOCVD technique is proven through the growth of large scale homogeneous monolayer in both materials ( $\text{MoS}_2$  and  $\text{WS}_2$ ) using similar growth parameters. Our MOCVD growth therefore provides a new avenue for the growth of various high-quality monolayer TMD films with different compositions and electrical properties, enabling the future development of large-scale 2D stacking and atomically thin integrated circuitry.

This chapter is adapted from the paper, “High-mobility three-atom-thick semiconducting films with wafer-scale homogeneity” [73], to which I am a contributing author (Kibum Kang and Saien Xie are the co-first authors). Data in Figure 2.6 a-c and e were generated by me.

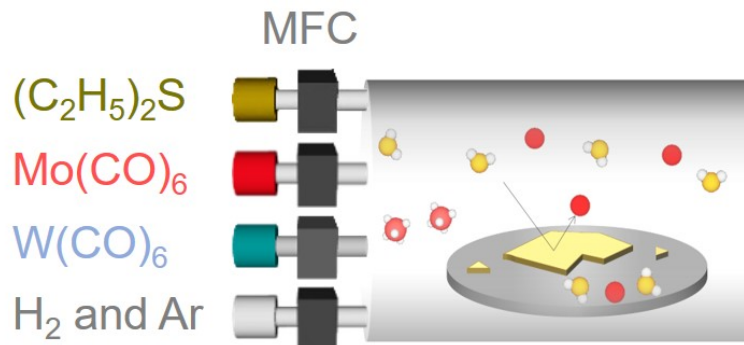


Figure 2.1: MOCVD growth setup

Precursors were introduced to the growth setup with individual mass flow controllers (MFCs). Red, Mo or W atoms; yellow, S atoms; white, carbonyl or ethyl ligands.

## 2.2 Growth method and optimization

Figure 2.1 schematically explains our MOCVD growth. The synthesis was carried out in a 4.3-inch (inner diameter) hot-wall quartz tube furnace.  $\text{Mo}(\text{CO})_6$ ,  $\text{W}(\text{CO})_6$ ,  $(\text{C}_2\text{H}_5)_2\text{S}$ , which have high equilibrium vapor pressure near room temperature, were selected as chemical precursors for Mo, W, S, respectively, and were introduced to the furnace in gas phase.  $\text{H}_2$  and Ar were injected to the chamber using separate lines. The concentration of each reactant can be precisely controlled throughout the growth time by regulating the partial pressure of each reactant with the mass flow controllers (MFCs).

With our MOCVD method, we carefully optimized  $\text{MoS}_2$  growth conditions, and our key findings are summarized in Figure 2.2 and Figure 2.3. First, our  $\text{MoS}_2$  film is grown in the layer-by-layer growth mode. Figure 2.2a shows optical images of  $\text{MoS}_2$  films, grown under the optimized growth condition, at different growth times, revealing the initial nucleation on the  $\text{SiO}_2$  surface ( $t =$

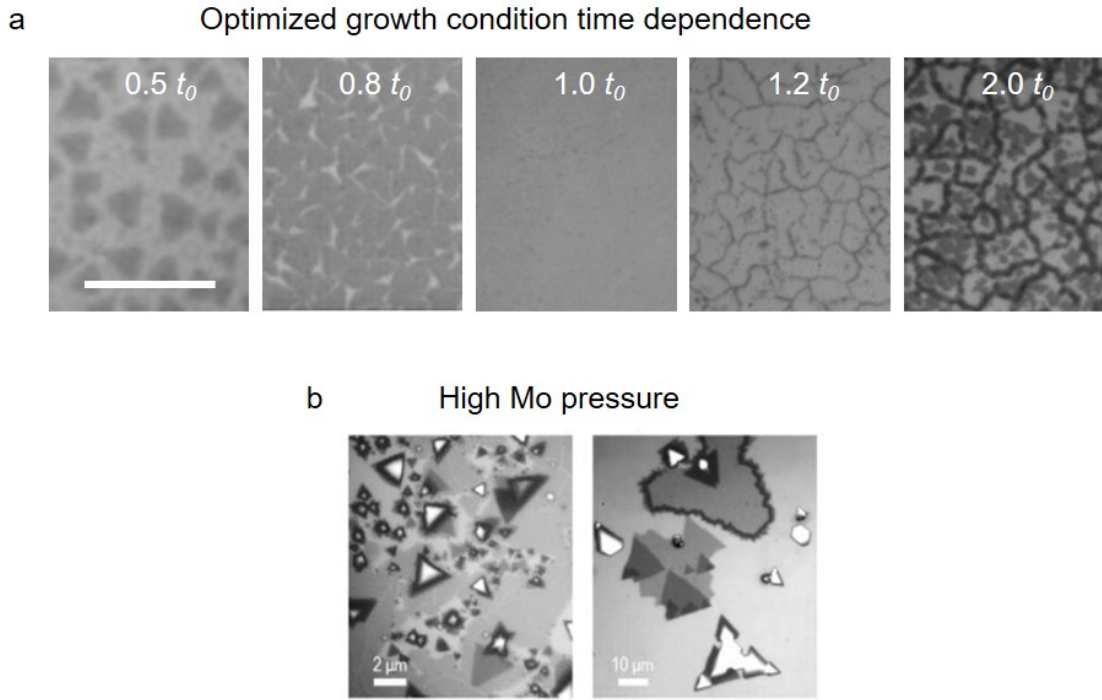


Figure 2.2: MOCVD layer-by-layer growth

(a) Optical images of MOCVD-grown  $\text{MoS}_2$  at the indicated growth times, where  $t_0$  was the optimal growth time for full monolayer coverage. Scale bar,  $10 \mu\text{m}$ . (b) Optical images of MOCVD-grown  $\text{MoS}_2$  with a high vapor pressure of Mo vapor, where a mixture of monolayer, multilayer and no-growth regions exist.

$0.5t_0$ ), subsequent monolayer growth near ( $0.8t_0$ ) and at the maximum monolayer coverage ( $t_0$ ), followed by nucleation mainly at grain boundaries ( $1.2t_0$ ) and bilayer growth ( $2t_0$ ). We observed no nucleation of a second layer while the first layer was forming (when  $t < t_0$ ), producing an optimal growth time  $t_0$  near full monolayer coverage. The standard thin-film growth model [74] suggests that this growth mode is effective below a certain deposition rate of the growth species, above which it suggests a different mode that forms thicker islands. Indeed, the layer-by-layer growth of the  $\text{MoS}_2$  film was observed only when we applied a low partial pressure (around  $10^{-4}$  Torr) of Mo vapor (produced by the thermal decomposition of  $\text{Mo}(\text{CO})_6$  in the presence of excess  $(\text{C}_2\text{H}_5)_2\text{S}$ . In con-

trast, as shown in Figure 2.2b, the growth at a higher Mo partial pressure was no longer in the layer-by-layer growth mode, instead simultaneously producing a mixture of monolayer, multilayer and no-growth regions. For the uniform monolayer growth over a large substrate, it is thus important to maintain a low Mo partial pressure constantly over the entire growth region and over time, the key technical capability provided by our MOCVD setup.

Our second finding is that the grain structure of our MoS<sub>2</sub> film, including the average grain size and the intergrain stitching, depends sensitively on the concentrations of H<sub>2</sub>, (C<sub>2</sub>H<sub>5</sub>)<sub>2</sub>S, and residual water. Figure 2.3a shows the two main effects of H<sub>2</sub>, whose presence is necessary for removing carbonaceous species generated during the MOCVD growth: the average grain size increases from hundreds of nanometers to more than 10 μm with decreasing H<sub>2</sub> flow, and the MoS<sub>2</sub> grains grown under higher H<sub>2</sub> flow have mostly perfect triangular shapes without merging with neighboring grains, a trend that disappears with lower H<sub>2</sub> flow. The dependence on H<sub>2</sub>O concentration was observed under the presence of salt desiccant (NaCl, KCl, NaBr), as shown in Figure 2.3b, where the grain size increases up to 100-fold. (Recently, a number of papers are published studying the effect of alkali metal halides in TMD growth. It is suggested that the effect of alkali metal halides may not be serving as a desiccant. Possible mechanisms are: alkali metal modifies the growth substrate and suppresses nucleation; the halogen vapor reacts with the transition metal precursor and assists precursor transfer [75–78]) Also, Figure 2.3c shows that the concentration of (C<sub>2</sub>H<sub>5</sub>)<sub>2</sub>S affects the grain size.

In order to explain these phenomena, we need to discuss the precursor decomposition and nucleation kinetics. First, according to hydrolysis and hy-

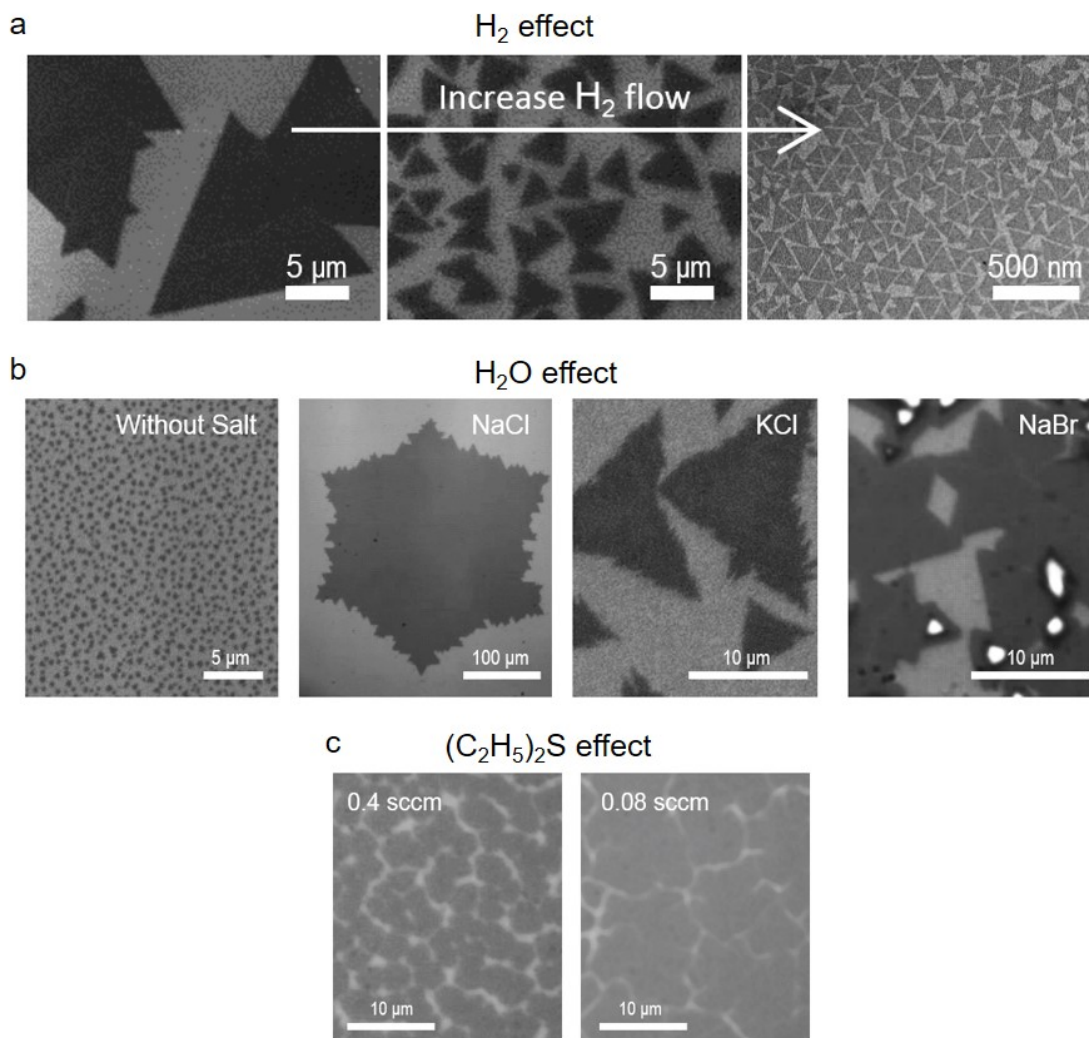


Figure 2.3: MoS<sub>2</sub> grain structure optimization

(a) Grain structure variation depending on H<sub>2</sub>. With H<sub>2</sub> increasing, grain size decreases and merging of grains is prohibited. (b) Grain structure variation depending on H<sub>2</sub>O. Grain size increases if desiccant exists. (c) Grain structure variation depending on (C<sub>2</sub>H<sub>5</sub>)<sub>2</sub>S. Grain size increases with decreased concentration of (C<sub>2</sub>H<sub>5</sub>)<sub>2</sub>S.

drogenolysis, H<sub>2</sub> [79] and H<sub>2</sub>O promote the decomposition of the (C<sub>2</sub>H<sub>5</sub>)<sub>2</sub>S precursor, which enhances the concentration of sulphur vapor. Also, the concentration of sulphur vapor linearly depends on the concentration of (C<sub>2</sub>H<sub>5</sub>)<sub>2</sub>S, since (C<sub>2</sub>H<sub>5</sub>)<sub>2</sub>S contains a certain ratio of S vapor. Second, the concentration of sulphur affects the nucleation kinetics and grain size. We make several assump-

tions here. (i) Our growth is Mo diffusion limited growth, since the Mo concentration is kept low for layer-by-layer growth. In comparison, the concentration of S vapor is much higher than that of Mo vapor. (ii) When a Mo atom produced by thermal decomposition of  $\text{Mo}(\text{CO})_6$  arrives at the surface, it diffuses until reacting with S. (iii) Energetically, Mo and S atoms prefer to be adsorbed at a  $\text{MoS}_2$  edge. (iv) If the concentration of S vapor is high, Mo atoms lose their chance to find energetically favorable positions and nucleation occurs at a non-edge region. Based on these assumptions, we conclude that the nucleation density of  $\text{MoS}_2$  increases on the surface when the decomposition kinetics of  $(\text{C}_2\text{H}_5)_2\text{S}$  becomes faster. Therefore, when  $\text{H}_2$ ,  $\text{H}_2\text{O}$ , and  $(\text{C}_2\text{H}_5)_2\text{S}$  concentrations are high, nucleation density increases and grain size decreases. For  $\text{H}_2$ , it also etches  $\text{MoS}_2$  [80], which prevents intergrain connection. To grow continuous monolayer  $\text{MoS}_2$  with a large grain size and high-quality intergrain stitching, we thus flowed optimal amounts of  $\text{H}_2$  and  $(\text{C}_2\text{H}_5)_2\text{S}$  and dehydrated the growth environment.

The optimum growth parameters for monolayer  $\text{MoS}_2$  is as follows. We use a total pressure of 7.5 Torr, growth temperature of 550 °C and growth time ( $t_0$ ) of 26 hrs. The flow rate of precursors is 0.01 sccm for  $\text{Mo}(\text{CO})_6$ , 0.4 sccm for  $(\text{C}_2\text{H}_5)_2\text{S}$ , 5 sccm for  $\text{H}_2$ , and 150 sccm for Ar. NaCl is loaded in the upstream region of the furnace as a desiccant to dehydrate the growth chamber. The main growth substrates are 4-inch fused silica wafers or 4-inch Si wafers with 285 nm thermal  $\text{SiO}_2$ .

The MOCVD growth is not subject to specific precursor-substrate chemistry, and is therefore highly versatile. We demonstrate the growth of  $\text{WS}_2$  using almost the same growth conditions as  $\text{MoS}_2$ , only changing the precursor from

Mo(CO)<sub>6</sub> to W(CO)<sub>6</sub>.

### 2.3 Optical and structural characterization of TMD

We confirm the quality, homogeneity, and continuity of our semiconducting monolayer MoS<sub>2</sub> and WS<sub>2</sub> films on a 4-inch wafer scale using various non-electrical methods, including optical microscopy, photoluminescence, Raman, TEM, etc.

Figure 2.4 presents our continuous TMD monolayer films and shows their wafer-scale homogeneity as well as intrinsic optical properties and chemical composition. The color photos of MoS<sub>2</sub> (Figure 2.4a; greenish yellow) and WS<sub>2</sub> (Figure 2.4b; yellow) films grown on a transparent 4-inch fused silica wafer show that the TMD grown region (right half) is uniform over the whole substrate and clearly distinguishable from the bare silica substrate (left half). The optical absorption, photoluminescence and Raman spectra measured from our films show characteristics unique to monolayer MoS<sub>2</sub> and WS<sub>2</sub>, respectively (Figure 2.4c-e). All of these measured spectra have the same peak positions as in exfoliated monolayer samples (denoted by diamonds) [28, 81–83], regardless of the location of the measurements within our films (Figure 2.4f). Figure 2.4g displays the X-ray photoelectron spectra taken from our monolayer MoS<sub>2</sub> films, which show almost identical features to those of bulk single crystal MoS<sub>2</sub> with low defect levels, further confirming the precise chemical composition and the high quality of our MoS<sub>2</sub> films.

Figure 2.5 focuses on the grain boundaries of the MoS<sub>2</sub> growth and proves the continuity of our films. Figure 2.5a and Figure 2.5b, the darkfield transmis-

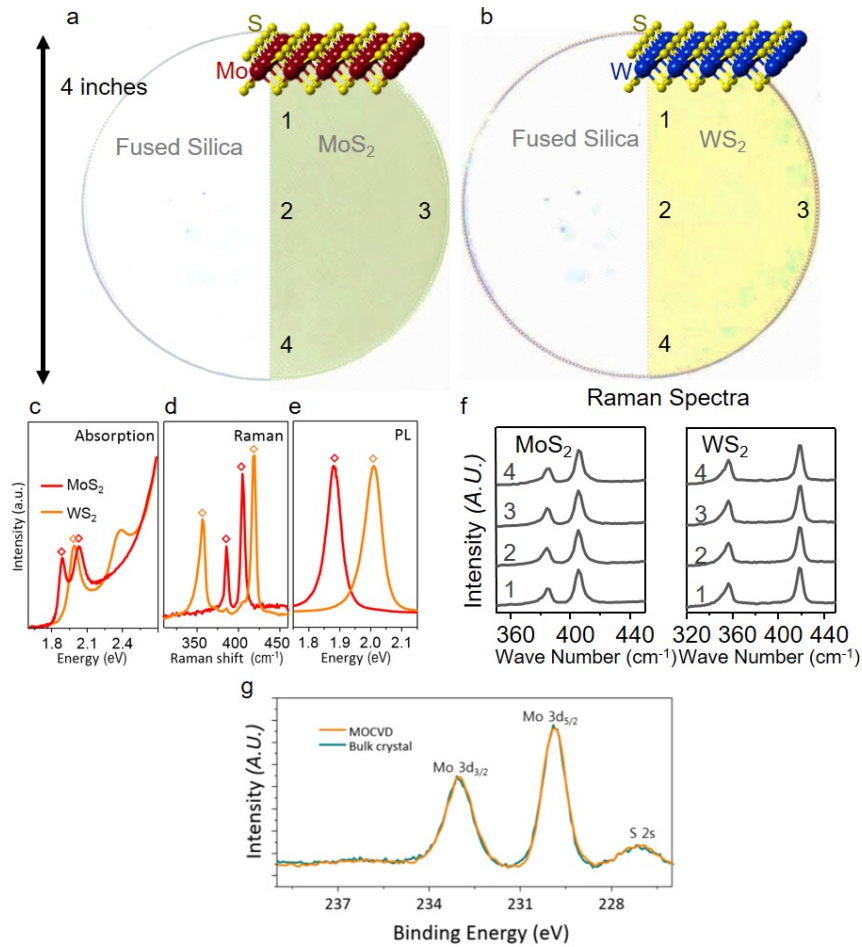


Figure 2.4: Wafer-scale homogeneous monolayer TMD films (a) and (b): Photographs of monolayer  $\text{MoS}_2$  (a) and  $\text{WS}_2$  (b) films grown on 4-inch fused silica substrates, with diagrams of their respective atomic structures. The left halves show the bare fused silica substrate for comparison. (c) Optical absorption spectra of MOCVD-grown monolayer  $\text{MoS}_2$  (red line) and  $\text{WS}_2$  (orange line) films in the photon energy range from 1.6 to 2.7 eV. (d) Raman spectra of as-grown monolayer  $\text{MoS}_2$  and  $\text{WS}_2$ , normalized to the silicon peak intensity. (e) Normalized photoluminescence spectra of as-grown monolayer  $\text{MoS}_2$  and  $\text{WS}_2$ . The peak positions in c-e are consistent with those seen from exfoliated samples (diamonds). (f) Raman spectra for  $\text{MoS}_2$  (left) and  $\text{WS}_2$  (right) respectively, taken at different locations marked on the corresponding fused silica wafer. (g) XPS spectra of Mo 3d 3/2, 5/2 and S 2s state for  $\text{MoS}_2$  grown by our method (orange) and bulk  $\text{MoS}_2$  single crystal (cyan blue), where the peak position and FWHM are almost identical.

sion electron microscope (DF-TEM) and annular darkfield scanning TEM (ADF-STEM) images, confirm the continuity on the nanometer and atomic length

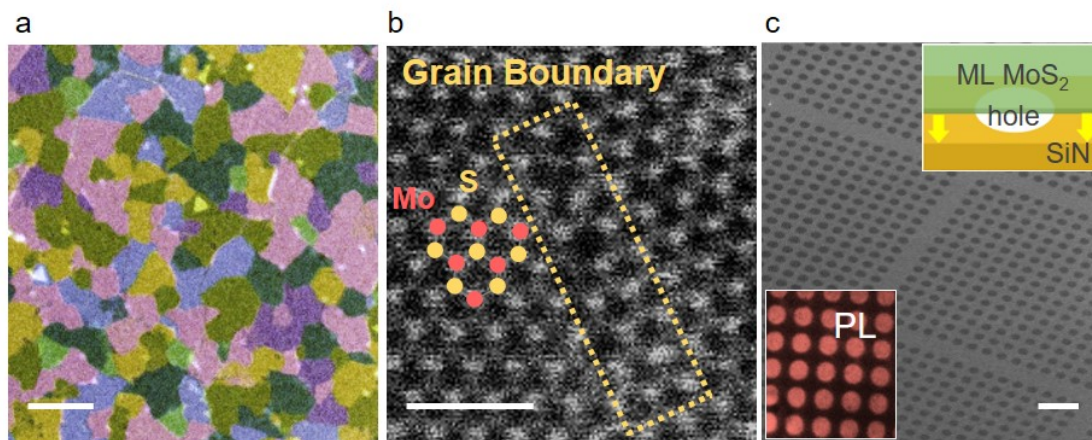


Figure 2.5: Continuity of monolayer MoS<sub>2</sub>  
 (a) False-color DF-TEM image showing a continuous monolayer MoS<sub>2</sub> film. Scale bar, 1 μm. (b) ADF-STEM image of a laterally stitched grain boundary in a monolayer MoS<sub>2</sub> film, with red and yellow dots representing the Mo and S atoms, respectively. Scale bar, 1 nm. (c) SEM image and photoluminescence (PL) image (bottom inset, at 1.9 eV) of monolayer MoS<sub>2</sub> membranes suspended over a SiN TEM grid with 2 μm holes (a diagram of the suspended film is shown in the top inset). Scale bar, 10 μm.

scales. The DF-TEM (Figure 2.5a) image shows a continuous polycrystalline monolayer film with no visible gaps and a bilayer area of less than 0.5%. Further analysis of the DF-TEM and electron diffraction data confirms a uniform angular distribution of crystal orientations with no preferred intergrain tilt angle for grain boundaries. The ADF-STEM data (Figure 2.5b) further confirms that adjacent grains are likely to be connected by a high-quality lateral connection with structures similar to those seen in previous reports [67,68]. Figure 2.5c shows a scanning electron microscope (SEM) image of an array of fully suspended monolayer MoS<sub>2</sub> membranes (2 μm in diameter), confirming the continuity on micrometer scale. This suspended structure is fabricated by transferring our grown film onto a SiN grid with holes. Its high fabrication yield (~99.5%) suggests mechanical strength and continuity of the film. The widefield photoluminescence images of these films (insets to Figure 2.5c) show strong, spatially

uniform photoluminescence signals, further confirming that they are continuous monolayer MoS<sub>2</sub>, with its high quality maintained even after transfer.

## 2.4 Electrical characterization of TMD

The electrical properties of our monolayer MoS<sub>2</sub> films have two important characteristics: spatial uniformity over a large scale and excellent transport properties similar to those seen in exfoliated samples. All our electrical measurements in Figure 2.6 (except those in Figure 2.6c and e) were performed at room temperature. Figure 2.6a shows a plot of sheet conductance ( $\sigma_{\square}$ ) against back gate voltage ( $V_{\text{BG}}$ ) measured from a monolayer MoS<sub>2</sub> FET (optical image shown in the inset) with multiple electrodes for the four-probe measurements (except for the channel length  $L$  of 34  $\mu\text{m}$ ). It includes several curves for different  $L$  ranging between 1.6 and 34  $\mu\text{m}$  (shifted from the bottom curve for clarity), all of which show nearly identical behaviors, including the n-type conductance, carrier concentration ( $\sim 4 \times 10^{12} \text{ cm}^{-2}$  at  $V_{\text{BG}} = 0 \text{ V}$ ) and high field-effect mobility ( $\mu_{\text{FE}}$ ). Figure 2.6b further plots  $\mu_{\text{FE}}$  measured from five such devices, fabricated at random locations and separated by up to 3.3 mm on a single chip. All the devices show similar  $\mu_{\text{FE}}$  near  $30 \text{ cm}^2 \cdot \text{V}^{-1} \cdot \text{s}^{-1}$ , independent of  $L$  and device location, suggesting the spatial homogeneity of the electrical properties of the MoS<sub>2</sub> film at length scales ranging from micrometers to millimeters.

The distribution of  $\mu_{\text{FE}}$  of our devices is compared with the results of multiple devices from two previous reports, each measured from individual grains of exfoliated [29] or CVD-grown MoS<sub>2</sub> samples [70]. We find that  $\mu_{\text{FE}}$  measured from our MOCVD film is similar to the median  $\mu_{\text{FE}}$  (denoted by a star) of exfo-

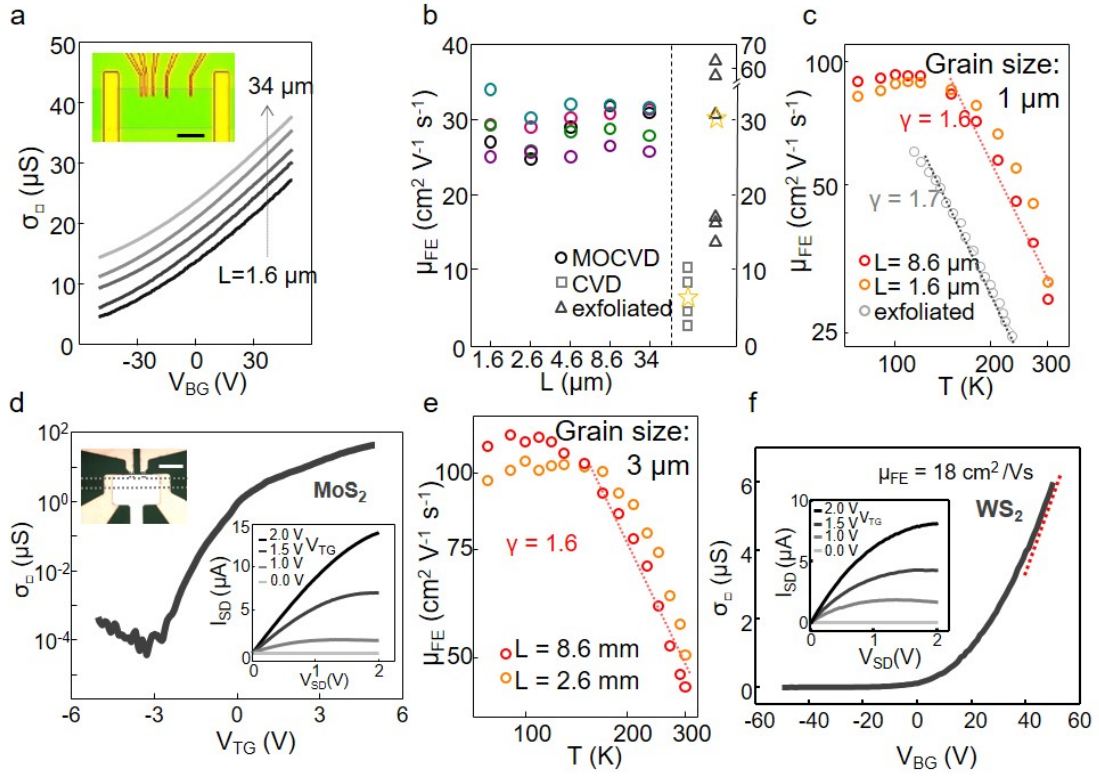


Figure 2.6: Electrical characterization of MoS<sub>2</sub> FETs

(a) Gate-dependent sheet conductance ( $\sigma_{\square}$ ) of monolayer MoS<sub>2</sub> FETs measured at different channel lengths  $L$  (curves displaced from the bottom for clarity). Inset: optical image of the device; scale bar, 10  $\mu\text{m}$ . (b) Field effect mobility ( $\mu_{\text{FE}}$ ) measured from five MoS<sub>2</sub> FETs (ellipses) fabricated at random locations with different  $L$ . Data from previous results for CVD-grown samples [70] (squares) and exfoliated samples [29] (triangles) are shown for comparison (yellow stars indicate their medians). (c) Temperature dependence of  $\mu_{\text{FE}}$  measured from the device in Figure 2.6a at  $L = 1.6 \mu\text{m}$  (orange) and  $8.6 \mu\text{m}$  (red), and from a previous report on exfoliated samples (grey) [57], both showing phonon-limited intrinsic transport. (d) Top gate ( $V_{\text{TG}}$ )-dependent  $\sigma_{\square}$  for dual-gate monolayer MoS<sub>2</sub> FET (device shown in the upper inset). Lower inset:  $V_{\text{TG}}$ -dependent  $I_{\text{SD}}-V_{\text{SD}}$  curves showing current saturation and ohmic electrode contact. Scale bar, 10  $\mu\text{m}$ . For a-d, MoS<sub>2</sub> grain size is 1  $\mu\text{m}$ . (e) Temperature dependence of  $\mu_{\text{FE}}$  measured from MoS<sub>2</sub> film of grain size 3  $\mu\text{m}$ , with different channel lengths, which show the same dependence as shown in Figure 2.6c. (f) Gate-dependent  $\sigma_{\square}$  of a monolayer WS<sub>2</sub> FET showing  $\mu_{\text{FE}} = 18 \text{ cm}^2/\text{Vs}$ . Inset:  $V_{\text{TG}}$ -dependent  $I_{\text{SD}}-V_{\text{SD}}$  curves showing current saturation and ohmic electrode contact.

liated samples (and several times higher than the CVD results) and has a much narrower distribution. In addition, the temperature dependence of  $\mu_{\text{FE}}$  (Fig-

ure 2.6c) measured from the same device in Figure 2.6a shows higher  $\mu_{FE}$  at lower temperatures ( $92 \text{ cm}^2 \cdot \text{V}^{-1} \cdot \text{s}^{-1}$  at 100 K) and intrinsic, phonon-limited electron transport similar to the behaviors previously observed in exfoliated samples (data from Reference [57] shown in Figure 2.6c) but different from those observed from a CVD sample with stronger effects from defects [84]. Specifically, our data show that the temperature dependence of mobility follows a power law of  $\mu_{FE} \approx T^{-\gamma}$  with exponent  $\gamma = 1.6$  for temperatures between 150 and 300 K, close to the value (1.69) [56] predicted by theory and consistent with results from previous experiments (average value ranging between 0.6 and 1.7) [29, 57–59] for a similar temperature range. Finally, Figure 2.6d shows a high-performance MoS<sub>2</sub> FET fabricated with an individual top-gate electrode ( $V_{TG}$ ). It has a high on/off conductance ratio ( $\sim 10^6$ ), current saturation at relatively low bias  $V_{SD}$  (lower inset to Figure 2.6d) and high field-effect mobility ( $\sim 29 \text{ cm}^2 \cdot \text{V}^{-1} \cdot \text{s}^{-1}$ ), both are comparable to the best reported results [29, 57, 58]. We note that our devices studied in Figure 2.6a-d were fabricated at random locations using a polycrystalline monolayer MoS<sub>2</sub> film, unlike the devices with single grain samples used for comparison. In addition, the electrical properties measured from a separate monolayer MoS<sub>2</sub> film with a larger average grain size of  $3 \mu\text{m}$  are almost identical to those of the  $1 \mu\text{m}$  grain size film in Figure 2.6a-d, including the channel-length independence of  $\mu_{FE}$  and the phonon-limited transport at  $T > 150 \text{ K}$  (see Figure 2.6e; with the low-temperature mobility as high as  $114 \text{ cm}^2 \cdot \text{V}^{-1} \cdot \text{s}^{-1}$  at 90 K).

Taken together, our data confirm the spatial uniformity and high electrical performance of our MoS<sub>2</sub> FETs independent of the average grain size, which suggests that the intergrain boundaries in our films do not significantly degrade their electrical transport properties. This is probably due to the formation

of well-stitched intergrain boundaries with a low level of defects, an explanation also supported by the ADF-STEM (Figure 2.5b) and X-ray photoelectron spectrum data (Figure 2.4g) discussed above. Our data therefore lead us to conclude that our optimized MOCVD growth provides an electrically homogeneous monolayer MoS<sub>2</sub> film.

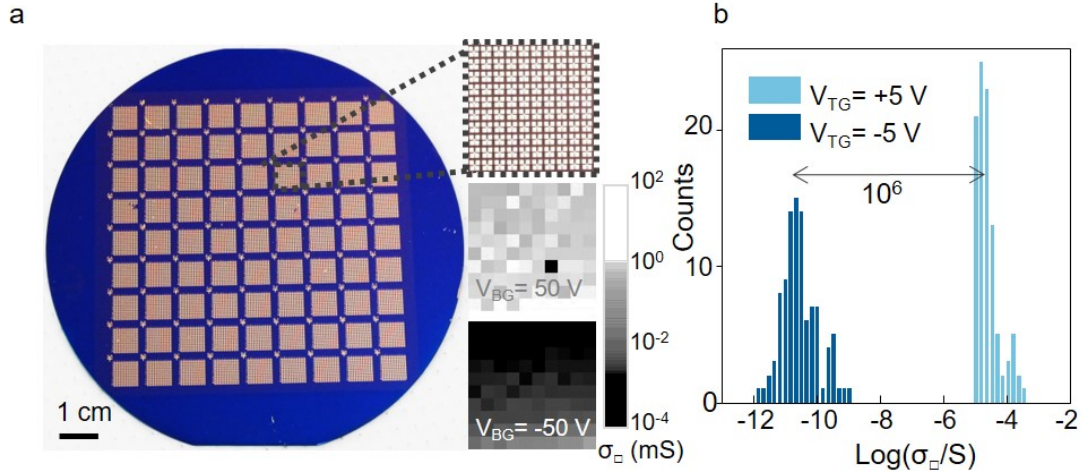


Figure 2.7: MoS<sub>2</sub> wafer-scale FETs

(a) Batch-fabricated 8,100 MoS<sub>2</sub> FET devices on a 4-inch SiO<sub>2</sub>/Si wafer. Top inset: enlarged image of one square containing 100 devices. Middle and bottom insets: corresponding color maps of  $\sigma_{\square}$  at gate bias  $V_{BG} = 50$  V and -50 V, respectively, with the black block in the middle inset representing the only non-conducting device. (b) Histogram of on-state and off-state  $\sigma_{\square}$  of 100 dual-gate FETs showing a median on-off ratio of  $10^6$  and a high on-state conductivity. Dark blue,  $V_{TG} = -5$  V; pale blue,  $V_{TG} = +5$  V. All measurements were performed at room temperatures.

The structural and electrical uniformity of our MoS<sub>2</sub> film enables the wafer-scale batch fabrication of high performance FETs as demonstrated in Figure 2.7. Figure 2.7a shows a photograph of 8,100 MoS<sub>2</sub> FETs with a global back gate, which were fabricated on a 4-inch SiO<sub>2</sub>/Si wafer using a standard photolithography process. The middle and bottom insets to Figure 2.7a show color-scale maps of  $\sigma_{\square}$  measured from 100 MoS<sub>2</sub> FETs in one square region at  $V_{BG} = 50$  V and -50 V, respectively; the top inset to Figure 2.7a shows an enlarged opti-

cal image of the devices. We observed an almost perfect device yield of 99%; only two out of 200 FETs that we characterized (including data from an adjacent region) did not conduct. Our data also confirm the spatially uniform n-type transistor operation (larger  $\sigma_{\square}$  for positive  $V_{\text{BG}}$ ) with similar  $V_{\text{BG}}$  dependence for all our devices and high on-state device conductance. We fabricated 100 individually addressable dual-gate MoS<sub>2</sub> FETs (similar to the device in Figure 2.6d) on another wafer. The histogram of the on-state  $\sigma_{\square}$  ( $V_{\text{TG}} = 5$  V; median carrier concentration  $\sim 7 \times 10^{12}$  cm<sup>-2</sup>) and off-state  $\sigma_{\square}$  ( $V_{\text{TG}} = -5$  V) collected from all such FETs (Figure 2.7b) shows strong peaks above  $10^{-5}$  S and near  $10^{-11}$  S, respectively, confirming a uniform conductance switching behavior with high on-state  $\sigma_{\square}$  ( $>10$  S) and on-off ratio ( $>10^6$ ).

The data presented in Figures 2.4-2.7 confirm the structural and electrical uniformity of the wafer-scale monolayer MoS<sub>2</sub> film grown by our MOCVD method. Moreover, we successfully fabricated and measured 60 FETs by using a monolayer WS<sub>2</sub> film. Even though the growth of monolayer WS<sub>2</sub> was not carefully optimized, these devices showed excellent electrical properties, with their  $\mu_{\text{FE}}$  as high as  $18$  cm<sup>2</sup>·V<sup>-1</sup>·s<sup>-1</sup> at room temperature (Figure 2.6f) and a median  $\mu_{\text{FE}}$  of  $5$  cm<sup>2</sup>·V<sup>-1</sup>·s<sup>-1</sup>. In addition, the WS<sub>2</sub> device in Figure 2.6f showed a high on/off ratio of  $10^6$  and the current saturation behavior (inset to Figure 2.6f) as in our MoS<sub>2</sub> devices.

## 2.5 Summary

Our high-mobility monolayer TMD films by MOCVD growth can be used immediately for the batch fabrication of TMD-based integrated circuitry on a tech-

nologically relevant wafer scale, and can also serve as building blocks for 2D stacking. In addition, because our MOCVD growth is controlled by the kinetics of the precursor supply rather than specific precursor-substrate chemistry (an example of the latter would be the different graphene growth modes on copper and nickel), its use is not limited to the TMD-substrate combinations reported here. Instead, this method can be generalized for producing various TMD materials, both semiconducting (for example  $\text{MoSe}_2$  or  $\text{WTe}_2$ ) and metallic (for example  $\text{NbSe}_2$  or  $\text{TaS}_2$ ), with precise layer control over a large scale. Indeed, our data show, as an initial demonstration, monolayer TMD growth of  $\text{WS}_2$ . Our versatile MOCVD growth therefore provides a new avenue for the growth of multiple high-quality monolayer TMD films with different compositions and electrical properties on a single substrate, enabling the future development of 2D stacking and atomically thin integrated circuitry.

## CHAPTER 3

### MODEL STACKING SYSTEM: TWISTED BILAYER GRAPHENE

#### 3.1 Introduction

As discussed in the chapter 1, for stacked 2D materials systems, interlayer van der Waals interactions introduce a new degree of freedom: the interlayer rotation angle  $\theta$ , which can be a key parameter for determining the physical properties of the stacked materials. Twisted bilayer graphene (tBLG) is a prototypical layered 2D material system, where  $\theta$  serves as a key parameter. tBLG can be viewed as a defective form of Bernal stacked bilayer graphene, in which the two graphene layers, instead of having the same crystal orientation, are stacked on top of the each other with a crystal orientation mismatch  $\theta$ . tBLG exists, for a significant portion, in graphene samples prepared via CVD growth. In tBLG, interlayer interactions alter the band structure and create new van Hove singularities (vHS) and mini-gaps whose energy levels are monotonically tuned by the twist angle  $\theta$  [49, 85–88]. This leads to features such as  $\theta$ -dependent optical resonances between vHS [3, 5, 6] and electronic transport changes [89] when the Fermi level reaches the vHS and mini-gaps.

In this chapter, we will first review this prototypical layered 2D material system — tBLG, focusing on its  $\theta$ -dependent properties. Then we will introduce our vacuum-assisted direct stacking technique that generates  $\theta$ -controlled high-quality tBLG on a large scale.

## 3.2 Electronic band structure

We can better understand the electronic band structure of tBLG by comparing it with single layer graphene (SLG) and Bernal stacked bilayer graphene (Bernal BLG).

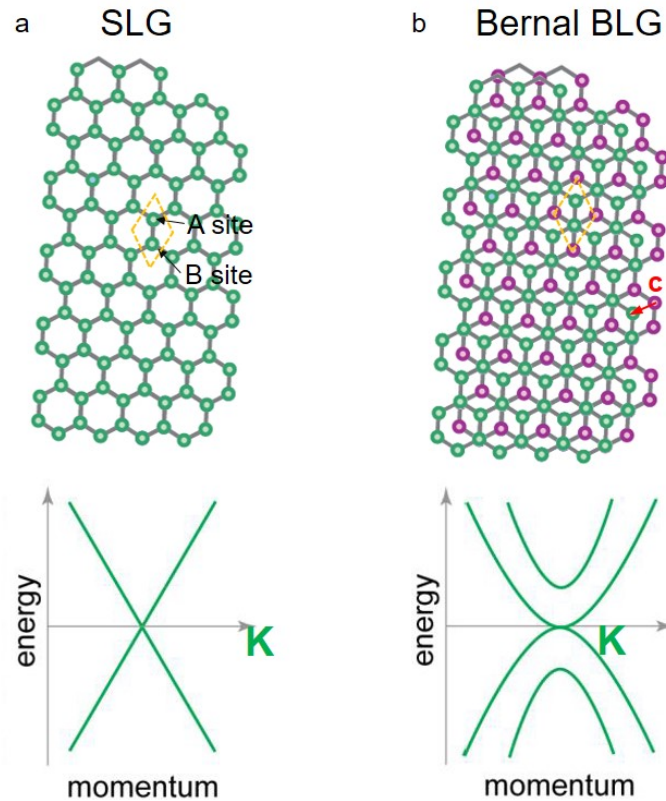


Figure 3.1: Crystal and electronic structure of SLG and Bernal BLG  
(a) Single layer graphene. (b) Bernal stacked bilayer graphene. The unit cell is indicated by the yellow dashed frame

As plotted in Figure 3.1a, SLG has a honeycomb lattice structure; its unit cell contains 2 atoms, A site and B site carbons. Its band structure reveals a gapless linear dispersion - the Dirac cone in the low energy range around the K and K' point. The most exciting electronic property of graphene, the ultrahigh mobil-

ity, comes from this linear band distribution and large momentum separation between the K and K' points. The band structure of SLG can be calculated using the tight binding method. Actually, the tight binding calculation of SLG, first presented by Wallace in 1947 [90] as a first step towards the calculation of the band structure of graphite, is a classic example of a tight binding calculation, and is often used in text books.

As plotted in Figure 3.1b, Bernal BLG is made up of two SLG layers that have the same crystal orientation but are shifted relative to each other by a vector  $\mathbf{c}$ . It has a unit cell that contains four carbon atoms. Similar to SLG, its band structure can be calculated using the tight binding model. The difference is that, for Bernal BLG, we need to consider the interactions from higher-order nearest neighbor atoms. [91] The band distribution of Bernal BLG near K and K' point is quadratic. One outstanding property of Bernal BLG is that, by breaking the inversion symmetry between the two layers by applying a vertical electric field, a tunable band gap can be opened. [92]

Now, let us look at tBLG. As discussed earlier, tBLG is made up of two layers of SLG which are stacked on top of each other with a crystal orientation mismatch  $\theta$ . Due to the stacking of two rotated crystalline films, a quasi-periodic moiré pattern would be formed. It is called quasi-periodic, because there might be small differences in crystal structure between those “repeating” units of the moiré pattern. These differences would cause the size of the primitive unit cell to differ from the moiré pattern unit cell. Depending on  $\theta$ , some tBLG has a primitive unit cell that is the same as the moiré pattern unit cell; some tBLG has a primitive unit cell that is bigger than the moiré pattern unit cell; and for some  $\theta$ , the size of the primitive unit cell is infinite. The first two of these three

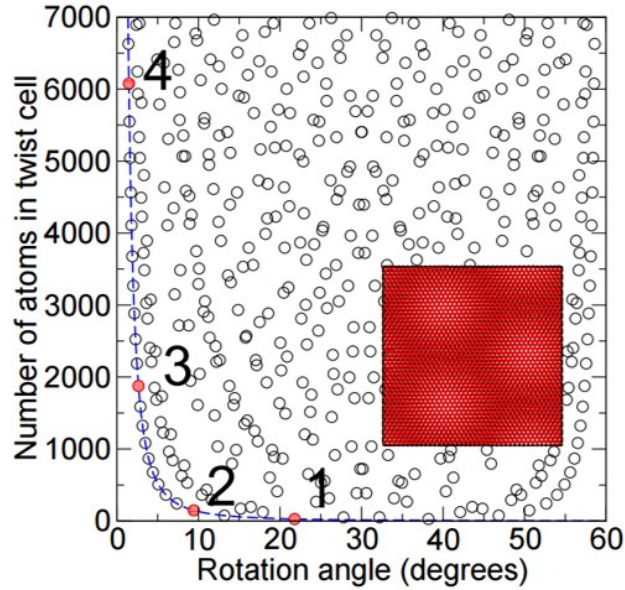


Figure 3.2: tBLG unit cell size vs.  $\theta$

A plot of the unit cell size vs.  $\theta$  for tBLG. This plot illustrates how a very small change in  $\theta$  can lead to a very large change in unit cell size. The dashed line corresponds the lower bound. For commensuration cells that fall on this line, the moiré periodicity is equal to the commensuration periodicity. This figure is adapted from Reference [93].

types of tBLG are called commensurate tBLG. Figure 3.2 shows the correlation between twist angle and the unit cell size for commensurate tBLG. It is clear from this figure that the unit cell size of tBLG does not change monotonically with  $\theta$ . tBLG with infinite unit cell size is called incommensurate tBLG. However, even for incommensurate tBLG, there is still a finite size moiré pattern unit cell (except when  $\theta$  goes to 0). In Figure 3.2, the dashed blue line indicates the size of moiré pattern unit cell, which changes smoothly and monotonically with the twist angle  $\theta$ .

These special structural properties make the band structure calculation of

tBLG complicated. For standard calculation methods, such as tight binding and ab initio, the calculation is carried out by modeling the inter-atomic interactions in a unit cell. The bigger the unit cell is, the more complicated this calculation will be, and the more computational power is required. To calculate the band structure of tBLG with an incommensurate angle or an angle corresponding to large unit size, standard methods can be time-consuming or even fail. However, according to experimental results, quite interestingly, the properties of tBLG that are generated by interlayer interactions change smoothly corresponding to the changes in twist angle  $\theta$  [49, 85–88]. To better capture this smooth angle dependence, a simplified model was proposed, in which the band structure of tBLG is viewed as the sum of two SLG with a small amount of modification introduced by interlayer interactions [6, 85]. Details for this band structure picture is presented as following.

Figure 3.3 shows both real and reciprocal space pictures of tBLG with a twist angle  $\theta$ . Figure 3.3a presents the crystal structure, drawn in the real space, in which the top layer is coloured green and the bottom layer is coloured purple. Figure 3.3b shows the band structure in the low energy range, drawn in the reciprocal space. This is a super-position of two SLG Brillouin zones with a relative rotation angle equal to  $\theta$ . As we already know, in low energy range, the band structure of SLG is a set of Dirac cones near the K and K' points. Figure 3.3b plots the Dirac cones at the K point from both the top and the bottom layers. The two Dirac cones cross each other at a certain energy. The larger the twist angle, the further apart the two Dirac cones, and the higher in energy this crossing will occur. Figure 3.3c pictures the intersection of the two Dirac cones along the plane going through the top and bottom layer K points and orthogonal to the crystal plane. As indicated in Figure 3.3c, at the place where the two Dirac

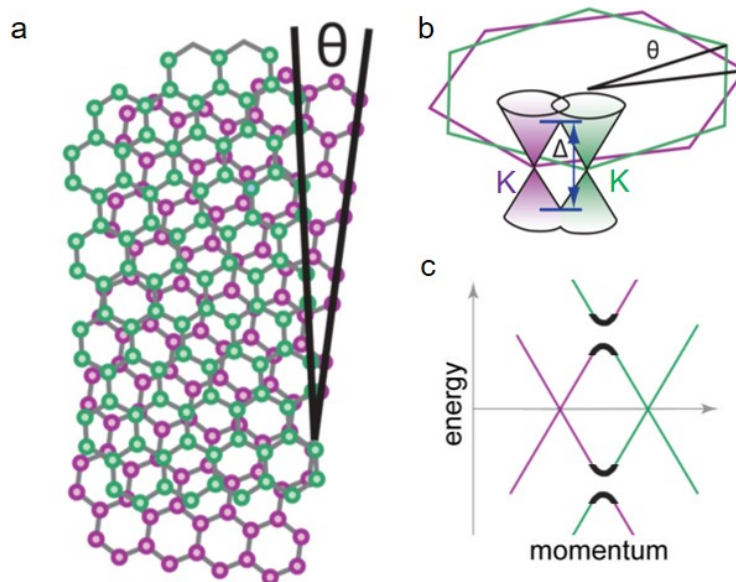


Figure 3.3: Crystal and electronic structure of tBLG

(a) The crystal structure of tBLG with a twist angle  $\theta$ . (b) Two Dirac cones from the top (green) and bottom (purple) layers are overlaid on top of each other, forming vHS states separated by energy  $\Delta$ . (c) Intersection of the two overlapping Dirac cones.

cones cross each other, interlayer interactions result in the opening of a mini band gap, and vHS states form on the gap edge. This band structure picture is directly supported by the angle-resolved photoemission spectroscopy (ARPES) data plotted in Figure 3.4, which is adopted from a paper published by Taisuke Ohta and coworkers [88].

As you may have noticed already, so far, we have only discussed the K point Dirac cones. The Dirac cones in the  $K'$  points should be taken into consideration as well. In tBLG, there are two kinds of crossings: the one between the K (or  $K'$ ) point Dirac cone of the top layer and the K (or  $K'$ ) point Dirac cone of the bottom layer (showed in Figure 3.3b), and the one between K (or  $K'$ ) point Dirac cone of the top layer and  $K'$  (or K) point Dirac cone of the bottom layer (not

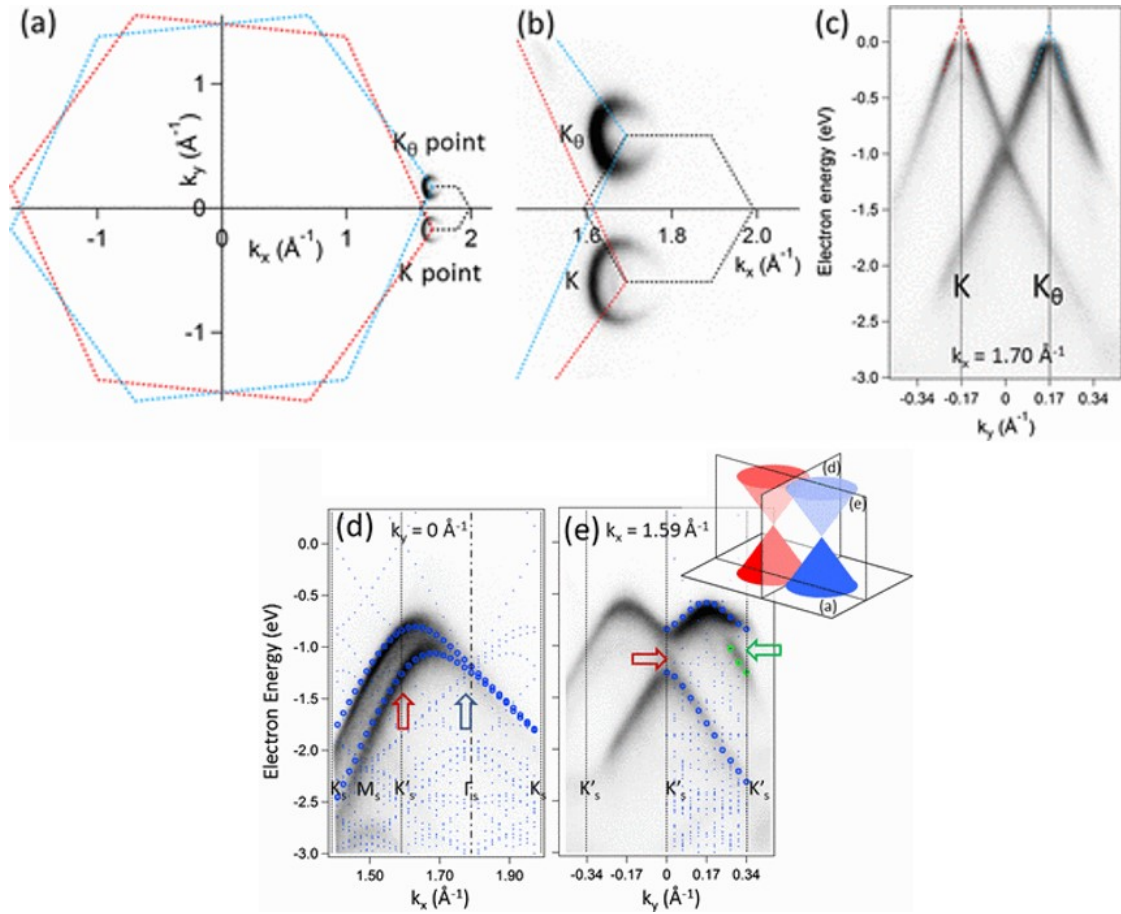


Figure 3.4: ARPES data from tBLG

(a) Photoemission intensity contour of the two Dirac cones at the electron energy of 0.4eV. (b) Enlarged image of (a) near the two cones. (c) Photoemission spectra intersecting the two cones at the top and bottom layer K points. (d) Photoemission spectra and the DFT calculations (blue and green dots) bisecting the two cones and (e) the one orthogonal to (d). The schematic to the right of (e) shows the orientations of the photoemission patterns relative to the two primitive Dirac cones without interaction. This figure is adapted from Reference. [88]

plotted out in Figure 3.3b). These two kinds of crossings happen at different energies and also have different chirality. [94] For the tBLG plotted in Figure 3.3, the lower energy crossing is left-handed and the higher energy crossing is right-handed. In most experiments, the lower energy one is measured for the following reasons. First, the higher energy crossings go to UV which is outside the measured range for most experiments. Second, we expect a weaker optical

signal from the higher energy crossing. In the band structure, at the same energy level, there are both single partical bands (where band structure is the same as SLG) and renormalized bands (where band crossing happens). At high energy level, single partical bands have high density of states which would weaken the effect of band renormalization to the total density of states. In later discussions, we will refer the energy of the vHS excitations for the lower energy crossing as  $E_A$  and higher energy crossing as  $E_B$ .

Depending on whether chirality is considered, there are different angle ranges for twist angle  $\theta$ . When considering chirality, the twist angle  $\theta$  ranges from  $0^\circ$  to  $60^\circ$ . Twist angle  $x^\circ$  and  $(60-x)^\circ$  are different because the chirality is different. If ignoring chirality,  $x^\circ$  and  $(60-x)^\circ$  are the same and  $\theta$  only ranges from  $0^\circ$  to  $30^\circ$ .

This simplified model works surprisingly well. It predicts many  $\theta$ -dependent properties of tBLG with both qualitative and quantitative accuracy. [7] However, it also has its limits. First, it is a single particle picture. The band gap opening at the band crossing point is a forced result, not something deduced by considering the detailed interlayer interaction. As a result, this model fails to explain the detailed band structure. A good practice would be to combine both this simplified model and a model which actually considers interlayer interactions together to explain or predict actual physical properties. The second limit is that, when  $\theta$  is small and the size of the mini-gap is comparable to the energy between vHS, this picture can no longer describe the band structure. For such cases, treating the moiré pattern as a long-wavelength structural perturbation for each layer would be a good theory to which to turn. This theory is called the continuum model [95].

### 3.3 Angle-dependent properties of tBLG

As discussed in section 3.2, in tBLG, interlayer interactions alter the band structure and create new vHS and mini-gaps whose energy levels are monotonically tuned by the twist angle  $\theta$ . This leads to many  $\theta$ -dependent features. In this section, we will review these features.

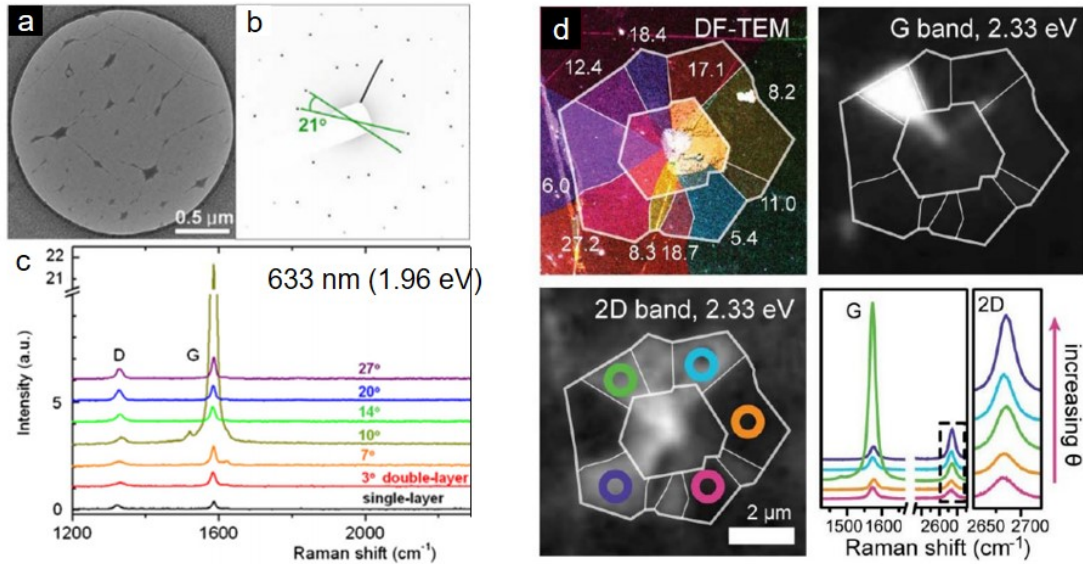


Figure 3.5: tBLG Raman G peak angle dependence

(a) TEM image of misoriented double-layer graphene. (b) Diffraction pattern of the graphene sample shown in (a). (c) Raman spectra of tBLG samples measured with 633 nm wavelength laser (1.96 eV). The spectra are shifted vertically for clarity. (d) Dark-field TEM, G band, and 2D band Raman images of the same multilayer tBLG sample. The twist angles are identified with dark-field TEM and are labeled for each domain in the TEM image. Raman spectra for several domains are also shown. (a)-(c) is adapted from Reference [5] and (d) is adapted from Reference [6].

Figure 3.5 displays the experimental results of  $\theta$ -dependent Raman G peak of tBLG, adapted from two independent reports [5,6]. In both works, the electron diffraction pattern from TEM is used to measure the twist angle  $\theta$ . The experimental data show that under a fixed optical excitation, among all differ-

ent  $\theta$  ranging from  $0^\circ$  to  $30^\circ$  (chirality is not involved in this case), there is one twist angle that is on resonance with the excitation photon energy and reveals a dramatically enhanced G peak in the Raman spectrum.

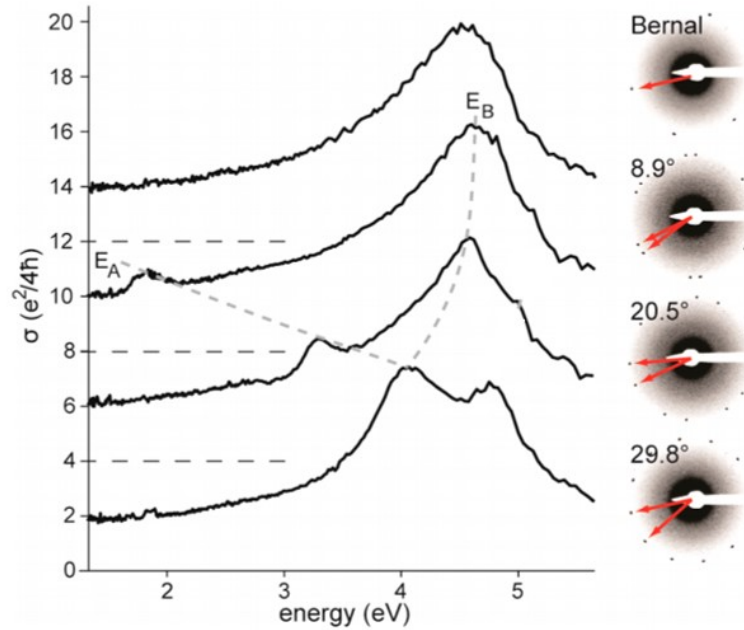


Figure 3.6: tBLG optical absorption angle dependence (left) Measured optical absorption spectra of Bernal BLG (top) and tBLG with increasing  $\theta$ . Dashed lines are guides to the eye indicating three features in the optical absorption spectra of tBLG which are not found in BLG. Spectra are offset in by  $4e^2/4\hbar$  a piece for clarity. (right) Electron diffraction patterns from the same tBLG regions, indicating  $\theta$  for each. This figure is adapted from Reference [7].

Figure 3.6 displays the  $\theta$  dependence of tBLG optical absorption. As in Figure 3.5, the  $\theta$  of the tBLG is quantitatively measured by TEM. According to the results, there are extra optical absorption peaks for different  $\theta$  tBLG, compared with Bernal BLG. The lowest energy peak has an energy that increases with  $\theta$ ; the higher energy peak has an energy that decreases with  $\theta$ . (A third peak appears in large  $\theta$  tBLG, which comes from the M point vHS of SLG)

The  $\theta$  dependence for both Raman G peak and optical absorption comes from

the new vHS states created by interlayer interaction, and can be explained using the simplified model we introduced in chapter 3.2. For Raman G peak enhancement, when the incoming laser excitation energy matches with  $E_A$ , the vHS excitation from the lower energy Dirac cone crossing, Raman resonance happens. For a fixed excitation laser energy, the higher the excitation energy, the larger the on-resonance angle will be. This agrees with data in Figure 3.5: 1.96 eV laser excitation is on resonance with  $10^\circ$  tBLG and 2.33 eV laser is on resonance with  $12^\circ$  tBLG. For optical absorption, absorption enhancement occurs when the energy of incoming light matches with  $E_A$  or  $E_B$  (the vHS excitations from the lower or the higher energy Dirac cone crossing).

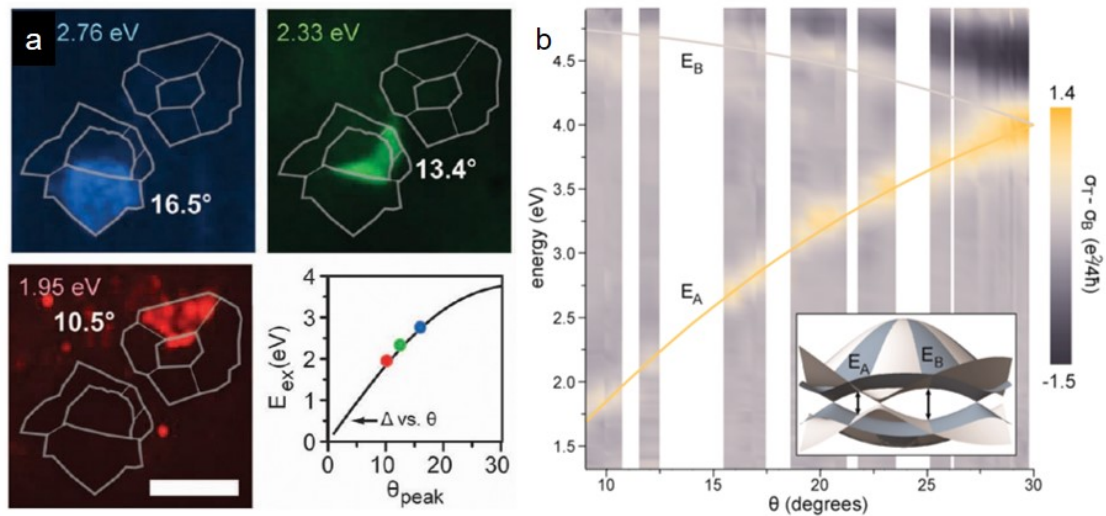


Figure 3.7: Quantitative analysis of tBLG  $\theta$  dependence

(a) Widefield G band images of the same tBLG regions at three different excitation wavelengths. A different domain exhibits strong G band enhancement in each image (scale bar  $5 \mu\text{m}$ ). Plotted are excitation energy vs the  $\theta$  correlated to maximum Raman G peak intensity for each of our available excitation wavelengths, based on data from many samples. The solid line is calculation result from the single particle model with a 4% increase in energy. (b) A 2D plot that combines the spectral differences between optical absorption in tBLG and Bernal BLG for all different  $\theta$  tBLG samples. The two main features,  $E_A$  and  $E_B$ , are fit to the simplified model described in section 3.2 (inset) with a 4% increase in energy. (a) is adapted from Reference [6]. (b) is adapted from Reference [7].

Figure 3.7 summarizes the comparison between the experimental data and the resonance peak calculated using the simplified model. The calculation is done simply by solving the crossing point of two rotated single layer graphene Brillouin zones. As presented in Figure 3.7, with a 4% increase in energy, the calculation matches almost perfectly to the experimental data.

One thing you might have already noticed is that, while on resonance, the Raman G peak is enhanced by a much larger amount than the optical absorption. This is because an optical absorption process only involves the photon absorption step, while a Raman process involves photon absorption, electron and/or hole scattering with phonons, and photon emission. The scattering step can happen through different pathways. For off-resonance tBLG or SLG, a large number of those scattering pathways interfere destructively during the G peak process, while for on-resonance tBLG, dramatic signal increase occurs due to the fact that interlayer interaction alters the band structure and blocks many destructive pathways. [6,96]

So far, we have discussed the  $\theta$ -dependent interlayer-interaction-induced optical properties in tBLG that do not involve chirality. Now let us take a look at the chirality of tBLG. Figure 3.8 displays data from a tBLG  $\theta$ -dependent circular dichroism (CD) study [94]. The CD spectra of both left-handed and right-handed tBLG with different  $\theta$  are plotted. It can be seen that, first, for a tBLG sample, there is one peak and one valley in the CD spectrum. Second, for tBLG with the same  $\theta$ , left-handed and right-handed samples have opposite CD spectra: the energy where the peak appears in one is the energy where valley appears in the other. Third, the energy where the peak and valley are located depends on  $\theta$ .

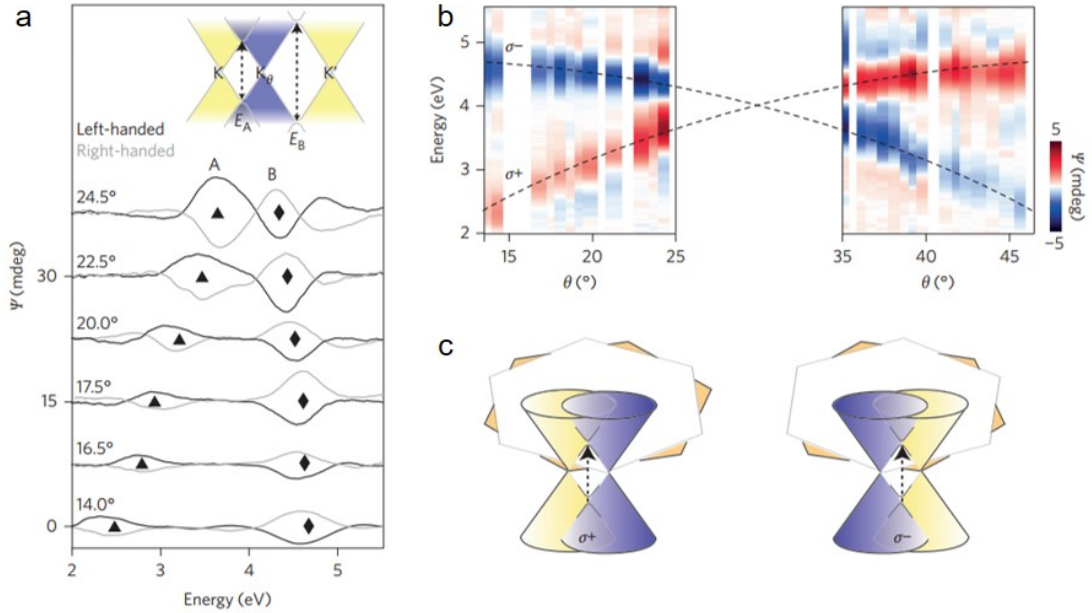


Figure 3.8: tBLG CD spectra  $\theta$  dependence

(a) CD spectra in chiral tBLG pairs with different  $\theta$ . Inset: Band structure of twisted bilayer graphene, where the  $K$  (or  $K'$ ) Dirac cone of the bottom layer (yellow) is hybridized with the  $K_\theta$  Dirac cone of the top layer (blue) producing the interlayer optical transition  $E_A$  (or  $E_B$ ). (b) Three-dimensional CD plot as a function of  $\theta$  (x axis) and energy of incident light (y axis), taken from 29 twisted bilayer graphene samples in total. All CD peaks are found along two lines, which indicate the energies of interlayer optical transitions. (c) For each interlayer optical transition, the top-layer Dirac cone (blue) can be rotated with respect to that of the bottom layer (yellow) either anticlockwise (left; corresponding to  $\sigma^+$ ) or clockwise (right;  $\sigma^-$ ), which determines the sign of the CD signal. This figure is adapted from Reference [94].

These phenomena can be explained as follows. As discussed in section 3.2, the lower energy vHS excitation  $E_A$  has the same chirality as the tBLG, while the higher energy vHS excitation  $E_B$  has the opposite chirality as the tBLG. Two peaks appear in the tBLG CD spectra: the lower energy peak corresponds to  $E_A$ , and the higher energy peak corresponds to  $E_B$ . Since  $E_A$  and  $E_B$  have different chirality, their CD spectra are opposite. Flipping the chirality of the tBLG sample will change the signs of the both peaks in the CD spectrum. In addition, with  $\theta$  changing, the position of  $E_A$  and  $E_B$  will change accordingly.

Besides the  $\theta$ -dependent optical properties, when the Fermi level reaches the vHS and mini-gaps,  $\theta$ -dependent electrical properties can also be detected in tBLG [49, 97]. However, limited by the doping capability,  $\theta$  shouldn't be too large in order to reach the vHS and mini-gaps. In Figure 3.9, we show a scanning tunneling microscope work done on tBLG. Our device level studies about tBLG will be presented chapter 4.

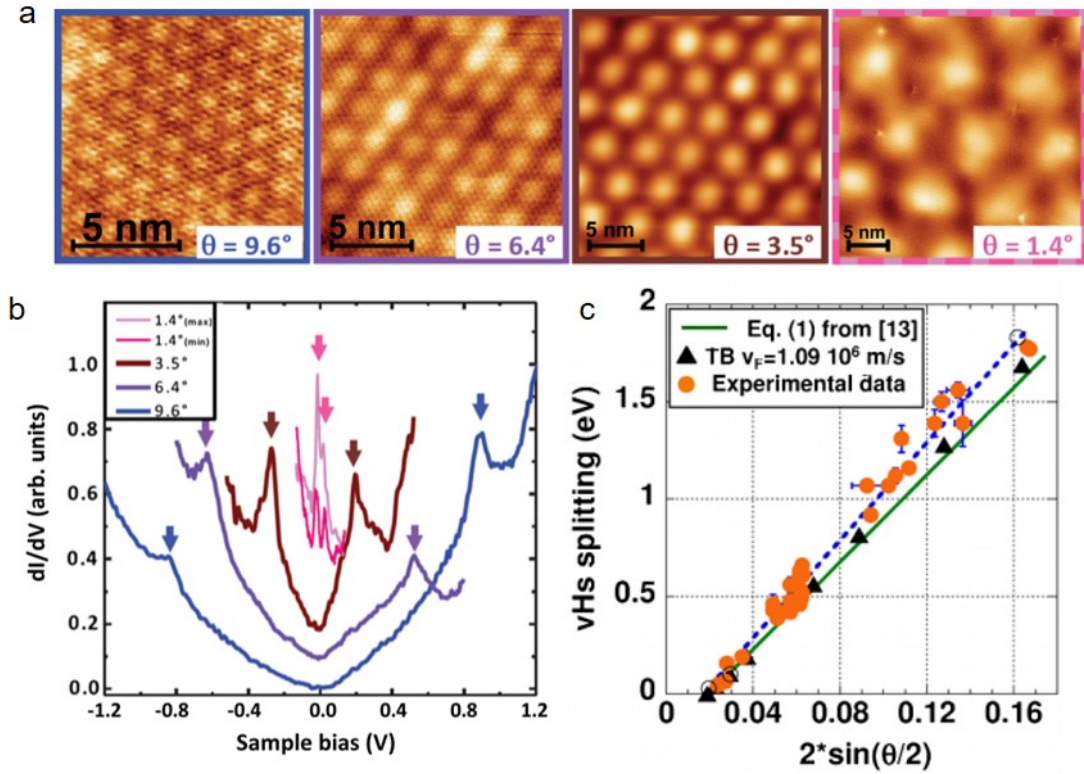


Figure 3.9: tBLG vHS direct mapping with STS

(a) The scanning tunneling microscopy images of several tBLG samples with different  $\theta$ . (b) The scanning tunneling spectroscopy measurements of different  $\theta$  tBLG. (c) The energies of vHS splitting from both experimental data and calculations are shown. TB stands for tight binding. This figure is adapted from Reference [49].

Figure 3.9 shows the scanning tunneling microscopy and spectroscopy (STM and STS) measurements of tBLG samples with different  $\theta$ . The twist angle of each sample is extracted from the moiré pattern measured by STM. The tunnel-

ing current derivative ( $dI/dV$ ) from the STS directly shows the density of states. The vHS states (indicated by the arrows) can be directly observed. With increasing  $\theta$ , the energy of the vHS also increases. Quantitatively, not surprisingly, the energies of the vHS states match very well with the tight binding calculation.

### **3.4 Assembly of tBLG by vacuum-assisted direct stacking**

#### **3.4.1 Introduction**

Among the tBLG works that were reviewed in the last section, the majority use as-grown samples from CVD growth. In these cases, as-grown sources can serve the purpose, because these studies only focus on understanding the properties of the tBLG system, so the trouble of sample-hunting could be borne with. However, if the goal is to apply these  $\theta$ -dependent properties, there would be requirements of sample size, sample yield, and time efficiency. Searching for tBLG areas with a certain  $\theta$  in a CVD sample is definitely not the best approach.

Moreover, even when time is not a concern, there are still limitations with synthetic sample sources. First, small- $\theta$  tBLG is very rare in as-grown CVD samples. We can see this clearly from the statistical data presented in Figure 3.10. Small- $\theta$  samples are rare, because the structure of small- $\theta$  tBLG is close to the energetically much more stable form, Bernal stacked BLG, which creates a large torque driving small twisted sample to become Bernal stacked during growth. Second, when synthetic sources are used, it is challenging to confirm the sample chirality, because the atomic thickness makes it hard to structurally resolve the handedness.

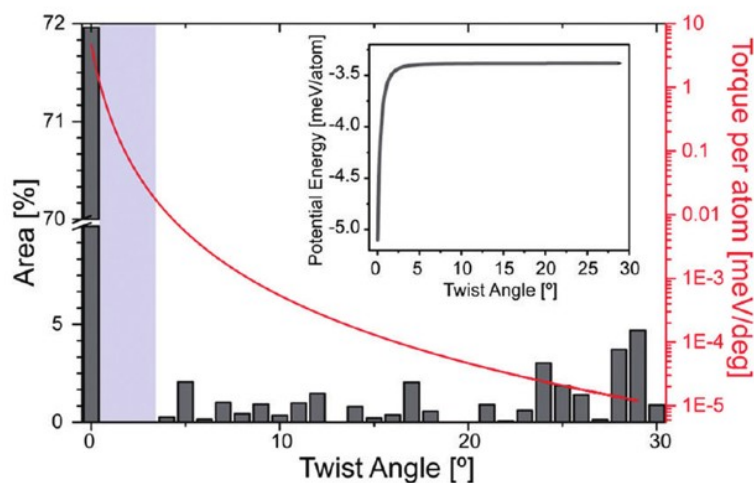


Figure 3.10: Statistical analysis of twist angle distribution in BLG. Area probability histogram of bilayer twist angles taken from 50 continuous bilayer regions with >100 individual bilayers. Overlaid in red is the torque calculated based on the theoretical plot of the interlayer potential as a function of the twist angle (inset, as adapted from Morell et al. [98]). This figure is adapted from Reference [99].

The solution to all these challenges is to develop an artificial stacking method that can generate large-scale high-quality tBLG with controllable  $\theta$ . Here, we report our vacuum-assisted direct stacking technique that can manually put two graphene layers obtained from aligned CVD growth on top of each other while controlling their mismatch angle. Comparing to other CVD graphene artificial stacking techniques, our method can avoid polymer contamination at the graphene-graphene interface and ensures high sample quality.

### 3.4.2 Graphene CVD growth and transfer

Our stacking technique can be divided into two parts: graphene growth and graphene stacking i.e. transfer. Before discussing the specific growth and trans-

fer methods that we use in our stacking process, let us first take a look at the graphene growth and transfer techniques in general.

CVD growth of graphene, as we briefly discussed in section 1.3, can be carried out on multiple substrates. Cu is the most widely used substrate because it yields single layer growth with high quality. Normally, the CVD growth of graphene on a Cu substrate involves two steps. The first step is annealing, where the Cu substrate is heated up to around 1000 °C under H<sub>2</sub> flow. The purpose of the annealing step is to reduce the CuO on the surface of the growth substrate back to Cu, the species which catalyzes graphene formation. The second step is growth, where a carbon source is introduced to the growth system to form graphene under the catalysis of Cu. Normally this step is also carried out at a high temperature (around 1000 °C). Methane is the most commonly used carbon source. Many other chemicals, however, such as ethane and propane can also be used [100]. If benzene is used as the carbon source, the temperature for graphene growth can be decreased down to around 300 °C [101]. Normally during the growth step, we also flow a certain amount of H<sub>2</sub>. H<sub>2</sub> serves multiple purposes: it removes the O<sub>2</sub> that get into the system, and affects the carbon source decomposition balance (changing growth speed), and etches graphene edge (affecting domain shape). During both the annealing and growth steps, inert gas (Ar or sometimes N<sub>2</sub>) may be introduced to the system as a way to control the growth pressure and help carry the precursor.

Now, let us look at graphene growth optimization. For CVD growth of graphene, there are many factors that can affect the growth, such as the growth substrate, gas flow rate, annealing temperature, annealing time, annealing pressure, growth temperature, growth time, growth pressure, oxygen leakage, and

also water vapor. Among these factors, the Cu substrate is one of the most critical factors for the growth. The surface impurity concentration, crystalline condition [102], and the shape (whether or not an enclosure is formed [103]) can dramatically change the resulting graphene growth. Interestingly, due to the strong interactions between graphene and its growth substrate, under specific growth conditions, there will be rotational orientation match between graphene and its growth substrate. This has been confirmed for graphene growth not only on Cu (111) substrates [104], but also ruthenium (0001) [105], iridium (111) [106], rhodium (111) [107], and germanium (110) [108] surfaces as well.

Once CVD growth is complete, we need to remove the growth substrate and transfer graphene to various new substrates in order to measure its intrinsic properties or make electronic devices out of it. For graphene grown on Cu, there is a standard transfer procedure. First, a film of polymer is spin coated on top of graphene. PMMA is the most commonly used polymer. Second, the graphene on the backside of the Cu substrate is removed by oxygen plasma. Third, wet etching is applied to etch away the copper. For the wet etching step, the PMMA/graphene/Cu stack is kept floating on the solution surface by the supporting force from surface tension. Two kinds of copper etchants are commonly used:  $\text{FeCl}_3$  mixed with HCl or ammonium persulfate ( $(\text{NH}_4)_2\text{S}_2\text{O}_8$ ) solution. Among these two,  $\text{FeCl}_3$  mixed with HCl etches Cu much quicker and does not generate bubbles during etching. However, when the pH of the solution is higher than around 4,  $\text{FeCl}_3$  can react with water and produce  $\text{Fe}(\text{OH})_3$ , which precipitates and sticks to the graphene surface. On the other hand,  $(\text{NH}_4)_2\text{S}_2\text{O}_8$  does not leave any solid residue, but its etching rate is much slower and it generates bubbles which can block further etching. The next step of the transfer procedure is a cleaning step. It is to get rid of various kinds of residues such

as Cu or the etching solution residue. Sometimes only multiple DI water rinses are necessary, but for better cleaning results, a diluted version of standard clean can be used. Standard clean is used in the silicon industry. It has two solutions: SC1, which is  $\text{NH}_4\text{OH}$  mixed with  $\text{H}_2\text{O}_2$  and  $\text{H}_2\text{O}$  by ratio of 1:1:5; and SC2, which is  $\text{HCl}$  mixed with  $\text{H}_2\text{O}_2$  and  $\text{H}_2\text{O}$  by ratio of 1:1:5. SC1 is for organic contamination cleaning and SC2 is for metal contamination cleaning. Diluted standard clean is made by changing both ratios to 1:1:20. For graphene, the majority of residue is metal. SC2 should be done first, followed by an optional SC1 step. In the last step, we need to use the target substrate to scoop up the PMMA/graphene stack that floats on top of DI water and wait for it to dry. Finally, the PMMA is removed by thermal annealing or by soaking in acetone followed by a IPA rinse.

For graphene transfer, lowering the amount of contaminants is critical for generating high quality films. There are two kinds of contaminations: inorganic and organic. Inorganic contaminations are mainly on the side which is in contact with the growth substrate, and we use chemical treatment such as SC2 to decrease it. However, chemical treatment can also break the chemical bonds within graphene and degrade the film quality, so proper choice of cleaning chemical and careful engineering of the process are required. Organic contamination comes from the supporting polymer that is on top of graphene. To better remove organic residues, we can use a heated acetone solution [94] instead of a room temperature one. However, the rule of thumb is, once the polymer touches graphene, it can never be completely removed.

Based on this discussion, we can see that with standard graphene transfer method, simply transferring one layer of graphene, getting rid of the PMMA,

and stacking another layer, cannot give us  $\theta$ -controlled high-quality tBLG.

### 3.4.3 Vacuum-assisted direct stacking

In our stacking method, in order to control the microscale structure parameter  $\theta$  in a macroscopic way, we adopted the procedure for aligned graphene growth on Cu (111) developed by Lola Brown et al. [109], with slight modifications. The key designs of this aligned growth are, first, increasing the time and temperature of the copper annealing step to recrystallize the Cu foil into Cu 111 domains; and second, decreasing the growth speed to ensure the growth following the thermodynamically stable path — the aligned growth. The growth recipe is as follows: (1) anneal the Cu foil (Nilaco corporation, #CU-113213) for 6 hours under 100 sccm H<sub>2</sub> and 400 sccm Ar at 1040 °C, (2) flow 3 sccm of 1% CH<sub>4</sub> which is diluted in H<sub>2</sub>, 100 sccm H<sub>2</sub>, and 400 sccm Ar at 1040 °C for 1 hour, (3) cut off the CH<sub>4</sub> flow, and cool the system down to room temperature while continuing to flow Ar and H<sub>2</sub>.

For stacking, as illustrated in Figure 3.11, we start with an aligned CVD graphene grown on a Cu substrate and cut it into two pieces. For one piece, we (1) spin PMMA on top to make a PMMA/graphene/Cu stack, (2) stick the PMMA side of this stack to a piece of thermal release tape that has hole punched in the middle, (3) send this entire stack through Cu etching, SC2 cleaning, several rinses with water, and finish with a gentle stream of air to dry out the graphene surface. The resulting product is PMMA/graphene supported by thermal release tape frame. For the other piece, we (1) cut it into a proper size, and (2) put it on top of a custom-made holder that has a center stage, a slightly

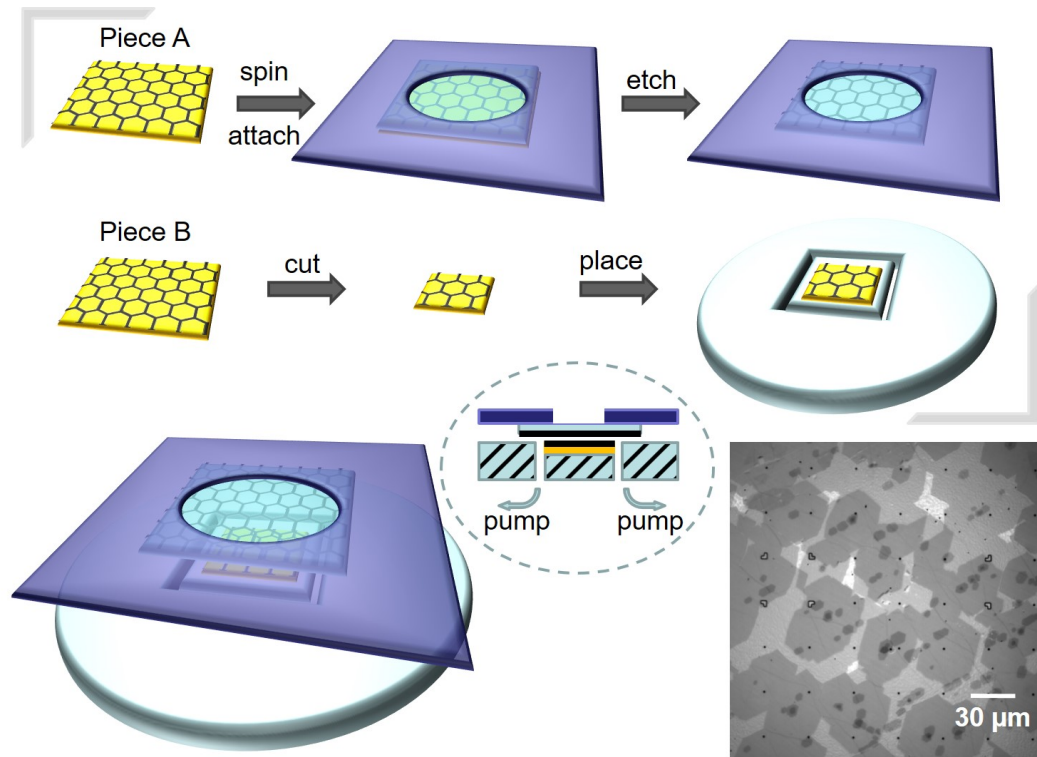


Figure 3.11: Schematics of vacuum-assisted direct stacking

higher outside stage, and a pumping groove in between. We then stack the first piece of graphene on top of the second piece, which stays on the holder, and apply a negative pressure between the first and the second graphene layers by pumping through the pumping groove. This negative pressure brings two layers together, while we perform a gentle heat gun treatment from the top to soften the PMMA to help improve the coupling. The microscopic  $\theta$  control is achieved by controlling the macroscopic rotation angle between the two Cu pieces, since the two pieces share the same graphene crystal to Cu film alignment. The resulting sample is on top of Cu and can then be transferred to a  $\text{SiO}_2/\text{Si}$  substrate for device fabrication, a SiN window for TEM measurements, or any other substrate. In bottom right of Figure 3.11, we show the optical microscope image of one stacked sample that is transferred to  $\text{SiO}_2/\text{Si}$  substrate.

Compared with other graphene stacking methods, our method achieves large-scale,  $\theta$ -controlled, and high-quality tBLG. In our method, the requirement for a large scale is met by using CVD as the sample source; the  $\theta$  control is achieved by using aligned CVD; and most importantly, the high quality is ensured by avoiding polymer exposure of the stacked interface throughout the stacking. In chapter 4, we will apply this vacuum-assisted direct stacking method to overcome the sample rarity problem of small- $\theta$  tBLG.

### 3.5 Summary

In this chapter, we reviewed tBLG. First, we discussed the electronic band structure of tBLG and introduced a single particle model for understanding the band structure. After that, we listed the  $\theta$ -dependent properties reported on tBLG, and also showed that the single particle model we introduced can quantitatively explain many of those phenomena. With these, we proved that twist angle  $\theta$  is a key parameter for tBLG, suggesting a need for an artificial stacking technique to generate high-quality tBLG with  $\theta$  control. Finally, after providing the general information about CVD graphene growth and graphene transfer, we introduced our vacuum-assisted direct stacking technique that generates  $\theta$ -controlled high-quality tBLG on a large scale.

## 4.1 Introduction

As discussed in chapter 3, in tBLG, interlayer interaction alters the band structure and creates new vHS and mini-gaps whose energy levels are monotonically tuned by the twist angle  $\theta$ . Among all tBLG, small- $\theta$  tBLG is special. In the single particle band structure picture of tBLG, two energy scales are involved: the energy level of the mini-gap that increases by approximately 100 meV per degree with  $\theta$ , and the magnitude of the mini-gap that is on the order of 200 meV [88]. When  $\theta$  is small, these two energy scales become close so that normally negligible small perturbations, i.e. the strain effect and many body interactions, need to be considered. Significant band dispersion changes are expected, which include Fermi velocity renormalization [87] and the formation of flat band [110]. As a result, insulating states [89], valley Hall boundary states [9, 10], and potentially superconducting states [110–113] may be observed in small- $\theta$  tBLG.

These predicted novel electronic properties inspire experimental explorations of small- $\theta$  tBLG. However, existing  $\theta$ -detection methods are not suitable for device level studies in the small  $\theta$  range. Non-optical techniques such as transmission electron microscopy (TEM) and scanning tunneling microscopy (STM), though accurate, are not device compatible [86, 99, 114]. Established optical methods, optical absorption [4, 7] and Raman G peak resonance [5, 6] measurements, though device compatible, do not suit small  $\theta$  detection. When  $\theta$  is small, the basis of these optical methods, the monotonic correlation between  $\theta$  and vHS excitation, pushes measurements beyond the visible range

to longer wavelengths, causing challenges in spatial resolution and signal detection. Also, this correlation, though valid for high angle, may be disrupted in small angle due to band renormalization, which may fundamentally invalidate these methods. The absence of a facile small angle detection method limits the fabrication, exploration, and application of small- $\theta$  tBLG.

This chapter is adapted from Reference [115]. In this chapter, we will report an optical  $\theta$ -detection method that has fundamental advantages over the existing techniques for small  $\theta$  detection. This method is based on the Raman  $R'$  process, an intralayer Raman scattering assisted by the interlayer moiré pattern [116]. The Raman  $R'$  process has  $\theta$ -dependent resonance at an energy level  $\sqrt{3}$  times as high as the vHS excitation (Figure 4.1a legend), which necessitates measurement at shorter wavelengths, thus yielding better spatial resolution and easier signal detection. In addition, its correlation with  $\theta$  would still hold even when the  $\theta$  dependence of vHS excitations were disrupted. By combining Raman with TEM measurements over a large number of samples, we quantitatively resolve the correlation between  $\theta$  and the peak intensity and peak position of the  $R'$  peak, explore the polarization properties of the  $R'$  peak, and then develop our  $\theta$ -detection method based on these results. With our method, the lower limit of optical  $\theta$  detection is pushed to  $3^\circ$ , an angle where  $\theta$ -dependent electronic features start to be detectable in a typical device. Furthermore, we utilize this method to demonstrate a dual-gate transistor device of small- $\theta$  tBLG, and report an extra resistance peak that arises from the mini-gap. The  $\theta$  extracted from this resistance peak is consistent with the Raman  $R'$  measurement.

## 4.2 $\theta$ dependence of Raman R' process

The mechanism of the Raman R' process is illustrated in Figure 4.1a [116]. In tBLG, interlayer interaction creates a quasi-periodic moiré pattern whose structure is determined by  $\theta$ . The static potential of this moiré pattern enables elastic scattering which permits access to non-zero momentum phonons in the longitudinal optical phonon branch. As a result, the intralayer intra-valley Raman R' scattering becomes allowed and the R' peak can be observed in tBLG Raman spectra in addition to the G and 2D peaks. Based on this mechanism, both the intensity and the position of the R' peak are expected to reveal dependences on  $\theta$  (detailed discussion later). These dependences, if quantitatively confirmed, can serve to realize  $\theta$  detection. While previous experimental results support these dependence predictions [5, 116–120], the available data from existing reports is not sufficient for achieving small angle detection, due to a limited number of samples and a relatively high lower-angle limit (the lowest being  $4^\circ$ ).

In this work, we present comprehensive angle-resolved R' data over a large number of samples, and push down the lower angle limit by fabricating small- $\theta$  samples and measuring them with lower frequency laser excitation. We include two key components in our experimental design. First, we adapt our vacuum-assisted direct-stacking technique to artificially generate small- $\theta$  tBLG. This solves the problem of sample rarity with small- $\theta$  tBLG and makes a large number of data points possible. Second, we combine TEM with Raman spectroscopy to enable angle-resolved Raman measurements. For this experiment, we transfer artificially stacked small- $\theta$  tBLG onto 10 nm thick SiN windows to make samples that are compatible with both Raman and TEM measurements. These samples are first excited by a 785 nm laser to obtain the Raman spectra,

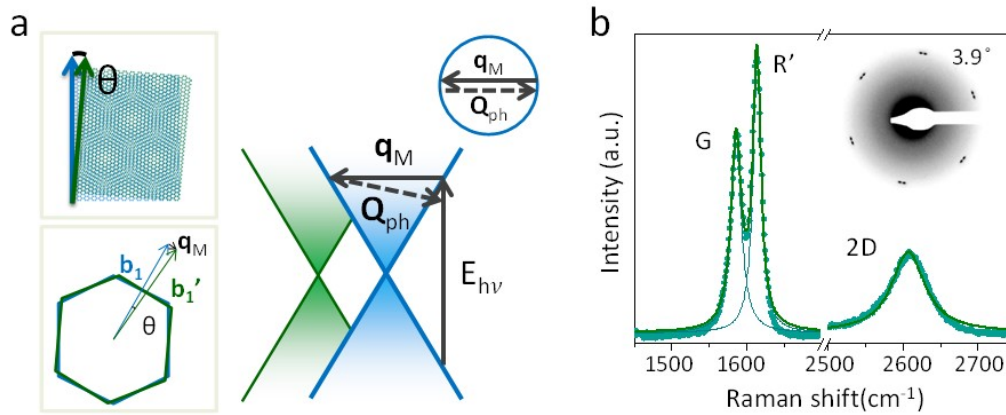


Figure 4.1: Schematics and representative spectrum of Raman R' process (a) Schematics for Raman R' process. (left top) Moiré pattern of tBLG. (left bottom) Small- $\theta$  tBLG in reciprocal space:  $\mathbf{b}_1$  and  $\mathbf{b}_1'$  are the reciprocal space primitive vectors of the top and bottom graphene layer;  $\mathbf{q}_M$  is moiré pattern reciprocal space primitive vector. (right) On-resonance Raman R' process: creation of electron-hole pair by laser excitation  $E_{hv}$ , electron scattering by moiré pattern (the same size as  $\mathbf{q}_M$ ) then back-scattering by non-zero momentum phonon  $Q_{ph}$ .  $\mathbf{b}_1$  and  $\mathbf{b}_1'$  are  $\sqrt{3}$  times as large as the momentum of the K point;  $\mathbf{q}_M$  is  $\sqrt{3}$  times the size of Dirac point shift between the two layers;  $E_{hv}$  is  $\sqrt{3}$  times the size of vHS excitation. (right inset) On-resonance Fermi circle: the momentum of  $\mathbf{q}_M$  is the same size as the Fermi circle diameter. (b) Representative Raman spectrum of one small- $\theta$  tBLG sample. (inset) The corresponding TEM diffraction pattern.

and then are put into TEM to take the diffraction patterns at exactly the same spots as the Raman measurement.

In Figure 4.1b, we present the Raman and TEM data from one representative sample. In the Raman spectrum, the R' peak appears right next to the G peak at around  $1614 \text{ cm}^{-1}$ ; it is well-defined and almost 50% higher than the G peak. The twist angle of this sample can be measured from its TEM diffraction pattern. There are two sets of six-fold-symmetric spots, each coming from one of the graphene layers. The angle offset between them gives the twist angle, which, for this sample, is  $3.9^\circ$ .

We take angle-resolved Raman spectra of 48 samples with  $\theta$  ranging between

3° and 10°. The experimental results are summarized in Figure 4.2. In Figure 4.2a, we plot spectra by color scale as a function of both  $\theta$  and Raman shift. From this plot, it is clear how G and R' peaks evolve with  $\theta$ : in the range of 3° ~ 6°, G peak remains relatively constant and the R' peak shows resonance behavior; in the range of 6° ~ 8°, G peak enhancement begins to dominate and the R' peak becomes difficult to resolve; and above 8°, the R' peak vanishes completely. For the purpose of small angle detection, we focus on the range from 3° to 6°, where both the intensity and position of the R' peak reveal dependences on  $\theta$ . In Figure 4.2b and 4.2c, quantitative experimental data points are plotted (black dashed lines serve as a guide for the eye). In Figure 4.2b, we normalize the intensity (area) of the R' peak relative to the G peak and plot it as a function of twist angle  $\theta$ . These data points show resonance behavior, as the intensity rises and falls with  $\theta$  increasing, reaching maximum value at  $\theta = 4.3^\circ$ . For peak position, as shown in Figure 4.2c, the R' peak increases monotonically with  $\theta$ ; the trend is almost linear, with a slope of about 2 cm<sup>-1</sup> per degree.

As mentioned earlier, the  $\theta$  dependence of the peak intensity and position arises due to the mechanism of the R' peak [116]. As illustrated in Figure 4.1a, the excited electron sits in a Fermi circle whose diameter is determined by the laser excitation energy  $E_{hv}$ . This electron is first elastically scattered by the moiré pattern and then inelastically scattered by longitudinal optical phonon  $Q_{ph}$ . The moiré pattern elastic scattering is similar to impurity site elastic scattering but with an extra restriction: its momentum must equal the moiré pattern's reciprocal space primitive vector  $\mathbf{q}_M$ , which equals the vector difference between the top and bottom graphene layer reciprocal space primitive vectors  $\mathbf{b}_1$  and  $\mathbf{b}_1'$ . Since the size of  $\mathbf{b}_1$  and  $\mathbf{b}_1'$  is set by the graphene lattice structure, the twist an-

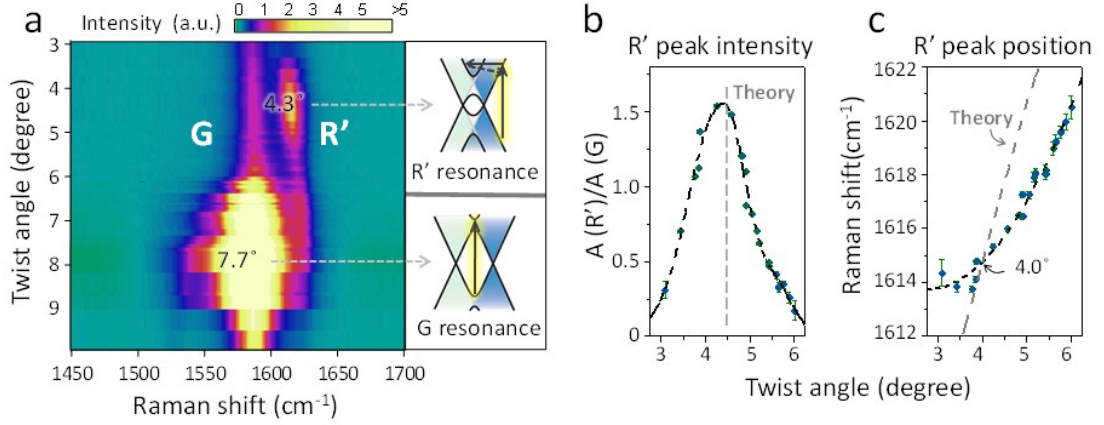


Figure 4.2: Quantitative study of small- $\theta$  tBLG Raman spectroscopy  
(a) 2D plot summarizing Raman spectra of tBLG samples ranging from  $3^\circ$  to  $10^\circ$  under 785 nm laser excitation. Intensity is plotted in a color scale as a function of the twist angle  $\theta$  and Raman shift in the range of  $1450 \text{ cm}^{-1}$  to  $1700 \text{ cm}^{-1}$ . On the right, schematics for both R' and G peak resonances are provided. (b), (c), Quantitative analysis of Raman R' peak. (b) R' peak area normalized to G peak is plotted as a function of  $\theta$ . Experimental data is plotted in blue dots; the black dashed line is a guide for the eye; and the grey dashed line indicates the theoretical resonance peak position. (c) R' peak position is plotted as a function of  $\theta$ . Experimental data is plotted as blue dots; the black dashed line is a guide for the eye; and the grey line is the theoretical prediction of R' peak position. Experimental data and theoretical prediction cross at  $4.0^\circ$ .

gle  $\theta$  determines the size of  $\mathbf{q}_M$ :

$$|\mathbf{q}_M| = \frac{8\pi}{\sqrt{3}a} \sin \frac{\theta}{2} \quad (4.1)$$

Here,  $a = 2.46 \text{ \AA}$  is the lattice constant of graphene. The R' resonance occurs when  $\mathbf{q}_M$  and the Fermi circle diameter (determined by laser excitation  $E_{hv}$ ) are the same size. Considering the linear band structure of graphene, the resonance condition is:

$$E_{hv} = \hbar v_f \frac{8\pi}{\sqrt{3}a} \sin \frac{\theta}{2} \quad (4.2)$$

Here,  $v_f$  is the Fermi velocity and  $\hbar$  is the reduced Planck constant. According to this theoretical model, the resonance  $\theta$  is  $4.5^\circ$  ( $v_f = 1.03 \times 10^6 \text{ m/s}$ ) for the 785 nm laser (grey dashed line in Figure 4.2b), which agrees well with the  $4.3^\circ$  from

our experiment.

The on-resonance  $R'$  peak position is determined by the energy of  $Q_{\text{ph}}$ , which can be extracted from graphene's phonon band structure [121] if the phonon momentum is known. [116] Because of momentum conservation, the momentum of the phonon  $Q_{\text{ph}}$  is approximately the same as that of the elastic scattering vector  $\mathbf{q}_M$ . For a given twist angle  $\theta$ ,  $\mathbf{q}_M$  is known, and since the momentum of  $Q_{\text{ph}}$  equals  $\mathbf{q}_M$ , the  $R'$  peak position can therefore be calculated accordingly. In Figure 4.2c, the predicted  $R'$  peak position from this model is plotted (grey dashed line) together with the experimental data. They follow similar trends but their values do not match exactly. The angle at which the values match is  $4.0^\circ$ , close to the resonance angle. This discrepancy between the theory and our experiment probably arises because the model assumes a resonance condition while the experiment is off resonance except at  $\theta \approx 4.3^\circ$ . When off resonance, the constraint that elastic scattering momentum equals  $\mathbf{q}_M$  is not strict, which causes the peak position to differ from the prediction that assumes resonance. A more detailed model is needed to quantitatively explain the off-resonance case, which is beyond the scope of this dissertation.

### 4.3 $R'$ process polarization property

We also discover that there is a polarization effect in the  $R'$  process, which needs to be considered when using the  $R'$  peak intensity for the  $\theta$  measurement. As shown in Figure 4.3a, when excited by a linearly polarized laser, the  $R'$  peak intensity changes when the relative angle ( $\alpha$ ) between the laser and the signal analyzer changes, while the G peak remains constant. If we vary  $\alpha$  from  $0^\circ$  to

360° and plot the normalized R' peak intensity relative to  $\alpha$  in a polar plot, as shown in Figure 4.3b, it is clear that the R' peak reaches maximum when the analyzer and the laser polarization are parallel, and minimum when they are perpendicular. The scattered light remembers the polarization direction of the incoming light and has higher intensity along the same direction. Interestingly, this polarization behavior also depends on  $\theta$ : the sample measured in Figure 4.3 is near resonance, and has a parallel to perpendicular ratio of 4.2; when  $\theta$  is further from resonance, as for the sample in Figure 4.4, we observe a lower parallel to perpendicular ratio (around 2.5).

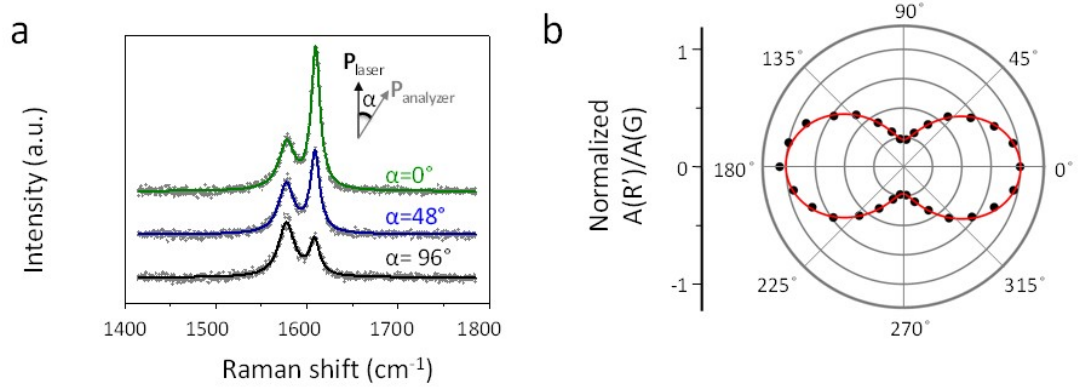


Figure 4.3: On resonance R' peak polarization dependence (a) Raman spectrum for the same small- $\theta$  tBLG sample under different polarization settings: angle ( $\alpha$ ) between detector analyzer and laser polarization direction is 0°, 48°, and 96°. (b) Summary of normalized R' to G peak area ratio as a function of  $\alpha$  in polar coordinates. Red line:  $0.62 + 0.38 \cos(2\alpha)$ , the trigonometric fitting result.

This polarization behavior can be understood by considering the inhomogeneous light excitation and emission mediated by the scattering steps. During electron-hole creation or recombination, under the dipole approximation, the absorption or emission matrix element is proportional to  $\pm(\mathbf{P}_{\text{light}} \times \hat{k})$ , where  $\mathbf{P}_{\text{light}}$  is light polarization vector and  $\hat{k}$  is electron (hole) momentum measured from the K (K') point. [122] This implies that polarized light selectively excites

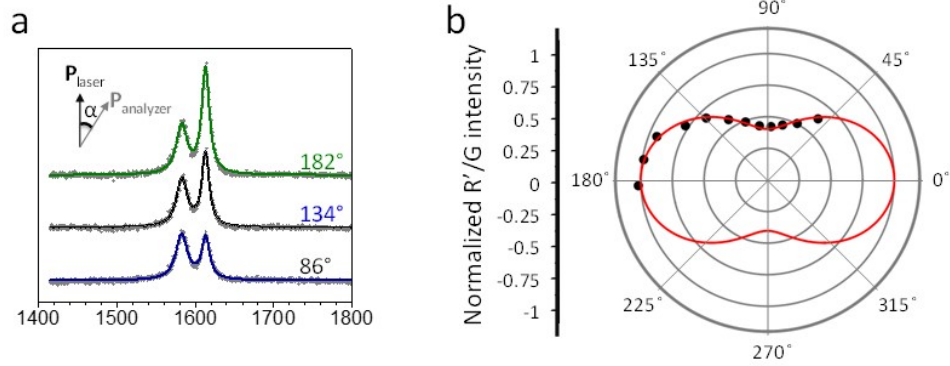


Figure 4.4: Off resonance R' peak polarization dependence (a) Raman spectrum for the same small- $\theta$  tBLG sample under different polarization settings: angle ( $\alpha$ ) between detector analyzer and laser polarization direction is 86°, 134°, and 182°. (b) Summary of normalized R' to G peak area ratio as a function of  $\alpha$  in polar coordinates. Red line:  $0.7 + 0.3 \cos(2\alpha)$ , the trigonometric fitting result.

states with specific momentum (perpendicular to  $\mathbf{P}_{\text{light}}$  is preferred), and states with specific momentum also selectively emit polarized light (perpendicular to  $\hat{k}$  is preferred). As a result, during the scattering steps, if the selectively excited electron-hole pairs do not get redistributed evenly along the Fermi circle, then the emitted light will be polarized. In the R' process, scattering happens across the diameter of the Fermi circle along three directions determined by  $\mathbf{q}_M$  [116]. The initial electron-hole pair's momentum direction is changed by 0° or 180°, depending on whether just the electron or the hole gets scattered, or if both are scattered. In either case, the exciton is not redistributed evenly along the Fermi circle, and the emitted light would be polarized. Similar to the peak position case, when off resonance, the constraint on scattering direction is not strict, thus a lower parallel to perpendicular ratio is expected.

In Figure 4.5, we provide a more quantitative explanation for the polarization behavior. The method we use here is modified from the heuristic model reported by Duhee Yoon and co-workers [122]. In Figure 4.5, the long dashed line

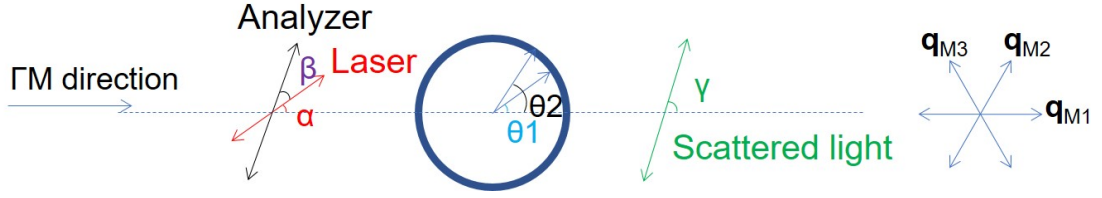


Figure 4.5: Derivation of the polarization dependence

The dotted line indicates the direction of  $\Gamma M$ . The incident (scattered) light has a polarization which is rotated by  $\alpha$  ( $\gamma$ ) relative to  $\Gamma M$  direction. The analyzer is rotated by  $\beta$  relative to the laser polarization.  $\mathbf{q}_{M1}$ ,  $\mathbf{q}_{M2}$  and  $\mathbf{q}_{M3}$  are the directions of the moiré pattern's reciprocal space primitive vectors

goes along the  $\Gamma M$  direction. Relative to the  $\Gamma M$  direction, the incident laser has a polarization along  $(\cos \alpha, \sin \alpha, 0)$  direction, the scattered light has a polarization along  $(\cos \gamma, \sin \gamma, 0)$  direction. Here  $\theta_1$  ( $\theta_2$ ) is the angle difference between the  $\Gamma M$  direction and the momentum of the excited electron measured from K or K' point. The absorption matrix can be expressed as  $\sin(\alpha - \theta_1)$  and the emission matrix can be expressed as  $\sin(\gamma - \theta_2)$ . On resonance, scattering happens across the Fermi circle diameter along three directions only: they are defined by the moiré pattern's reciprocal space primitive vectors ( $\mathbf{q}_{M1}$ ,  $\mathbf{q}_{M2}$ ,  $\mathbf{q}_{M3}$ ). Because of the rotation symmetry of both the electronic states around the Fermi circle and phonon states near  $\Gamma$  point, we assume the electron-phonon matrix elements along all three  $\mathbf{q}_M$  directions to be the same. As a result, the scattering intensity at  $\gamma$  will be proportional to:

$$I(\alpha, \gamma) = \left| \sum_{\theta_1, \theta_2} \sin(\alpha - \theta_1) \times \sin(\gamma - \theta_2) \right|^2 = 9 \cos^2(\alpha - \gamma) \quad (4.3)$$

Here, the sum is taken over  $\theta_1$  and  $\theta_2$  at 6 directions decided by the three  $\mathbf{q}_M$  (both forward and backward).

Then the scattered light is projected to the analyzer along the direction  $(\cos(\alpha$

$+\beta), \sin(\alpha + \beta), 0)$ . The resulting intensity will be:

$$\int_0^{2\pi} I(\alpha, \gamma) \cos^2(\alpha + \beta - \gamma) d\gamma = \frac{9}{4}\pi (1 + 2\cos^2\beta) \quad (4.4)$$

From this result, we can get that the maximum intensity will be measured when  $\beta$  equals 0 or  $\pi$ , which is the case when laser and analyzer are parallel to each other, and that the minimum intensity will be measured when  $\beta$  equals  $\pi/2$  or  $3\pi/2$ , which is the case when laser and analyzer are perpendicular to each other. The parallel to perpendicular ratio is 3 to 1.

The R' peak intensity reveals polarization dependence; on the contrary, the G peak is known to be unpolarized. As a result, the intensity of R' peak relative to G peak varies by the polarization setting, with a maximum difference reaching 4 times (Figure 4.3b). Considering polarization is important for  $\theta$ -detection. For instance, the data in Figure 4.1 and 4.2 is taken under a linearly polarized laser without an analyzer. If an analyzer is inserted at the detector side and aligned to the excitation laser, the R' peak intensity would need a correction. This result can be found in Figure 4.6.

#### 4.4 $\theta$ mapping through R' process

In section 4.2 and 4.3, we provide quantitative data for the R' peak under a 785 nm laser. Referring to our data, one can directly measure small  $\theta$  through the following steps: (1) use a 785 nm linearly polarized laser to take the Raman spectrum of the target sample, (2) extract the R' peak intensity and peak position, (3) compare the R' peak intensity and peak position result to our data to extract the angle. If the peak intensity is on resonance,  $\theta$  equals the resonance

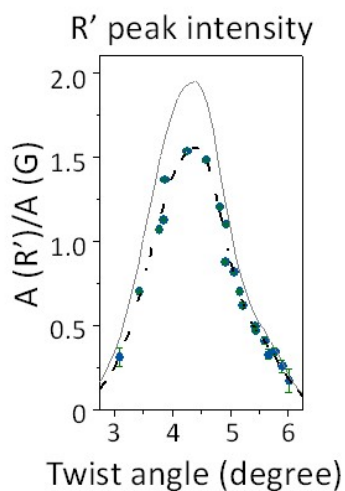


Figure 4.6: Polarization correction of R' peak intensity

R' peak area normalized to G peak is plotted as a function of  $\theta$  under linear polarized laser. The black dotted line is a guide for the eye and the gray line is the expected peak intensity when polarizer is inserted at the detector side with its fast axis aligned with the excitation laser

angle; if the peak intensity is off resonance, extract two possible angles based on the peak intensity, then pick out the correct one based on the peak position.

The same procedure can be developed for other laser wavelengths. Currently, with a 785nm laser, the lower limit for  $\theta$  detection is  $3^\circ$ . We expect a lower threshold for detection if longer wavelength light sources and detectors are used. Moreover, if laser illumination is changed from a focused point to a line and the spectra from all the points along this line are collected by a CCD camera simultaneously, quick mapping of  $\theta$  over a large sample area can also be achieved [123]. In the actual experiment, we add a cylindrical lens to the beam pass to change the laser excitation spot into line form and use CCD to simultaneously collect spectra from all the points along this line. These spectra were collected repeatedly with the sample being moved perpendicular to the laser excitation line to map the entire sample area. Figure 4.7 shows an example of  $\theta$

mapping. In Figure 4.7a, the optical picture of the tBLG is provided. In Figure 4.7b, the twist angle extracted from the R' peak measurement is plotted. We can tell there is an angle difference moving across a wrinkle.

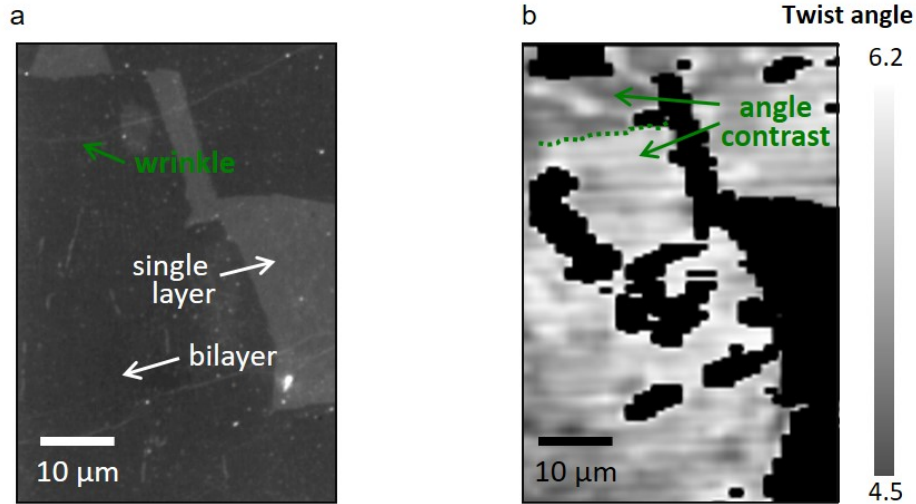


Figure 4.7: Angle mapping with Raman R' peak  
 (a) Optical image. (b)  $\theta$  mapping. Notice that angle contrast can sometimes be observed across wrinkle.

However, for the mapping method, attention needs to be paid when applying the peak position dependency. As presented earlier, peak position shift with  $\theta$  is about  $2 \text{ cm}^{-1}$  per degree; such a small shift means applying this dependency requires a well-calibrated Raman setup and the absence of other factors affecting the peak position. For example, heating is a major concern. With temperature increase, the graphene Raman peaks in general show a red shift. We use G peak as an example since its position is  $\theta$  independent and should be constant if no heating effect exists. In Figure 4.8, the G peak position through line scanning is mapped out: in the SiN window center, it is red-shifted by  $10 \text{ cm}^{-1}$  compare to the edge, resulting from higher temperature in center region due to poorer thermal cooling.

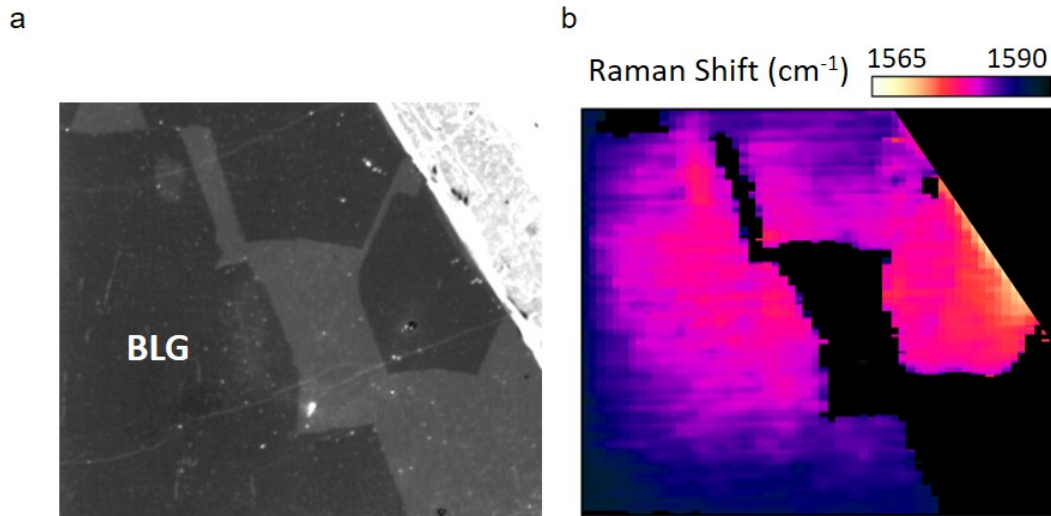


Figure 4.8: Effects of heating on Raman G peak  
 (a) Optical image for a sample on 10 nm SiN window. (b) G peak position measured from line scanning is plotted in a color scale (only bilayer region). The center region is red-shifted compare to the edge region.

Because of this heating effect, we recommend to always check both the R' intensity and position during  $\theta$  measurement and adjust the measurement condition accordingly. As a demonstration, for the angle measurements presented in Figure 4.7, in order to maintain the laser power in each spot along the line, the total input power could not be kept low, and the heating effect became unavoidable. During the actual measurement, line scanning is first done to divide the sample into several domains based on the R' peak intensity; then in each domain, point measurement is processed to determine whether the angle belongs to the  $3^\circ \sim 4.3^\circ$  branch or the  $4.3^\circ \sim 6^\circ$  branch according to its R' peak position. The final result is extracted by combining R' peak intensity data from line mapping and branch assignment from point measurements.

## 4.5 $\theta$ -dependent electronic features in small- $\theta$ tBLG

With this Raman-based angle detection method, we demonstrate a dual-gate small- $\theta$  tBLG transistor device, as shown in Figure 4.9. To build our device, we transfer as-grown CVD graphene onto a SiO<sub>2</sub> (62 nm)/Si substrate, on which one BLG domain is confirmed to be small angle through the emergence of a R' peak and its angle is measured to be 3.1° (Figure 4a). On this small- $\theta$  tBLG region, we fabricate a dual-gate multi-channel Hall bar device using electron beam lithography. In four steps, we (1) define Ni/Au electrodes, (2) pattern the graphene, (3) grow Al seeded Al<sub>2</sub>O<sub>3</sub> by ALD as top gate oxide, and (4) define a top gate. An optical image of this multi-channel device before depositing the top gate is provided in Figure 4.9a inset.

This small- $\theta$  tBLG device shows a clear electronic feature resulting from interlayer interactions. The square resistance of this device is measured at 77 K under a dual-gate sweep, which gives independent control over doping ( $Q$ ) and vertical displacement field ( $D$ ). In the measurement, two resistance peaks along constant  $Q$  lines (gray dotted line and dashed line) stand out. To better illustrate, in Figure 4.9c, we provide a line cut plot crossing these two peaks along the  $D \approx 0$  line (white dashed line in Figure 4b). As doping increases (top x-axis), the first resistance peak appears at  $Q = 0$  and the second appears at  $Q = 2.3 \times 10^{13} \text{ cm}^{-2}$ . The peak at  $Q = 2.3 \times 10^{13} \text{ cm}^{-2}$  originates from the Fermi level reaching the mini-gap. (We rule out the explanation of inhomogeneous local doping, since we observe similar electrical behavior in all three channels.) We extract the twist angle  $\theta$  by matching this experimentally measured mini-gap doping level with electronic band structure and get  $\theta = 2.8^\circ$ , which agrees well with the  $3.1^\circ$  obtained from the Raman measurement.

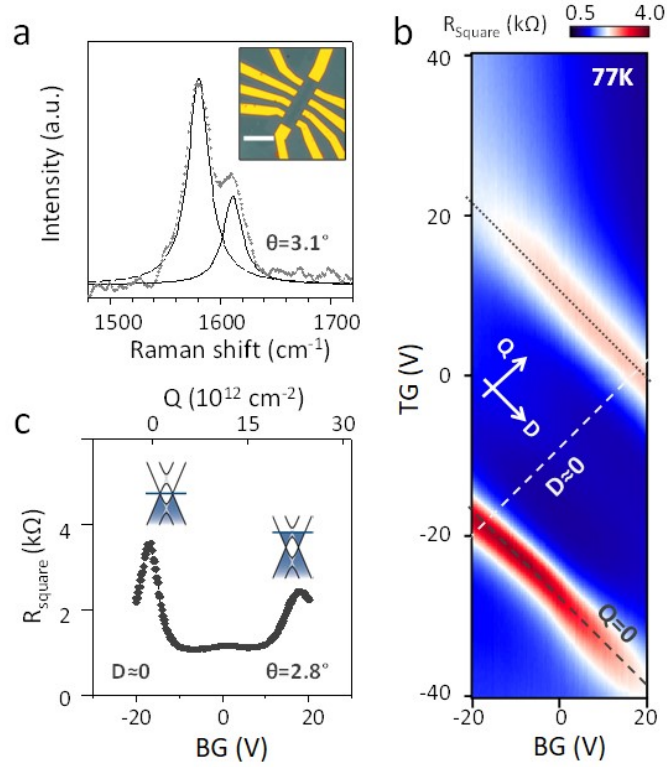


Figure 4.9: Electrical conductivity study of dual gate small- $\theta$  tBLG device (a) Raman spectrum for the device region.  $\theta$  extracted from Raman spectrum is  $3.1^\circ$ . Inset: optical image of the device after graphene patterning. Scale bar is  $10 \mu\text{m}$ . (b) tBLG square resistance plotted in color scale as a function of top and back gate voltages. Dotted and dashed lines are: constant vertical field line  $D \approx 0$  (white dashed), constant doping line  $Q = 0$  (gray dashed), and constant doping line  $Q = \text{mini gap}$  (gray dotted). (c) Square resistance versus back gate voltage (bottom x-axis) and doping (top x-axis) along the constant vertical field line  $D \approx 0$ . The doping schematics for both resistance peaks are provided.

The details for twist angle calculation are as follows. Referring to a tBLG tight binding calculation reported by Pilkyung Moon and Mikito Koshino [124] (Figure 4.10), we extract, for the  $3.89^\circ$  tBLG, a 2:1 ratio between the vHS doping level and the mini-gap doping level. Assuming that our sample has the same vHS to mini-gap doping ratio as  $3.89^\circ$  tBLG, we calculate the vHS doping level of our sample. After that, we apply the single particle model and calculate the

twist angle using the following equation:

$$Q_{vHS} = \frac{2}{\pi}(k_K)^2 \sin^2 \frac{\theta}{2} \quad (4.5)$$

Here,  $k_K$  is the momentum of the K point.

We choose this calculation strategy because: first, single particle model has been proven to predict experimental data with quantitative accuracy by previous STS and optical studies of tBLG [7, 49]; second, unlike tight binding model which only works for commensurate angles, single particle model provides a continuous correlation between vHS doping level and the twist angle.

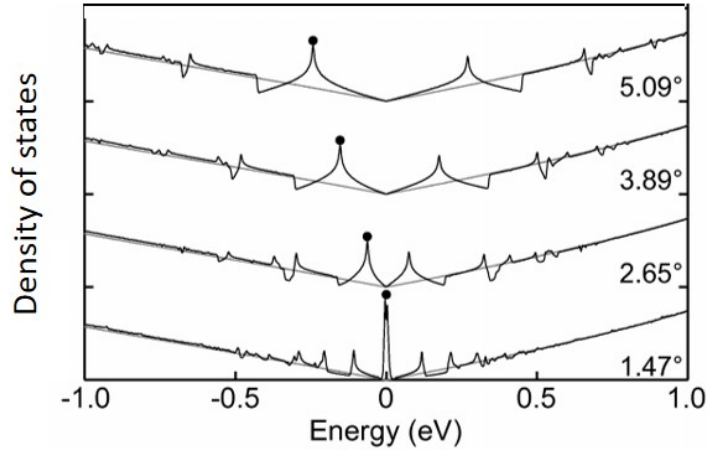


Figure 4.10: Density of states of tBLG based on tight binding calculation. This figure is adapted from Reference [124].

## 4.6 Other electronic features in small- $\theta$ tBLG

In section 4.5, we discussed the effect of twist angle on the electronic properties of small- $\theta$  tBLG. In this section, we will focus on other features of the data

plotted in Figure 4.9b, mainly the effects of the vertical displacement field on small- $\theta$  tBLG electrical conductivity.

To isolate the effect of the vertical field, we first extract the square resistance along constant doping lines  $Q = 0$  and  $Q = 2.3 \times 10^{13} \text{ cm}^{-2}$ . Along the constant doping lines, the combination effects of the top and back gates results in the changing of the vertical displacement field, following this equation:

$$D = \frac{1}{2} \left( \frac{\epsilon_{TG} V_{TG}}{d_{TG}} - \frac{\epsilon_{BG} V_{BG}}{d_{BG}} \right) \quad (4.6)$$

Here,  $\epsilon$  and  $d$  are the dielectric constant and thickness of the gate dielectric layer respectively, and  $V$  is the applied gate voltage. We plot the calculated vertical displacement in the top axis in Figure 4.11a and 4.11b. Looking at the result, we can see that the resistance of tBLG around both the Dirac point and the mini-gap decreases with increasing vertical field.

To explain this observation, we need to consider the two kinds of effects that the vertical field has on small- $\theta$  tBLG: the intralayer effect and the interlayer effect. For the intralayer effect, vertical field shifts the chemical potential of the top and bottom layer Dirac cones; as a result, the doping of each layer changes, though total doping level  $Q$  ( $Q_t + Q_b$ ) stays constant. This gives rise to a change in the total carrier density ( $|Q_t| + |Q_b|$ ) and can cause the electrical conductivity to change if assuming the two layers are relatively independent of each other. For the interlayer effect, it is caused by the vertical field altering the band structure of small- $\theta$  tBLG (e.g. the size of mini-gap opening). This can affect the electrical conductivity as well. To check whether or not the interlayer effect is responsible for the experimental data, we can assume two non-interacting single layers to calculate the carrier density at different vertical fields and then plot the conductance as a function of carrier density. If the conductance vs. carrier density trend

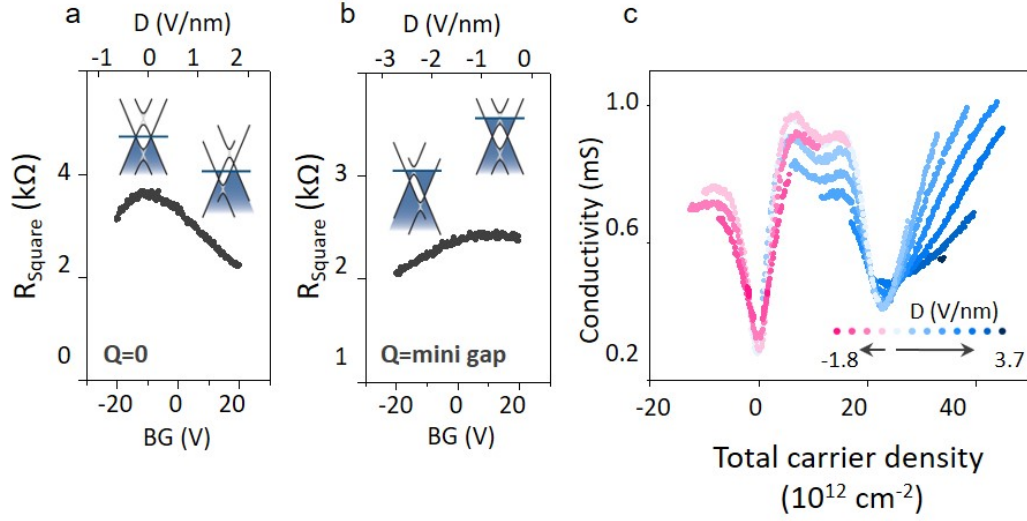


Figure 4.11: Effects of doping and vertical field on small- $\theta$  tBLG

(a) Square resistance along constant charge line  $Q = 0$  relative to vertical field (top axis). (b) Square resistance along constant charge  $Q = \text{mini gap}$  relative to vertical field (top axis). Insets are schematics for band structure with the Fermi level under different  $D$  and  $Q$  conditions. (c) The conductivity plotted as a function of total carrier density under different vertical field (sign is assigned according to the sign of total doping).

is the same under different vertical fields, it means that the intralayer effect is dominating; otherwise, the interlayer effect also plays a role.

To calculate the total carrier density ( $|Q_t| + |Q_b|$ ), we combine the Gauss's law with the requirement of potential balance. [125] According to Gauss's law, we have:

$$Q_t + Q_b = C_{TG} (V_{TG} - \mu_t) + C_{BG} (V_{BG} - \mu_b) \quad (4.7)$$

Here,  $C$  is the capacitance,  $\mu$  is the chemical potential,  $V$  is the applied gate voltage. According to the requirement of potential balance, we have:

$$\mu_t - \mu_b = E_{gg} \cdot d_{gg} \quad (4.8)$$

where  $E_{gg}$  is the residual electric field in between two graphene layers and  $d_{gg}$  is the distance between the two layers. For the chemical potential of graphene,

according to graphene band distribution we have:

$$\mu = \text{sign}(Q) \frac{\hbar v_f \sqrt{\pi |Q/e|}}{e} \quad (4.9)$$

Here,  $\hbar$  is the reduced plank constant,  $e$  is the charge of electron (the value is positive). The sign is defined such that when graphene is electron-doped,  $Q$  and  $\mu$  have a positive sign. For  $E_{gg}$ , the residual electric field between the two graphene layers, the electric field introduced by the top and back gate is partially screened by the two layers. The result is this equation:

$$E_{gg} = \frac{1}{\epsilon_{gg}} \left( \frac{C_{TG}(V_{TG} - \mu_t) - C_{BG}(V_{BG} - \mu_b)}{2} + \frac{Q_t - Q_b}{2} \right) \quad (4.10)$$

Here,  $\epsilon_{gg}$  is the dielectric constant between the two graphene layers. In equation (4.7) and (4.8), substituting  $E_{gg}$  and  $\mu$  with equations (4.9) and (4.10), we end up with two equations and two unknown values  $Q_t$  and  $Q_b$  (all other values are either constants, the device geometry values, or applied gate voltages). We adapt the value of  $\epsilon_{gg}$  from reference [125]. To correct for the charge introduced by charge impurities,  $V_{0TG}$  and  $V_{0BG}$ , the top and back gate voltages cooresponding to the zero charge and zero vertical field point, are extracted out in our calculation.

In Figure 4.11c, we plot the conductance vs. carrier density under different vertical fields. It can be seen that around  $Q = 0$ , the correlations are approximately the same for different vertical fields, suggesting that the intralayer effect is dominating. Around  $Q = 2.3 \times 10^{13} \text{ cm}^{-2}$ , the correlation varies for different vertical fields, and there is a combination of both intralayer (carrier density change) and interlayer (band structure change) effects. We can conclude that, around  $Q = 0$ , the vertical field affects electrical property at the intralayer level. It causes two layers' Dirac cones to shift. The top and bottom graphene layers

are doped with the same amount, but different sign of charge (total carrier density  $(|Q_t| + |Q_b|)$  increases), leading to a total resistance decrease. Moving away from the Dirac point, the vertical field starts to show the interlayer effect. For example, at the second resistance peak corresponding to the mini-gap, the vertical field shifts the chemical potential of the top and bottom layer Dirac cones, and weakens the interlayer interactions due to the increased differences between the two mixing orbitals. This results in the decreasing resistance just as observed. Away from the mini-gap, the major trend is that the vertical field increases the resistance. More detailed calculation is needed to explain this, which is beyond the scope of this dissertation.

#### 4.7 Large- $\theta$ tBLG and Bernal BLG electronic features

To complete the discussion, in this section, we will talk about electronic properties of large- $\theta$  tBLG and Bernal BLG. We already know that for large- $\theta$  tBLG, the vHS states occur at a high energy level, and within the Fermi level accessible doping range, its band structure resembles that of two independent single layers. We can predict that for the electrical conductivity of large- $\theta$  tBLG, similar to the low doping range of small- $\theta$  tBLG, the graphene layers should act as two independent single layers carrying the electrical current in parallel. The experimental results are plotted in Figure 4.12a, which are in agreement with our predictions. In Figure 4.12c, we present the same data analysis that we did in Figure 4.11c, and plot conductivity relative to the total carrier density. According to the result, we can conclude that for large- $\theta$  tBLG, the total conductivity is approximately proportional to the total carrier density. The small deviation between different vertical fields could be caused by the increasing hysteresis when

the vertical field is large.

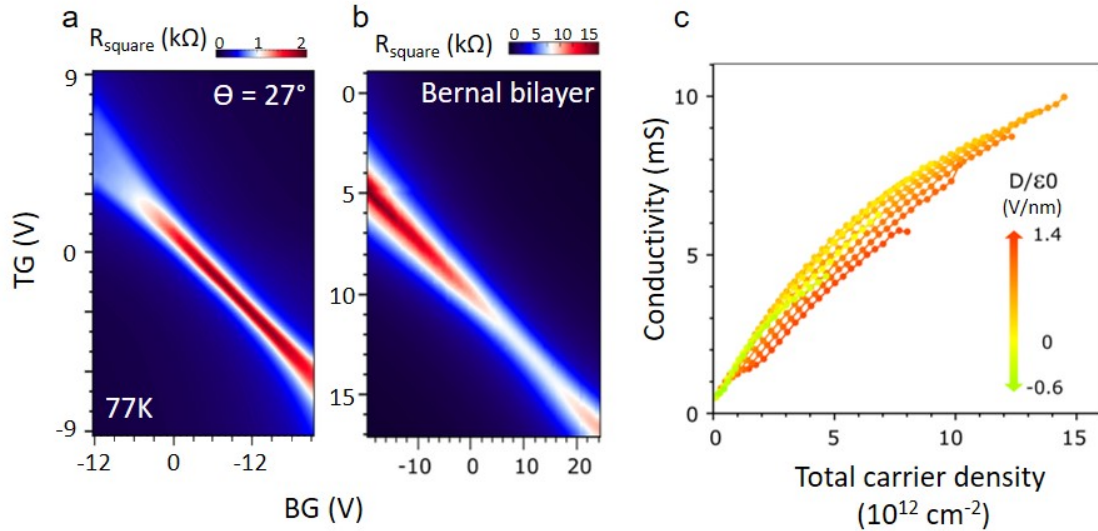


Figure 4.12: Effects of doping and vertical field on small- $\theta$  tBLG

(a)  $27^\circ$  tBLG square resistance plotted in color scale as a function of top and back gate voltages. (b) Bernal BLG square resistance plotted in color scale as a function of top and back gate voltages. (c) For  $27^\circ$  tBLG, the conductivity plotted as a function of total carrier density under different vertical field (only positive total doping is plotted).

In comparison, as plotted in Figure 4.12b, we can see that the response of Bernal BLG to the vertical field is quite different from that of tBLG. For Bernal BLG, the vertical field opens a band gap, and as a result, the resistance increases with increasing vertical field.

## 4.8 Summary

In conclusion, we introduce a Raman-based characterization method that directly maps  $\theta$  in small- $\theta$  tBLG samples based on our quantitative study of the R' Raman band and report the electrical conductivity of a small- $\theta$  tBLG transistor with a dual-gate, which shows a doping dependent conductance drop when

the Fermi level is close to the mini-gaps. Our experiment is a comprehensive electrical and optical characterization of angle-resolved small- $\theta$  tBLG. It can be further generalized for exploring novel electronic devices of small- $\theta$  tBLG. Furthermore, for a complete description of the tBLG system, we provide information about the electrical conductivity properties of large- $\theta$  tBLG and Bernal BLG relative to the vertical field and doping. Combined with existing reports about angle measurement of large- $\theta$  tBLG and optical detection of Bernal BLG, we now have a complete picture of the BLG system.

## CHAPTER 5

### STACKED TMD AS FUNCTIONAL DIELECTRIC LAYER

#### 5.1 Introduction

In chapters 3 and 4, we talked about tBLG, a stacked system where interlayer interactions alter the system's properties. However, as we discussed in chapter 1, the fact that the van der Waals interlayer interaction in stacked 2D materials is weaker than typical strong interactions such as chemical bonds, means that it does not necessarily introduce property changes to the system. Stacked 2D material films may behave just as a combination of its 2D building blocks. But even when stacking-induced property changes are absent, these kinds of stacked 2D material systems can still be of great use. They can form functional films with layer thickness control down to atomic scale, and are free from property-degrading due to interface impurity, since they have chemically well-defined interfaces. Graphene sandwiched by hBN is a good example of one such functional film, which reveals high graphene mobility due to the charge-impurity-free interface [15].

This chapter focuses on our preliminary research work on building functional films out of a stacked 2D material system. The stacked 2D system with which we work here is made up of one graphene layer and multiple  $WS_2$  layers stacked together. The idea is to use  $WS_2$  instead of hBN in the graphene/hBN stack. The motivation is to achieve a large-scale high-quality functional dielectric film out of stacked 2D materials.  $WS_2$  is chosen because its high quality large scale growth is available using the MOCVD method introduced in chapter 2. In comparison, hBN cannot be grown at this scale. The downside of  $WS_2$

(band gap 1.9 eV) is that it is a semiconductor instead of an insulator such as hBN.

As we discuss below, we proved that stacked multilayer  $\text{WS}_2$  can serve as a functional dielectric layer by fabricating a graphene FET using the graphene/ $\text{WS}_2$  stacked 2D materials system and demonstrating that this FET can function properly. Although the FET performance is not as good as the graphene/hBN stacked system, the fact that stacked semiconducting  $\text{WS}_2$  film can form a functional dielectric layer opens many potential applications, for example, using this film as the encapsulating dielectric layer for channel materials that are sensitive to air or charge impurities, or applying this film in places where achieving precise dielectric thickness is critical, such as a tunneling device.

## 5.2 Stacking and device fabrication

To build this graphene/ $\text{WS}_2$  stack, we mainly apply the vacuum stacking method for TMD films reported by Kibum Kang, Kanheng Lee, et al [126]. According to their report, it is easy to detach high quality TMD films grown by the MOCVD method from the growth substrate by mechanical peeling. Under vacuum, the peeled TMD layer can be put onto another TMD film that sits on its growth substrate. The resulted stacked TMD layers can subsequently be peeled from the substrate together. By repeating the peeling and stacking steps, multilayer TMDs with clean interfaces can be built.

When building our multilayer  $\text{WS}_2$  stack, detailed operations are as follows. First, we spin PMMA on top of the first  $\text{WS}_2$  film that sits on the  $\text{SiO}_2/\text{Si}$  sub-

strate and bake the PMMA film by placing the substrate on a hotplate at 180 °C for 5 mins. In the PMMA spin coating process, the PMMA used is formulated with 495,000 molecular weight and is dissolved in anisole with a concentration of 4%. Using a spinning speed of 3000 rpm, we get a PMMA film thickness of around 2  $\mu\text{m}$ . Here, the relatively large molecular weight of PMMA ensures the interaction between PMMA and the  $\text{WS}_2$  is stronger than the interaction between  $\text{WS}_2$  and the substrate, while not leaving too much residue after being removed with acetone. The thinness of the PMMA guarantees the film flexibility. In the second step, we attach a piece of thermal release tape (TRT) to the PMMA/ $\text{WS}_2$ / $\text{SiO}_2$ /Si stack, and use the thermal release tape to peel off the TRT/PMMA/ $\text{WS}_2$  stack from the  $\text{SiO}_2$ /Si substrate. Third, at 150 °C and vacuum conditions, using a custom-made stacking chamber, we stack the peeled-off TRT/PMMA/ $\text{WS}_2$  film onto another  $\text{WS}_2$  on  $\text{SiO}_2$ /Si substrate. In this step, the vacuum condition removes air bubbles during stacking, which, combined with the relaxation of the PMMA film at 150 °C, guarantees that the two  $\text{WS}_2$  films come in contact with each other. Forth, under ambient conditions, we heat the TRT/PMMA/ $\text{WS}_2$ / $\text{WS}_2$ / $\text{SiO}_2$ /Si stack at the releasing temperature of the thermal release tape (120 °C), and anneal the PMMA/ $\text{WS}_2$ / $\text{WS}_2$ / $\text{SiO}_2$ /Si stack at 180 °C for 5 mins to further relax the PMMA film to ensure  $\text{WS}_2$  to  $\text{WS}_2$  attachment. Finally, by repeating steps two through four, we can build multilayer  $\text{WS}_2$  with controllable layer number.

After building multilayer  $\text{WS}_2$ , the next part is to add graphene into this stack. The actual operation procedure depends on the graphene source. If exfoliated graphene is used, we can apply exactly the same method as  $\text{WS}_2$  stacking, and use multilayer  $\text{WS}_2$  to pick up the exfoliated graphene that sits on top of a  $\text{SiO}_2$ /Si substrate. If CVD graphene is used, we can follow step 3 of  $\text{WS}_2$

stacking, but change the target  $WS_2/SiO_2/Si$  substrate into graphene/Cu. In this way, we put down multilayer  $WS_2$  with PMMA on top of a graphene/Cu substrate. Then we etch away graphene on the other side of Cu using oxygen plasma etching. After that, we attach a thermal release tape to the PMMA side and remove the copper substrate using wet etching. Once that is done, we have a TRT/PMMA/multilayer  $WS_2$ /graphene stack, which can be used to further pick up other films or can be put down on a target substrate for device fabrication.

For devices reported in this chapter, exfoliated graphene is used. We stack 8 layers of  $WS_2$  on top of exfoliated graphene (schematics shown in Figure 5.1a) and turn the structure into a dual-gate two-terminal transistor devices. The optical image of device is plotted in Figure 5.1b. The device fabrication was done using electron beam lithography. Before putting down the 8-layer  $WS_2$  film, a targeted flake of SLG is picked out using optical methods and its position is recorded. Then, we put down the 8-layer  $WS_2$  film and fabricate the graphene transistor device with edge contacts in three steps. We (1) pattern the stacked  $WS_2$  and graphene to define the graphene transistor channel, (2) put down Cr/Au edge contacts, (3) define a Ti/Au top gate.

We use exfoliated graphene to rule out the effect of graphene quality on the final device performance and better evaluate how well a stacked semiconducting  $WS_2$  film can serve as a dielectric layer.

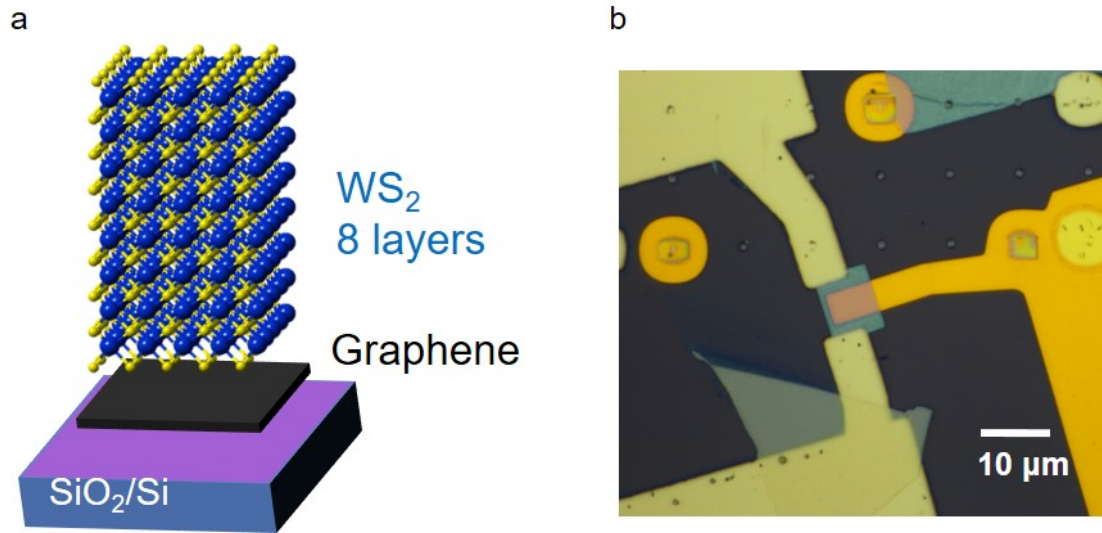


Figure 5.1: Graphene transistor with stacked  $\text{WS}_2$  as dielectric layer  
 (a) Schematic for the graphene/ $\text{WS}_2$  stack used for graphene transistor device.  
 (b) Optical image of the graphene transistor device with stacked  $\text{WS}_2$  as gate dielectric material.

### 5.3 Dielectric properties of the stacked TMD film

To evaluate performance of the 8-layer  $\text{WS}_2$  film as a dielectric layer, we first look at the leakage current. As plotted in Figure 5.2a, we measure the current between the source and top gate. When low gate bias is applied (lower than 30 mV), the current increases linearly with the applied bias, and the area-normalized resistance is  $0.6 \text{ G}\Omega\cdot\mu\text{m}^2$ . When the gate bias is high, at around 0.5 V, the tunneling effect becomes dominating. One feature of the tunneling curve is the asymmetry: tunneling current is much higher with positive bias. This asymmetry occurs because the tunneling happens between gold and graphene across 8 layers of  $\text{WS}_2$ , which is an asymmetric system. At 0.8 V gate bias, the system has a normalized resistance of  $10 \text{ M}\Omega\cdot\mu\text{m}^2$ . According to these results, under low gate bias, the stacked  $\text{WS}_2$  would serve the purpose of a dielectric layer quite well. Even under high bias, gate resistance is still orders of mag-

nitude higher than the graphene channel, and the measured channel current should still be dominated by the current through the channel material instead of the gate leakage current.

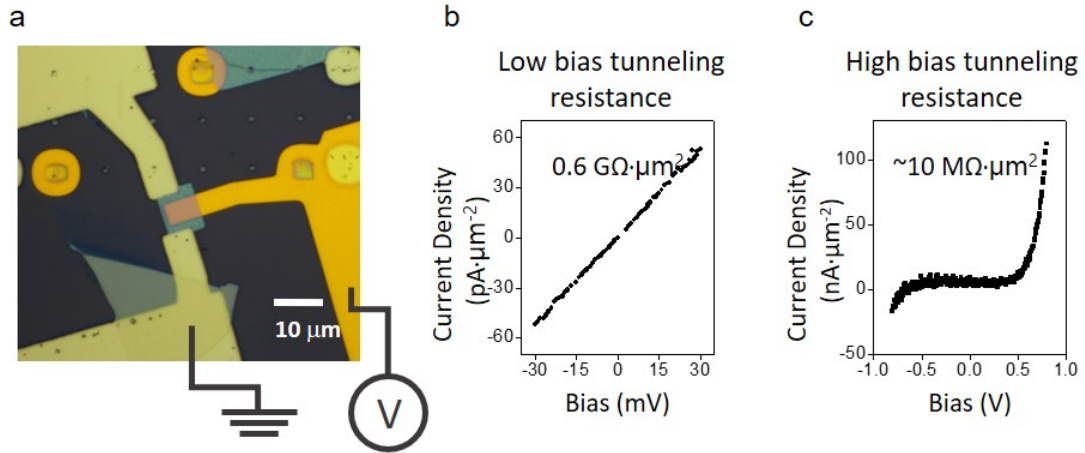


Figure 5.2: Graphene transistor gate leakage (a) Measurement setting for leakage current detection. (b) Leakage current as a function of gate bias at a low bias voltage range. (c) Leakage current as function of gate bias at a high bias voltage range.

In Figure 5.3, we measure the graphene transistor performance. Two terminal channel conductivity is measured while tuning the top gate voltage. After extracting the gate tunneling current away from the channel current for more accurate measurement, we plot the square conductivity of graphene as a function of top gate voltage in Figure 5.3b. It can be seen that using 8 layers of WS<sub>2</sub> as gate dielectric, we can observe Dirac point of the graphene, proving that our WS<sub>2</sub> film can serve the purpose of dielectric film.

To extract the dielectric constant of our stacked WS<sub>2</sub> layer, we perform a dual-gate measurement with both the WS<sub>2</sub> top gate and the SiO<sub>2</sub> back gate. As plotted in Figure 5.4, we measure the channel resistance, while fixing the back gate at different values and sweeping the top gate. In each sweeping curve, there is one Dirac point, at which the combination of top and back gate yields

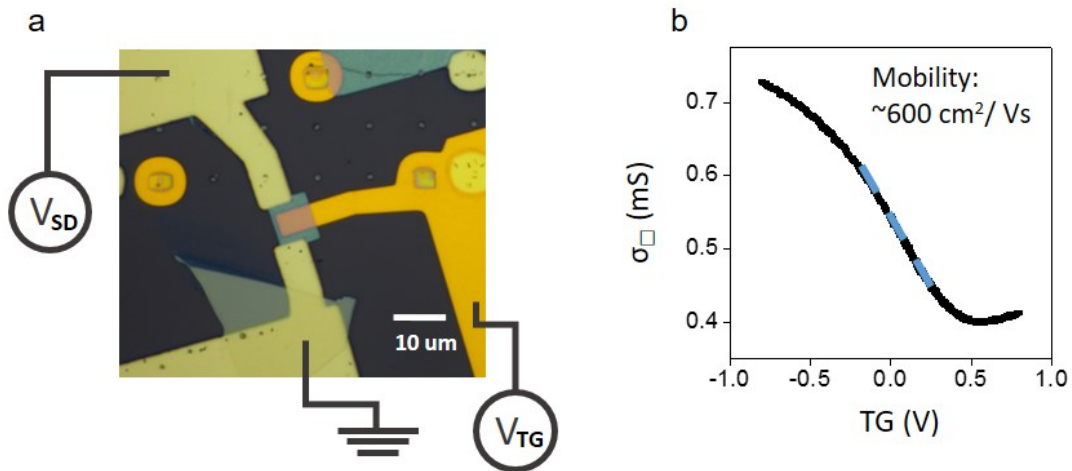


Figure 5.3: Graphene transistor channel performance  
 (a) Measurement setting for graphene transistor conductivity while tuning top gate. (b) Graphene square conductivity as a function of top gate.

a total doping of zero. We extract the positions of those Dirac points and plot out the back gate voltage positions as a function of top gate voltage positions. All the Dirac points fall onto one line, and from the slope of this line, we measure the ratio between the top and back gate capacitance. Knowing both the capacitance and the dielectric layer thickness, the dielectric constant of  $WS_2$  can be calculated. The stacked  $WS_2$  dielectric constant extracted from this measurement is 3.6.

Knowing the dielectric constant of the stacked  $WS_2$  film, we can now extract the mobility of the graphene with stacked  $WS_2$  as the gate dielectric layer. As plotted in Figure 5.3b, the mobility of our graphene channel is around  $600 \text{ cm}^2 \cdot \text{V}^{-1} \cdot \text{s}^{-1}$ , which is quite low. The reasons could be (1) the bottom gate is  $SiO_2$ , which has dangling bonds on the surface and can decrease device performance, (2) the device is two-terminal, so the measured channel mobility is lower than the real channel mobility, and the (3) top gate does not fully cover the channel area, which also makes the measured mobility lower than the real mobility.

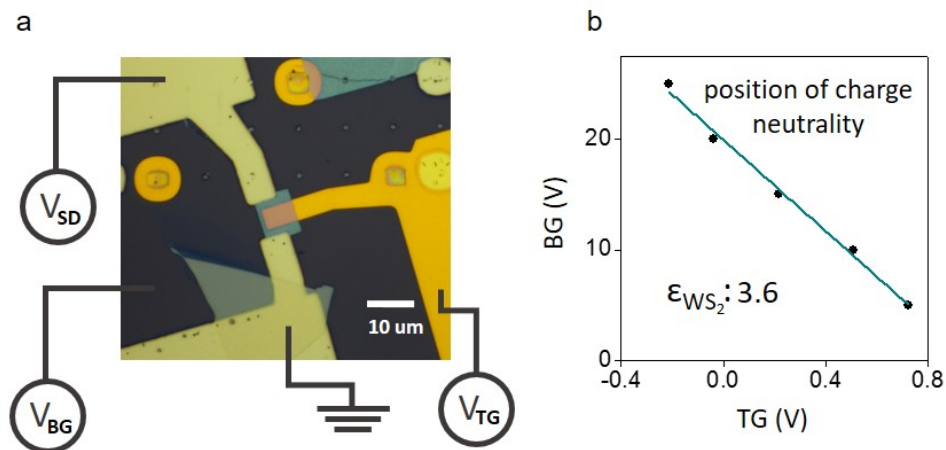


Figure 5.4: Extracting dielectric constant of stacked  $WS_2$   
 (a) Measurement setting for graphene transistor conductivity while tuning both top and back gate. (b) Back gate voltage of graphene Dirac point as function of top gate.

## 5.4 Summary

We fabricated a graphene transistor device with 8-layer  $WS_2$  as the dielectric layer and proved that a stacked semiconducting  $WS_2$  film can serve the purpose of a functional dielectric film. Although the data here are preliminary and we did not observe improved device performance by using stacked 2D films, it is a demonstration that stacked 2D materials systems, even when their film properties are not altered by interlayer interactions, can still form functional films in electronic devices.

## CHAPTER 6

### FUTURE DIRECTIONS

In this dissertation, the major achievements are (1) large-scale high-quality TMD growth using the MOCVD method, (2) the vacuum-assisted artificial stacking method for CVD graphene, which yields large-scale tBLG with low levels of interlayer contamination, (3) the optical angle detection method for small- $\theta$  tBLG using the R' process, and (4) the demonstration that stacked semiconductor WS<sub>2</sub> films can form a functional dielectric layer. Based on these results, we propose several future directions.

#### 6.1 TMD growth on patterned substrate

One future direction is to grow TMDs on patterned substrates. This patterning of the TMD growth substrates can happen on 2D or 3D level. On 2D level, although the growth of TMDs does not depend on specific precursor-substrate chemistry, the surface bonding condition still affects the growth of TMDs. It is possible to achieve patterned growth through substrate functionalization or modification. For example, as reported by Marcos Guimaraes and Hui Gao, on the graphene surface, due to the lack of dangling bond, the growth of MoS<sub>2</sub> and WS<sub>2</sub> is suppressed [127]. Inspired by this result, we propose using one kind of TMD film to modify the growth substrate for other TMDs. As plotted in Figure 6.1, we start by growing WSe<sub>2</sub> on top of SiO<sub>2</sub>/Si substrate. Then, we pattern the WSe<sub>2</sub> film, and carry out MoS<sub>2</sub> growth on the patterned substrate. Here, WSe<sub>2</sub> can be treated as an insulating material within the working doping range for MoS<sub>2</sub> devices, because the WSe<sub>2</sub> is a p-type semiconductor and requires a high level of doping to be turned on. This 2D patterned TMD growth can be

combined with other 2D material patterned growth [128] and the 2D stacking technique to build 3D atomically thin circuitry.

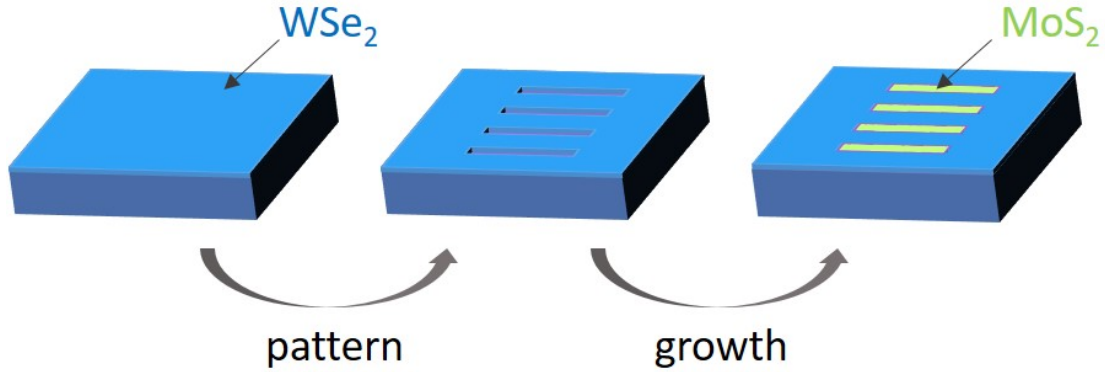


Figure 6.1: Patterned MoS<sub>2</sub> growth

However, using 2D materials for growth substrate modification can be a complicated process. Ideally, we prefer approaches that can be directly combined with standard photolithography techniques. Plasma treatment is one candidate. We expect SiO<sub>2</sub> substrate, when treated by oxygen plasma, to have higher growth speed due to increased number of or activated surface dangling bond. Other plasma processes are also worth testing. Besides plasma treatment, another candidate is to modify the substrate with certain surface modification chemicals. For example, we propose testing hexamethyldisilazane (HMDS) and trimethylsilyl chloride (TMSCl), which are widely used for enhancing the hydrophobicity of SiO<sub>2</sub> through the silylation process. One piece of supporting data we have is that the silylated substrate has been found to be stable up to 650 °C [129], higher than the MoS<sub>2</sub> growth temperature which is 550 °C.

On the 3D level, since TMD growth follows the same morphology as the growth substrate, we can get TMD films with desired 3D shapes simply by engineering the substrate. This can help us get TMD films with special mechanical or optical properties and enables the fabrication of circuitry with 3D shapes.

## 6.2 Explore angle generated features in small- $\theta$ tBLG

In small- $\theta$  tBLG, it would be very interesting to keep pushing down the twist angle and explore new features that arise. Expected band dispersion changes include Fermi velocity renormalization and the formation of a flat band. Expected structural change is the formation of strain soliton, and expected new properties includes insulating states, valley Hall boundary states, and potentially superconducting states. Here, we will discuss a few proposals.

First, using our vacuum-assisted stacking technique, we can fabricate a series of small- $\theta$  tBLG samples and use TEM to find out the angle at which strain soliton begins to form. On samples with that angle, we can explore whether or not the Raman R' process still exists.

Second, there are reports which claim the observation of signs of superconductivity in HOPG, indicating tBLG with small  $\theta$  might reveal superconducting properties with high critical temperature [111–113]. However, according to existing reports on small- $\theta$  tBLG superconducting behavior is not observed [97]. This is still worth more investigation. To explore this direction, we need to make series of high-quality small- $\theta$  tBLG samples and fabricate devices out of them. Because of the quality requirement, CVD graphene is not a good sample source. We propose following the method reported by reference [97] to build tBLG with artificial stacking of exfoliated graphene. However, instead of a single tBLG sample, we propose attempting to build multilayer stacks that have altering big  $\theta$ , small  $\theta$ , or Bernal multilayer to Bernal multilayer small  $\theta$  twists to resemble the stacking conditions in HOPG, which would also make the process much easier.

### 6.3 Free-standing stacked 2D material circuitry

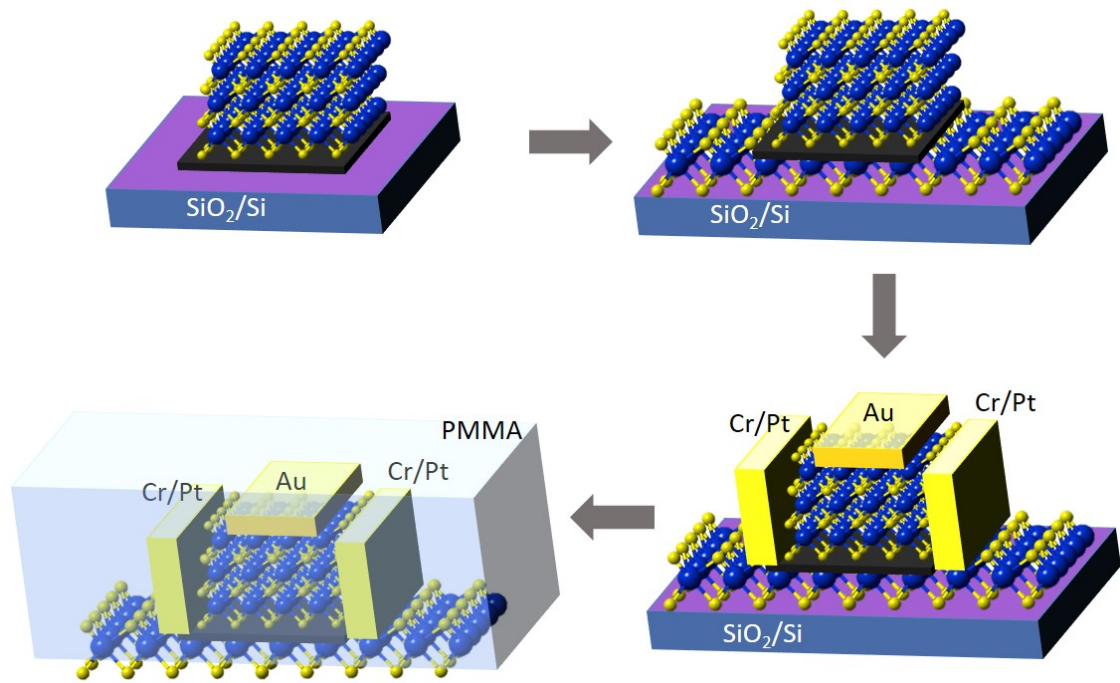


Figure 6.2: Fabrication of free-standing stacked 2D material circuitry  
The number of  $WS_2$  layers is just for demonstration purposes. Real device should be thick (we propose more than 7 layers).

In chapter 5, the graphene transistor devices with stacked  $WS_2$  as the top gate does not reveal superior mobility when compared with a graphene transistor on a  $SiO_2$  substrate. We suspect the existence of the  $SiO_2$  back gate as the main reason. Based on this analysis, we propose fabricating a free-standing graphene transistor with stacked  $WS_2$  as the top gate. The experimental design is shown in Figure 6.2. First, build the multilayer  $WS_2$  stack and stack it on top of exfoliated SLG. Second, after patterning the graphene/ $WS_2$  stacking into the desired channel shape, pick up this stacked film and put it on top of  $SiO_2/Si$  substrate fully covered with  $WS_2$  film. Third, fabricate the transistor device by putting down edge contacts and top gate. Finally, spin PMMA on top and peel the entire device away from the substrate. We can measure the graphene tran-

sistor device before and after the final step and check if the device performance improves.

## BIBLIOGRAPHY

- [1] A. K. Geim and I. V. Grigorieva, "Van der Waals heterostructures," *Nature*, vol. 499, no. 7459, pp. 419–425, jul 2013.
- [2] K. S. Novoselov, A. Mishchenko, A. Carvalho, and A. H. Castro Neto, "2D materials and van der Waals heterostructures," *Science*, vol. 353, no. 6298, jul 2016.
- [3] Z. Ni, L. Liu, Y. Wang, Z. Zheng, L.-J. Li, T. Yu, and Z. Shen, "G-band Raman double resonance in twisted bilayer graphene: Evidence of band splitting and folding," *Physical Review B*, vol. 80, no. 12, p. 125404, sep 2009.
- [4] Y. Wang, Z. Ni, L. Liu, Y. Liu, C. Cong, T. Yu, X. Wang, D. Shen, and Z. Shen, "Stacking-Dependent Optical Conductivity of Bilayer Graphene," *ACS Nano*, vol. 4, no. 7, pp. 4074–4080, jul 2010.
- [5] K. Kim, S. Coh, L. Z. Tan, W. Regan, J. M. Yuk, E. Chatterjee, M. F. Crommie, M. L. Cohen, S. G. Louie, and A. Zettl, "Raman Spectroscopy Study of Rotated Double-Layer Graphene: Misorientation-Angle Dependence of Electronic Structure," *Physical Review Letters*, vol. 108, no. 24, p. 246103, jun 2012.
- [6] R. W. Havener, H. Zhuang, L. Brown, R. G. Hennig, and J. Park, "Angle-Resolved Raman Imaging of Interlayer Rotations and Interactions in Twisted Bilayer Graphene," *Nano Letters*, vol. 12, no. 6, pp. 3162–3167, may 2012.
- [7] R. W. Havener, Y. Liang, L. Brown, L. Yang, and J. Park, "Van Hove Singularities and Excitonic Effects in the Optical Conductivity of Twisted Bilayer Graphene," *Nano Letters*, vol. 14, no. 6, pp. 3353–3357, jun 2014.
- [8] B. Hunt, J. D. Sanchez-Yamagishi, A. F. Young, M. Yankowitz, B. J. LeRoy, K. Watanabe, T. Taniguchi, P. Moon, M. Koshino, P. Jarillo-Herrero, and R. C. Ashoori, "Massive Dirac Fermions and Hofstadter Butterfly in a van der Waals Heterostructure," *Science*, vol. 340, no. 6139, pp. 1427 LP – 1430, jun 2013.
- [9] J. S. Alden, A. W. Tsen, P. Y. Huang, R. Hovden, L. Brown, J. Park, D. A. Muller, and P. L. McEuen, "Strain solitons and topological defects in bilayer graphene," *Proceedings of the National Academy of Sciences*, vol. 110, no. 28, pp. 11 256–11 260, jul 2013.

- [10] L. Ju, Z. Shi, N. Nair, Y. Lv, C. Jin, J. Velasco Jr, C. Ojeda-Aristizabal, H. A. Bechtel, M. C. Martin, A. Zettl, J. Analytis, and F. Wang, "Topological valley transport at bilayer graphene domain walls," *Nature*, vol. 520, no. 7549, pp. 650–655, apr 2015.
- [11] L. Jiang, Z. Shi, B. Zeng, S. Wang, J.-H. Kang, T. Joshi, C. Jin, L. Ju, J. Kim, T. Lyu, Y.-R. Shen, M. Crommie, H.-J. Gao, and F. Wang, "Soliton-dependent plasmon reflection at bilayer graphene domain walls," *Nat Mater*, vol. 15, no. 8, pp. 840–844, aug 2016.
- [12] A. Avsar, J. Y. Tan, T. Taychatanapat, J. Balakrishnan, G. K. W. Koon, Y. Yeo, J. Lahiri, A. Carvalho, A. S. Rodin, E. C. T. O'Farrell, G. Eda, A. H. Castro Neto, and B. Özyilmaz, "Spinorbit proximity effect in graphene," *Nature Communications*, vol. 5, p. 4875, sep 2014.
- [13] Z. Wang, D. Ki, H. Chen, H. Berger, A. H. MacDonald, and A. F. Morpurgo, "Strong interface-induced spinorbit interaction in graphene on  $WS_2$ ," *Nature Communications*, vol. 6, p. 8339, sep 2015.
- [14] C. R. Dean, A. F. Young, I. Meric, C. Lee, L. Wang, S. Sorgenfrei, K. Watanabe, T. Taniguchi, P. Kim, K. L. Shepard, and J. Hone, "Boron nitride substrates for high-quality graphene electronics," *Nat Nano*, vol. 5, no. 10, pp. 722–726, oct 2010.
- [15] L. Wang, I. Meric, P. Y. Huang, Q. Gao, Y. Gao, H. Tran, T. Taniguchi, K. Watanabe, L. M. Campos, D. A. Muller, J. Guo, P. Kim, J. Hone, K. L. Shepard, and C. R. Dean, "One-Dimensional Electrical Contact to a Two-Dimensional Material," *Science*, vol. 342, no. 6158, pp. 614 LP – 617, oct 2013.
- [16] G.-H. Lee, Y.-J. Yu, C. Lee, C. Dean, K. L. Shepard, P. Kim, and J. Hone, "Electron tunneling through atomically flat and ultrathin hexagonal boron nitride," *Applied Physics Letters*, vol. 99, no. 24, p. 243114, 2011.
- [17] L. Britnell, R. V. Gorbachev, R. Jalil, B. D. Belle, F. Schedin, M. I. Katsnelson, L. Eaves, S. V. Morozov, A. S. Mayorov, N. M. R. Peres, A. H. Castro Neto, J. Leist, A. K. Geim, L. A. Ponomarenko, and K. S. Novoselov, "Electron Tunneling through Ultrathin Boron Nitride Crystalline Barriers," *Nano Letters*, vol. 12, no. 3, pp. 1707–1710, mar 2012.
- [18] A. H. Castro Neto, F. Guinea, N. M. R. Peres, K. S. Novoselov, and A. K. Geim, "The electronic properties of graphene," *Rev. Mod. Phys.*, vol. 81, pp. 109–162, Jan 2009.

- [19] K. S. Novoselov, A. K. Geim, S. V. Morozov, D. Jiang, Y. Zhang, S. V. Dubonos, I. V. Grigorieva, and A. A. Firsov, "Electric field effect in atomically thin carbon films," *Science*, vol. 306, no. 5696, pp. 666–669, 2004.
- [20] S. V. Morozov, K. S. Novoselov, M. I. Katsnelson, F. Schedin, D. C. Elias, J. A. Jaszczak, and A. K. Geim, "Giant intrinsic carrier mobilities in graphene and its bilayer," *Phys. Rev. Lett.*, vol. 100, p. 016602, Jan 2008.
- [21] K. I. Bolotin, K. J. Sikes, Z. Jiang, M. Klima, G. Fudenberg, J. Hone, P. Kim, and H. L. Stormer, "Ultrahigh electron mobility in suspended graphene," *Solid State Communications*, vol. 146, no. 9, pp. 351–355, 2008.
- [22] K. I. Bolotin, F. Ghahari, M. D. Shulman, H. L. Stormer, and P. Kim, "Observation of the fractional quantum Hall effect in graphene," *Nature*, vol. 462, no. 7270, pp. 196–199, nov 2009.
- [23] X. Du, I. Skachko, F. Duerr, A. Luican, and E. Y. Andrei, "Fractional quantum Hall effect and insulating phase of Dirac electrons in graphene," *Nature*, vol. 462, no. 7270, pp. 192–195, nov 2009.
- [24] C. Lee, X. Wei, J. W. Kysar, and J. Hone, "Measurement of the Elastic Properties and Intrinsic Strength of Monolayer Graphene," *Science*, vol. 321, no. 5887, pp. 385 LP – 388, jul 2008.
- [25] S.-P. Gao, "Crystal structures and band gap characters of h-BN polytypes predicted by the dispersion corrected DFT and GW method," *Solid State Communications*, vol. 152, no. 19, pp. 1817–1820, oct 2012.
- [26] K. Watanabe, T. Taniguchi, and H. Kanda, "Direct-bandgap properties and evidence for ultraviolet lasing of hexagonal boron nitride single crystal," *Nat Mater*, vol. 3, no. 6, pp. 404–409, jun 2004.
- [27] E. S. Kadantsev and P. Hawrylak, "Electronic structure of a single MoS<sub>2</sub> monolayer," *Solid State Communications*, vol. 152, no. 10, pp. 909–913, 2012.
- [28] K. F. Mak, C. Lee, J. Hone, J. Shan, and T. F. Heinz, "Atomically Thin MoS<sub>2</sub>: A New Direct-Gap Semiconductor," *Physical Review Letters*, vol. 105, no. 13, p. 136805, sep 2010.
- [29] B. Radisavljevic and A. Kis, "Mobility engineering and a metal-insulator transition in monolayer MoS<sub>2</sub>," *Nat Mater*, vol. 12, no. 9, pp. 815–820, sep 2013.

- [30] K. Sera, F. Okumura, H. Uchida, S. Itoh, S. Kaneko, and K. Hotta, "High-performance tfts fabricated by xecl excimer laser annealing of hydrogenated amorphous-silicon film," *IEEE Transactions on Electron Devices*, vol. 36, no. 12, pp. 2868–2872, Dec 1989.
- [31] S. K. Gupta, P. Jha, A. Singh, M. M. Chehimi, and D. K. Aswal, "Flexible organic semiconductor thin films," *J. Mater. Chem. C*, vol. 3, pp. 8468–8479, 2015.
- [32] T. Hasegawa and J. Takeya, "Organic field-effect transistors using single crystals," *Science and Technology of Advanced Materials*, vol. 10, no. 2, p. 024314, 2009.
- [33] K. F. Mak, K. He, J. Shan, and T. F. Heinz, "Control of valley polarization in monolayer MoS<sub>2</sub> by optical helicity," *Nat Nano*, vol. 7, no. 8, pp. 494–498, aug 2012.
- [34] K. F. Mak, K. L. McGill, J. Park, and P. L. McEuen, "The valley Hall effect in MoS<sub>2</sub> transistors," *Science*, vol. 344, no. 6191, pp. 1489 LP – 1492, jun 2014.
- [35] G. Eda, T. Fujita, H. Yamaguchi, D. Voiry, M. Chen, and M. Chhowalla, "Coherent Atomic and Electronic Heterostructures of Single-Layer MoS<sub>2</sub>," *ACS Nano*, vol. 6, no. 8, pp. 7311–7317, aug 2012.
- [36] R. Kappera, D. Voiry, S. E. Yalcin, B. Branch, G. Gupta, A. D. Mohite, and M. Chhowalla, "Phase-engineered low-resistance contacts for ultrathin MoS<sub>2</sub> transistors," *Nat Mater*, vol. 13, no. 12, pp. 1128–1134, dec 2014.
- [37] X. Xi, Z. Wang, W. Zhao, J.-H. Park, K. T. Law, H. Berger, L. Forro, J. Shan, and K. F. Mak, "Ising pairing in superconducting NbSe<sub>2</sub> atomic layers," *Nat Phys*, vol. 12, no. 2, pp. 139–143, feb 2016.
- [38] M. R. Laskar, D. N. Nath, L. Ma, E. W. Lee, C. H. Lee, T. Kent, Z. Yang, R. Mishra, M. A. Roldan, J.-C. Idrobo, S. T. Pantelides, S. J. Pennycook, R. C. Myers, Y. Wu, and S. Rajan, "p-type doping of MoS<sub>2</sub> thin films using Nb," *Applied Physics Letters*, vol. 104, no. 9, p. 92104, mar 2014.
- [39] D. Li, M. B. Muller, S. Gilje, R. B. Kaner, and G. G. Wallace, "Processable aqueous dispersions of graphene nanosheets," *Nat Nano*, vol. 3, no. 2, pp. 101–105, feb 2008.

- [40] Z. Luo, Y. Lu, L. A. Somers, and A. T. C. Johnson, "High Yield Preparation of Macroscopic Graphene Oxide Membranes," *Journal of the American Chemical Society*, vol. 131, no. 3, pp. 898–899, jan 2009.
- [41] V. C. Tung, M. J. Allen, Y. Yang, and R. B. Kaner, "High-throughput solution processing of large-scale graphene," *Nat Nano*, vol. 4, no. 1, pp. 25–29, jan 2009.
- [42] S. Mao, H. Pu, and J. Chen, "Graphene oxide and its reduction: modeling and experimental progress," *RSC Adv.*, vol. 2, pp. 2643–2662, 2012.
- [43] P. Sutter, J. T. Sadowski, and E. Sutter, "Graphene on pt(111): Growth and substrate interaction," *Phys. Rev. B*, vol. 80, p. 245411, Dec 2009.
- [44] P. W. Sutter, J.-I. Flege, and E. A. Sutter, "Epitaxial graphene on ruthenium," *Nat Mater*, vol. 7, no. 5, pp. 406–411, may 2008.
- [45] A. T. N. Michely, J. Coraux, T. N. Plasa, C. Busse, and Thomas, "Structure of epitaxial graphene on Ir(111)," *New Journal of Physics*, vol. 10, no. 4, p. 43033, 2008.
- [46] A. Reina, X. Jia, J. Ho, D. Nezich, H. Son, V. Bulovic, M. S. Dresselhaus, and J. Kong, "Large Area, Few-Layer Graphene Films on Arbitrary Substrates by Chemical Vapor Deposition," *Nano Letters*, vol. 9, no. 1, pp. 30–35, jan 2009.
- [47] K. S. Kim, Y. Zhao, H. Jang, S. Y. Lee, J. M. Kim, K. S. Kim, J.-H. Ahn, P. Kim, J.-Y. Choi, and B. H. Hong, "Large-scale pattern growth of graphene films for stretchable transparent electrodes," *Nature*, vol. 457, no. 7230, pp. 706–710, feb 2009.
- [48] X. Li, W. Cai, J. An, S. Kim, J. Nah, D. Yang, R. Piner, A. Velamakanni, I. Jung, E. Tutuc, S. K. Banerjee, L. Colombo, and R. S. Ruoff, "Large-Area Synthesis of High-Quality and Uniform Graphene Films on Copper Foils," *Science*, vol. 324, no. 5932, pp. 1312 LP – 1314, jun 2009.
- [49] I. Brihuega, P. Mallet, H. González-Herrero, G. Trambly de Laissardière, M. M. Ugeda, L. Magaud, J. M. Gómez-Rodríguez, F. Ynduráin, and J.-Y. Veullen, "Unraveling the Intrinsic and Robust Nature of van Hove Singularities in Twisted Bilayer Graphene by Scanning Tunneling Microscopy and Theoretical Analysis," *Physical Review Letters*, vol. 109, no. 19, p. 196802, nov 2012.

- [50] T. Ohta, A. Bostwick, T. Seyller, K. Horn, and E. Rotenberg, "Controlling the Electronic Structure of Bilayer Graphene," *Science*, vol. 313, no. 5789, pp. 951 LP – 954, aug 2006.
- [51] T. Ohta, A. Bostwick, J. L. McChesney, T. Seyller, K. Horn, and E. Rotenberg, "Interlayer interaction and electronic screening in multilayer graphene investigated with angle-resolved photoemission spectroscopy," *Phys. Rev. Lett.*, vol. 98, p. 206802, May 2007.
- [52] X. Cui, G.-H. Lee, Y. D. Kim, G. Arefe, P. Y. Huang, C.-H. Lee, D. A. Chenet, X. Zhang, L. Wang, F. Ye, F. Pizzocchero, B. S. Jessen, K. Watanabe, T. Taniguchi, D. A. Muller, T. Low, P. Kim, and J. Hone, "Multi-terminal transport measurements of MoS<sub>2</sub> using a van der Waals heterostructure device platform," *Nat Nano*, vol. 10, no. 6, pp. 534–540, jun 2015.
- [53] C. R. Dean, L. Wang, P. Maher, C. Forsythe, F. Ghahari, Y. Gao, J. Katoch, M. Ishigami, P. Moon, M. Koshino, T. Taniguchi, K. Watanabe, K. L. Shepard, J. Hone, and P. Kim, "Hofstadter /'s butterfly and the fractal quantum Hall effect in moire superlattices," *Nature*, vol. 497, no. 7451, pp. 598–602, may 2013.
- [54] R. V. Gorbachev, A. K. Geim, M. I. Katsnelson, K. S. Novoselov, T. Tudorovskiy, I. V. Grigorieva, A. H. MacDonald, S. V. Morozov, K. Watanabe, T. Taniguchi, and L. A. Ponomarenko, "Strong Coulomb drag and broken symmetry in double-layer graphene," *Nat Phys*, vol. 8, no. 12, pp. 896–901, dec 2012.
- [55] Y. Kim, H. Yun, S.-G. Nam, M. Son, D. S. Lee, D. C. Kim, S. Seo, H. C. Choi, H.-J. Lee, S. W. Lee, and J. S. Kim, "Breakdown of the interlayer coherence in twisted bilayer graphene," *Phys. Rev. Lett.*, vol. 110, p. 096602, Feb 2013.
- [56] K. Kaasbjerg, K. S. Thygesen, and K. W. Jacobsen, "Phonon-limited mobility in n-type single-layer MoS<sub>2</sub> from first principles," *Phys. Rev. B*, vol. 85, no. 11, p. 115317, 2012.
- [57] B. W. H. Baugher, H. O. H. Churchill, Y. Yang, and P. Jarillo-Herrero, "Intrinsic Electronic Transport Properties of High-Quality Monolayer and Bilayer MoS<sub>2</sub>," *Nano Letters*, vol. 13, no. 9, pp. 4212–4216, sep 2013.
- [58] H. Schmidt, S. Wang, L. Chu, M. Toh, R. Kumar, W. Zhao, A. H. Castro Neto, J. Martin, S. Adam, B. Özyilmaz, and G. Eda, "Transport Properties of Monolayer MoS<sub>2</sub> Grown by Chemical Vapor Deposition," *Nano Letters*, vol. 14, no. 4, pp. 1909–1913, apr 2014.

- [59] D. Jariwala, V. K. Sangwan, D. J. Late, J. E. Johns, V. P. Dravid, T. J. Marks, L. J. Lauhon, and M. C. Hersam, "Band-like transport in high mobility unencapsulated single-layer MoS<sub>2</sub> transistors," *Applied Physics Letters*, vol. 102, no. 17, p. 173107, apr 2013.
- [60] D. Ovchinnikov, A. Allain, Y.-S. Huang, D. Dumcenco, and A. Kis, "Electrical Transport Properties of Single-Layer WS<sub>2</sub>," *ACS Nano*, vol. 8, no. 8, pp. 8174–8181, aug 2014.
- [61] D. MacNeill, G. M. Stiehl, M. H. D. Guimaraes, R. A. Buhrman, J. Park, and D. C. Ralph, "Control of spin-orbit torques through crystal symmetry in WTe<sub>2</sub>/ferromagnet bilayers," *Nat Phys*, vol. 13, no. 3, pp. 300–305, mar 2017.
- [62] Z. Ye, T. Cao, K. O'Brien, H. Zhu, X. Yin, Y. Wang, S. G. Louie, and X. Zhang, "Probing excitonic dark states in single-layer tungsten disulphide," *Nature*, vol. 513, no. 7517, pp. 214–218, sep 2014.
- [63] Q. Feng, Y. Zhu, J. Hong, M. Zhang, W. Duan, N. Mao, J. Wu, H. Xu, F. Dong, F. Lin, C. Jin, C. Wang, J. Zhang, and L. Xie, "Growth of Large-Area 2D MoS<sub>2</sub>(1-x)Se<sub>2x</sub> Semiconductor Alloys," *Advanced Materials*, vol. 26, no. 17, pp. 2648–2653, 2014.
- [64] W. Wu, L. Wang, Y. Li, F. Zhang, L. Lin, S. Niu, D. Chenet, X. Zhang, Y. Hao, T. F. Heinz, J. Hone, and Z. L. Wang, "Piezoelectricity of single-atomic-layer MoS<sub>2</sub> for energy conversion and piezotronics," *Nature*, vol. 514, no. 7523, pp. 470–474, oct 2014.
- [65] Y.-C. Lin, W. Zhang, J.-K. Huang, K.-K. Liu, Y.-H. Lee, C.-T. Liang, C.-W. Chu, and L.-J. Li, "Wafer-scale MoS<sub>2</sub> thin layers prepared by MoO<sub>3</sub> sulfurization," *Nanoscale*, vol. 4, no. 20, pp. 6637–6641, 2012.
- [66] I. Song, C. Park, M. Hong, J. Baik, H.-J. Shin, and H. C. Choi, "Patternable Large-Scale Molybdenum Disulfide Atomic Layers Grown by Gold-Assisted Chemical Vapor Deposition," *Angewandte Chemie International Edition*, vol. 53, no. 5, pp. 1266–1269, 2014.
- [67] S. Najmaei, Z. Liu, W. Zhou, X. Zou, G. Shi, S. Lei, B. I. Yakobson, J.-C. Idrobo, P. M. Ajayan, and J. Lou, "Vapour phase growth and grain boundary structure of molybdenum disulphide atomic layers," *Nat Mater*, vol. 12, no. 8, pp. 754–759, aug 2013.

- [68] A. M. van der Zande, P. Y. Huang, D. A. Chenet, T. C. Berkelbach, Y. You, G.-H. Lee, T. F. Heinz, D. R. Reichman, D. A. Muller, and J. C. Hone, "Grains and grain boundaries in highly crystalline monolayer molybdenum disulphide," *Nat Mater*, vol. 12, no. 6, pp. 554–561, jun 2013.
- [69] Y.-H. Lee, L. Yu, H. Wang, W. Fang, X. Ling, Y. Shi, C.-T. Lin, J.-K. Huang, M.-T. Chang, C.-S. Chang, M. Dresselhaus, T. Palacios, L.-J. Li, and J. Kong, "Synthesis and Transfer of Single-Layer Transition Metal Disulfides on Diverse Surfaces," *Nano Letters*, vol. 13, no. 4, pp. 1852–1857, apr 2013.
- [70] H. Liu, M. Si, S. Najmaei, A. T. Neal, Y. Du, P. M. Ajayan, J. Lou, and P. D. Ye, "Statistical Study of Deep Submicron Dual-Gated Field-Effect Transistors on Monolayer Chemical Vapor Deposition Molybdenum Disulfide Films," *Nano Letters*, vol. 13, no. 6, pp. 2640–2646, jun 2013.
- [71] Y. Yu, C. Li, Y. Liu, L. Su, Y. Zhang, and L. Cao, "Controlled Scalable Synthesis of Uniform, High-Quality Monolayer and Few-layer MoS<sub>2</sub> Films," *Scientific Reports*, vol. 3, p. 1866, may 2013.
- [72] Y. Zhang, Y. Zhang, Q. Ji, J. Ju, H. Yuan, J. Shi, T. Gao, D. Ma, M. Liu, Y. Chen, X. Song, H. Y. Hwang, Y. Cui, and Z. Liu, "Controlled Growth of High-Quality Monolayer WS<sub>2</sub> Layers on Sapphire and Imaging Its Grain Boundary," *ACS Nano*, vol. 7, no. 10, pp. 8963–8971, oct 2013.
- [73] K. Kang, S. Xie, L. Huang, Y. Han, P. Y. Huang, K. F. Mak, C.-J. Kim, D. Muller, and J. Park, "High-mobility three-atom-thick semiconducting films with wafer-scale homogeneity," *Nature*, vol. 520, no. 7549, pp. 656–660, apr 2015.
- [74] D. King and D. Woodruff, *Growth and Properties of Ultrathin Epitaxial Layers*. Elsevier, jun 1997.
- [75] J. H. Sung, H. Heo, S. Si, Y. H. Kim, H. R. Noh, K. Song, J. Kim, C.-S. Lee, S.-Y. Seo, D.-H. Kim, H. K. Kim, H. W. Yeom, T.-H. Kim, S.-Y. Choi, J. S. Kim, and M.-H. Jo, "Coplanar semiconductormetal circuitry defined on few-layer MoTe<sub>2</sub> via polymorphic heteroepitaxy," sep 2017.
- [76] Z. Wang, Y. Xie, H. Wang, R. Wu, T. Nan, Y. Zhan, J. Sun, T. Jiang, Y. Zhao, Y. Lei, M. Yang, W. Wang, Q. Zhu, X. Ma, and Y. Hao, "NaCl-assisted one-step growth of mos<sub>2</sub> ws<sub>2</sub> in-plane heterostructures," *Nanotechnology*, vol. 28, no. 32, p. 325602, 2017.

- [77] S. Li, S. Wang, D.-M. Tang, W. Zhao, H. Xu, L. Chu, Y. Bando, D. Golberg, and G. Eda, "Halide-assisted atmospheric pressure growth of large wse2 and ws2 monolayer crystals," *Applied Materials Today*, vol. 1, no. 1, pp. 60–66, 2015.
- [78] H. Kim, D. Ovchinnikov, D. Deiana, D. Unuchek, and A. Kis, "Suppressing nucleation in metalorganic chemical vapor deposition of mos2 monolayers by alkali metal halides," *Nano Letters*, vol. 17, no. 8, pp. 5056–5063, 2017, pMID: 28700239.
- [79] R. Connor and H. Adkins, "Hydrogenolysis of Oxygenated Organic Compounds," *Journal of the American Chemical Society*, vol. 54, no. 12, pp. 4678–4690, dec 1932.
- [80] S. Cristol, J. F. Paul, E. Payen, D. Bougeard, S. Clemendot, and F. Hutschka, "Theoretical study of the MoS<sub>2</sub> (100) surface: A chemical potential analysis of sulfur and hydrogen coverage," *JOURNAL OF PHYSICAL CHEMISTRY B*, vol. 104, no. 47, pp. 11 220–11 229, 2000.
- [81] W. Zhao, Z. Ghorannevis, L. Chu, M. Toh, C. Kloc, P.-H. Tan, and G. Eda, "Evolution of Electronic Structure in Atomically Thin Sheets of WS<sub>2</sub> and WSe<sub>2</sub>," *ACS Nano*, vol. 7, no. 1, pp. 791–797, jan 2013.
- [82] H. Li, Q. Zhang, C. C. R. Yap, B. K. Tay, T. H. T. Edwin, A. Olivier, and D. Baillargeat, "From Bulk to Monolayer MoS<sub>2</sub>: Evolution of Raman Scattering," *Advanced Functional Materials*, vol. 22, no. 7, pp. 1385–1390, 2012.
- [83] A. Berkdemir, H. R. Gutierrez, A. R. Botello-Mendez, N. Perea-Lopez, A. L. Elias, C.-I. Chia, B. Wang, V. H. Crespi, F. Lopez-Urias, J.-C. Charlier, H. Terrones, and M. Terrones, "Identification of individual and few layers of WS<sub>2</sub> using Raman Spectroscopy," *SCIENTIFIC REPORTS*, vol. 3, 2013.
- [84] S. Najmaei, M. Amani, M. L. Chin, Z. Liu, A. G. Birdwell, T. P. O'Regan, P. M. Ajayan, M. Dubey, and J. Lou, "Electrical Transport Properties of Polycrystalline Monolayer Molybdenum Disulfide," *ACS Nano*, vol. 8, no. 8, pp. 7930–7937, aug 2014.
- [85] J. M. B. Lopes dos Santos, N. M. R. Peres, and A. H. Castro Neto, "Graphene Bilayer with a Twist: Electronic Structure," *Physical Review Letters*, vol. 99, no. 25, p. 256802, dec 2007.
- [86] G. Li, A. Luican, J. M. B. Lopes dos Santos, A. H. Castro Neto, A. Reina,

- J. Kong, and E. Y. Andrei, "Observation of Van Hove singularities in twisted graphene layers," *Nat Phys*, vol. 6, no. 2, pp. 109–113, feb 2010.
- [87] A. Luican, G. Li, A. Reina, J. Kong, R. R. Nair, K. S. Novoselov, A. K. Geim, and E. Y. Andrei, "Single-Layer Behavior and Its Breakdown in Twisted Graphene Layers," *Physical Review Letters*, vol. 106, no. 12, p. 126802, mar 2011.
- [88] T. Ohta, J. T. Robinson, P. J. Feibelman, A. Bostwick, E. Rotenberg, and T. E. Beechem, "Evidence for Interlayer Coupling and Moiré Periodic Potentials in Twisted Bilayer Graphene," *Physical Review Letters*, vol. 109, no. 18, p. 186807, nov 2012.
- [89] Y. Cao, J. Luo, V. Fatemi, S. Fang, J. Sanchez-Yamagishi, K. Watanabe, T. Taniguchi, E. Kaxiras, and P. Jarillo-Herrero, "Superlattice-Induced Insulating States and Valley-Protected Orbits in Twisted Bilayer Graphene," *Physical Review Letters*, vol. 117, no. 11, p. 116804, sep 2016.
- [90] P. R. Wallace, "The band theory of graphite," *Phys. Rev.*, vol. 71, pp. 622–634, May 1947.
- [91] B. Partoens and F. M. Peeters, "From graphene to graphite: Electronic structure around the k point," *Phys. Rev. B*, vol. 74, p. 075404, Aug 2006.
- [92] Y. Zhang, T.-T. Tang, C. Girit, Z. Hao, M. C. Martin, A. Zettl, M. F. Crommie, Y. R. Shen, and F. Wang, "Direct observation of a widely tunable bandgap in bilayer graphene," *Nature*, vol. 459, no. 7248, pp. 820–823, jun 2009.
- [93] S. Shallcross, S. Sharma, E. Kandelaki, and O. A. Pankratov, "Electronic structure of turbostratic graphene," *Physical Review B*, vol. 81, no. 16, p. 165105, apr 2010.
- [94] C.-J. Kim, Sánchez-Castillo A., Z. Ziegler, Y. Ogawa, C. Noguez, and J. Park, "Chiral atomically thin films," *Nat Nano*, vol. 11, no. 6, pp. 520–524, jun 2016.
- [95] J. Lopes dos Santos, N. Peres, and a. Castro Neto, "Continuum model of the twisted graphene bilayer," *Physical Review B*, vol. 86, no. 15, p. 155449, oct 2012.
- [96] C.-F. Chen, C.-H. Park, B. W. Boudouris, J. Horng, B. Geng, C. Girit,

- A. Zettl, M. F. Crommie, R. A. Segalman, S. G. Louie, and F. Wang, "Controlling inelastic light scattering quantum pathways in graphene," *Nature*, vol. 471, no. 7340, pp. 617–620, mar 2011.
- [97] K. Kim, A. DaSilva, S. Huang, B. Fallahazad, S. Larentis, T. Taniguchi, K. Watanabe, B. J. LeRoy, A. H. MacDonald, and E. Tutuc, "Tunable moiré bands and strong correlations in small-twist-angle bilayer graphene," *Proceedings of the National Academy of Sciences*, 2017.
- [98] E. Suárez Morell, P. Vargas, L. Chico, and L. Brey, "Charge redistribution and interlayer coupling in twisted bilayer graphene under electric fields," *Physical Review B*, vol. 84, no. 19, p. 195421, nov 2011.
- [99] L. Brown, R. Hovden, P. Huang, M. Wojcik, D. A. Muller, and J. Park, "Twinning and Twisting of Tri- and Bilayer Graphene," *Nano Letters*, vol. 12, no. 3, pp. 1609–1615, feb 2012.
- [100] J. K. Wassei, M. Mecklenburg, J. A. Torres, J. D. Fowler, B. C. Regan, R. B. Kaner, and B. H. Weiller, "Chemical vapor deposition of graphene on copper from methane, ethane and propane: Evidence for bilayer selectivity," *Small*, vol. 8, no. 9, pp. 1415–1422, 2012.
- [101] Z. Li, P. Wu, C. Wang, X. Fan, W. Zhang, X. Zhai, C. Zeng, Z. Li, J. Yang, and J. Hou, "Low-Temperature Growth of Graphene by Chemical Vapor Deposition Using Solid and Liquid Carbon Sources," *ACS Nano*, vol. 5, no. 4, pp. 3385–3390, apr 2011.
- [102] R. M. Jacobberger and M. S. Arnold, "Graphene Growth Dynamics on Epitaxial Copper Thin Films," *Chemistry of Materials*, vol. 25, no. 6, pp. 871–877, mar 2013.
- [103] X. Li, C. W. Magnuson, A. Venugopal, R. M. Tromp, J. B. Hannon, E. M. Vogel, L. Colombo, and R. S. Ruoff, "Large-Area Graphene Single Crystals Grown by Low-Pressure Chemical Vapor Deposition of Methane on Copper," *Journal of the American Chemical Society*, vol. 133, no. 9, pp. 2816–2819, mar 2011.
- [104] Y. Ogawa, B. Hu, C. M. Orofeo, M. Tsuji, K.-i. Ikeda, S. Mizuno, H. Hibino, and H. Ago, "Domain Structure and Boundary in Single-Layer Graphene Grown on Cu(111) and Cu(100) Films," *The Journal of Physical Chemistry Letters*, vol. 3, no. 2, pp. 219–226, jan 2012.

- [105] Y. Pan, H. Zhang, D. Shi, J. Sun, S. Du, F. Liu, and H.-j. Gao, "Highly ordered, millimeter-scale, continuous, single-crystalline graphene monolayer formed on Ru(0001)," *Advanced Materials*, vol. 21, no. 27, pp. 2777–2780, 2009.
- [106] J. Coraux, A. T. NDiaye, C. Busse, and T. Michely, "Structural Coherency of Graphene on Ir(111)," *Nano Letters*, vol. 8, no. 2, pp. 565–570, feb 2008.
- [107] S. Roth, J. Osterwalder, and T. Greber, "Synthesis of epitaxial graphene on rhodium from 3-pentanone," *Surface Science*, vol. 605, no. 9, pp. L17–L19, 2011.
- [108] J.-H. Lee, E. K. Lee, W.-J. Joo, Y. Jang, B.-S. Kim, J. Y. Lim, S.-H. Choi, S. J. Ahn, J. R. Ahn, M.-H. Park, C.-W. Yang, B. L. Choi, S.-W. Hwang, and D. Whang, "Wafer-scale growth of single-crystal monolayer graphene on reusable hydrogen-terminated germanium," *Science*, vol. 344, no. 6181, pp. 286–289, 2014.
- [109] L. Brown, E. B. Lochocki, J. Avila, C.-J. Kim, Y. Ogawa, R. W. Havener, D.-K. Kim, E. J. Monkman, D. E. Shai, H. I. Wei, M. P. Levendorf, M. Asensio, K. M. Shen, and J. Park, "Polycrystalline Graphene with Single Crystalline Electronic Structure," *Nano Letters*, vol. 14, no. 10, pp. 5706–5711, oct 2014.
- [110] E. Suárez Morell, J. D. Correa, P. Vargas, M. Pacheco, and Z. Barticevic, "Flat bands in slightly twisted bilayer graphene: Tight-binding calculations," *Physical Review B*, vol. 82, no. 12, p. 121407, sep 2010.
- [111] A. B. Esquinazi, J. Barzola-Quiquia, T. Scheike, and P., "Josephson-coupled superconducting regions embedded at the interfaces of highly oriented pyrolytic graphite," *New Journal of Physics*, vol. 15, no. 2, p. 23024, 2013.
- [112] T. Scheike, P. Esquinazi, A. Setzer, and W. Böhlmann, "Granular superconductivity at room temperature in bulk highly oriented pyrolytic graphite samples," *Carbon*, vol. 59, pp. 140–149, aug 2013.
- [113] P. Esquinazi, T. T. Heikkilä, Y. V. Lysogorskiy, D. A. Tayurskii, and G. E. Volovik, "On the superconductivity of graphite interfaces," *JETP Letters*, vol. 100, no. 5, pp. 336–339, 2014.
- [114] W.-T. Pong and C. Durkan, "A review and outlook for an anomaly of scanning tunnelling microscopy (stm): superlattices on graphite," *Journal of Physics D: Applied Physics*, vol. 38, no. 21, p. R329, 2005.

- [115] L. Huang, C.-J. Kim, A. W. Tsen, L. Brown, M. Guimaraes, and J. Park, "Small-angle twisted bilayer graphene interlayer rotation detection with Raman R' process," *To be submitted*, 2017.
- [116] V. Carozo, C. M. Almeida, E. H. M. Ferreira, L. G. Cançado, C. A. Achete, and A. Jorio, "Raman Signature of Graphene Superlattices," *Nano Letters*, vol. 11, no. 11, pp. 4527–4534, nov 2011.
- [117] C.-C. Lu, Y.-C. Lin, Z. Liu, C.-H. Yeh, K. Suenaga, and P.-W. Chiu, "Twisting Bilayer Graphene Superlattices," *ACS Nano*, vol. 7, no. 3, pp. 2587–2594, mar 2013.
- [118] A. Niilisk, T. Kahro, V. Kiisk, M. Rähn, H. Alles, J. Aarik, and V. Sammelselg, "Raman modes in transferred bilayer CVD graphene," 2015.
- [119] C.-H. Yeh, Y.-C. Lin, P. K. Nayak, C.-C. Lu, Z. Liu, K. Suenaga, and P.-W. Chiu, "Probing interlayer coupling in twisted single-crystal bilayer graphene by raman spectroscopy," *Journal of Raman Spectroscopy*, vol. 45, no. 10, pp. 912–917, 2014, jRS-14-0128.R1.
- [120] X.-D. Chen, W. Xin, W.-S. Jiang, Z.-B. Liu, Y. Chen, and J.-G. Tian, "High-precision twist-controlled bilayer and trilayer graphene," *Advanced Materials*, vol. 28, no. 13, pp. 2563–2570, 2016.
- [121] J. Maultzsch, S. Reich, C. Thomsen, H. Requardt, and P. Ordejón, "Phonon Dispersion in Graphite," *Physical Review Letters*, vol. 92, no. 7, p. 75501, feb 2004.
- [122] D. Yoon, H. Moon, Y.-W. Son, G. Samsonidze, B. H. Park, J. B. Kim, Y. Lee, and H. Cheong, "Strong Polarization Dependence of Double-Resonant Raman Intensities in Graphene," *Nano Letters*, vol. 8, no. 12, pp. 4270–4274, dec 2008.
- [123] R. W. Havener, S.-Y. Ju, L. Brown, Z. Wang, M. Wojcik, C. S. Ruiz-Vargas, and J. Park, "High-Throughput Graphene Imaging on Arbitrary Substrates with Widefield Raman Spectroscopy," *ACS Nano*, vol. 6, no. 1, pp. 373–380, jan 2012.
- [124] P. Moon and M. Koshino, "Optical absorption in twisted bilayer graphene," *Physical Review B*, vol. 87, no. 20, p. 205404, may 2013.
- [125] J. D. Sanchez-Yamagishi, T. Taychatanapat, K. Watanabe, T. Taniguchi,

- A. Yacoby, and P. Jarillo-Herrero, "Quantum Hall Effect, Screening, and Layer-Polarized Insulating States in Twisted Bilayer Graphene," *Physical Review Letters*, vol. 108, no. 7, p. 76601, feb 2012.
- [126] K. Kang, K.-H. Lee, Y. Han, H. Gao, S. Xie, D. A. Muller, and J. Park, "Layer-by-layer assembly of two-dimensional materials into wafer-scale heterostructures," *Nature*, vol. advance online publication, sep 2017.
- [127] M. H. D. Guimarães, H. Gao, Y. Han, K. Kang, S. Xie, C.-J. Kim, D. A. Muller, D. C. Ralph, and J. Park, "Atomically Thin Ohmic Edge Contacts Between Two-Dimensional Materials," *ACS Nano*, vol. 10, no. 6, pp. 6392–6399, jun 2016.
- [128] M. P. Levendorf, C.-J. Kim, L. Brown, P. Y. Huang, R. W. Havener, D. A. Muller, and J. Park, "Graphene and boron nitride lateral heterostructures for atomically thin circuitry," *Nature*, vol. 488, no. 7413, pp. 627–632, aug 2012.
- [129] J. J. Fripiat, J. Uytterhoeven, U. Schobinger, and H. Deuel, "Etude physico-chimique de quelques drivs organiques d'un silicagel," *Helvetica Chimica Acta*, vol. 43, no. 1, pp. 176–181, 1960.